Title
Usp9x regulates a peri-implantation switch in PRC2 activity

Author
Macrae, Trisha Anne

Publication Date
2019

Peer reviewed|Thesis/dissertation

Usp9x regulates a peri-implantation switch in PRC2 activity

by
Trisha Anne Macrae

DISSERTATION
Submitted in partial satisfaction of the requirements for degree of
DOCTOR OF PHILOSOPHY

in

Biomedical Sciences

in the

GRADUATE DIVISION
of the
UNIVERSITY OF CALIFORNIA, SAN FRANCISCO

Approved:

DocuSigned by:
Aimee Kao
745CF57D40DB494...
Aimee Kao
Chair

DocuSigned by:
Miguel Ramalho-Santos
DocuSigned by:
Jeremy Reiter
DocuSigned by:
David Morgan
AAC13F29657E472...
Miguel Ramalho-Santos
Jeremy Reiter
David Morgan

Committee Members

For my parents,

who have cheered me on through nearly two and a half *decades* of schooling—

even though I keep running off to snowy climates.

Acknowledgments

I talk a lot about stem cells in this thesis. One important feature of stem cell biology that I won't discuss is the stem cell niche, the particular environment that maintains stem cell compartments and control their proper development. In recent months, as I've thought a lot about framing my PhD work, it occurred to me that the "niche" concept works nicely as a metaphor for graduate school, or at least as a metaphor for my own experience. The making of this graduate student required a steady diet of pro-growth signals: chocolate (and/or sequencing library cake), feedback and advice, encouragement, protocols, commiseration, more chocolate, and laughter. I'm lucky to have an ever-growing niche. Although I can't name everyone who has supported me here, here are a few people who deserve recognition.

To my graduate mentor, Miguel Ramalho-Santos: thank you. I can always count on you to offer feedback that is incisive but kind, motivated by deep curiosity yet grounded in mechanism and well-controlled experiments. Your love of science is infectious, your optimism inspiring. I am a bolder thinker and a more inquisitive, confident scientist thanks to my time in your lab.

Thank you to members of the Santos lab, past and present. Shout-out to Aydan, Michelle, Steffen, Stephanie—my original lab crew. Y'all made me the scientist that I am today (did I say that right, Steph?), and I'm grateful for all of those long lunches, coffees, and Friday wine hours in Pod B, not to mention deep life chats across benches and between TC hoods. Extra thanks to Aydan, who inspired my love of chromatin and always answered my questions, no matter how silly they were or how busy she was.

To the Toronto crew: it's been fun working alongside you. Evelyne, thank you for managing all of my rollercoaster emotions during a challenging lab transition, plus lots of science and adventure since then. Kirti, you manage to keep everything running and somehow always remain cheerful—I'm not sure how you do it. Brandon and Lamisa, I already miss our student office, but I trust you to carry on the legacy. Juan and Tania, thank you for good conversations about science and life. Golubina, Bilal, Deanna, Karl, and Jimmy, thanks for making sure I had a life and support system outside of the lab, despite my best efforts.

Summers in Kevin Shannon's lab at UCSF got me interested in science research and the MSTP path, so thank you to Monique Dail for taking a chance on a college student. Working with Lucy Godley at the University of Chicago convinced me that the physician-scientist track was for me. Many people at UCSF, but especially Geri, Demian, and Amanda, helped manage the logistics of my PhD. Thanks, as well, to members of my quals and thesis committees, for enthusiastic support and sound advice throughout the last few years: Aimee Kao, Jeremy Reiter, David Morgan, Diana Laird, Hiten Madhani, and Barbara Panning.

To all the friends from high school, college, and medical/grad school who visited me, emailed me, or texted me throughout my PhD, but especially during the time I was in Toronto: thank you. Truly, it means more than you know. Shelly, thank you for always having my back.

And finally—Mom and Dad, Cameron and Cara, and Dan. I would not be where (or who) I am without all of you.

A stem cell is no stem cell without its niche.

Contributions

Chapter 1 is the result of a collaborative effort with Aydan Bulut-Karslioglu and is reprinted largely as it appears in:

The transcriptionally permissive chromatin state of embryonic stem cells is acutely tuned to translational output. Bulut-Karslioglu A*, Macrae TA*, Oses-Prieto JA, Covarrubias S, Percharde M, Ku G, Diaz A, McManus MT, Burlingame AL, Ramalho-Santos M. *Cell Stem Cell* 22, 369-383 (2018). *co-first author.

Chapter 2 is adapted from a manuscript currently in preparation:

Usp9x regulates a peri-implantation switch in PRC2 activity. Macrae TA, Nora EP, Bruneau BG, Ramalho-Santos M. *Unpublished* (December 2019).

Usp9x regulates a peri-implantation switch in PRC2 activity

Trisha Anne Macrae

Abstract

How does a cell narrow from many possible fates to one? This question is highly relevant to pluripotent stem cells, which generate all tissue types of the adult organism. One answer is that pluripotent cells *in vitro* and in the peri-implantation mouse embryo undergo global rewiring of their chromatin landscape to prepare for lineage commitment. In this dissertation, I explore molecular mechanisms that regulate chromatin state during early development.

The emergence of permissive chromatin and hypertranscription in pluripotent cells enables rapid proliferation and lineage induction. We found that cellular growth pathways, most prominently translation, perpetuate the euchromatic state and hypertranscription of mouse embryonic stem (ES) cells. Inhibition of translation rapidly depletes euchromatic marks and reduces nascent transcription in ES cells and blastocysts. Our results identify a positive feedback loop between chromatin state and translational output, whereby high translational output sustains levels of unstable euchromatin regulators and may set the pace of proliferation at peri-implantation.

The transition to a permissive chromatin state coincides with widespread loss of facultative heterochromatin. Repressive histone H3 lysine 27 tri-methylation (H3K27me3), deposited by Polycomb Repressive Complex 2 (PRC2), is redistributed from broad distal blankets to mark the promoters of developmental genes. In this thesis,

I report a post-translational mechanism for control of PRC2. I found that the deubiquitinase Usp9x regulates PRC2 stability and activity in ES cells, and Usp9x levels capture the molecular transitions at implantation with remarkable fidelity. Transcriptome and chromatin analyses reveal that Usp9x-high cells bear a molecular signature of the pre-implantation embryo, whereas Usp9x-low cells resemble the post-implantation, gastrulating epiblast. These findings indicate that physiologic decline of Usp9x expression destabilizes PRC2 and helps constrict H3K27me3 during lineage induction. Deletion of *Usp9x* in pluripotent epiblast cells results in delayed repression of early lineage genes and developmental defects by embryonic day 9.5.

Studies in ES cells and early embryos provide insight into the regulatory logic that not only shapes embryonic development, but also underlies cell fate transitions more generally. The mechanistic interdependence of euchromatin, transcription and translation may apply to other fast-proliferating cells. Usp9x recurs as a marker of “stemness”; is essential for fly, mouse, and human development; and is mutated in various neurological disorders and cancers. Thus, the work described in this thesis has implications for stem/progenitor cell compartments, stem cell-based therapeutics, tissue regeneration and engineering, and cancer.

Table of Contents

List of Figures

Chapter 1

Chapter 2

List of Tables

General Introduction

It is not birth, marriage, or death, but gastrulation, which is truly the most important time in your life.

– Lewis Wolpert (1986)

It is impossible to say which stage of mammalian embryonic development is the most important. Some argue that it is gastrulation, or the establishment of the three embryonic germ layers. It is difficult to refute this point: mechanisms that drive gastrulation help form the body plan, meaning that they literally set the stage for subsequent development. To be clear, gastrulation is indeed a fascinating stage of development. Another candidate for the most important stage may be the "phylotypic stage" of development, the point at which vertebrate embryos attain a stereotyped form and are nearly indistinguishable from each other. The existence of a phylotypic stage suggests that major evolutionary pressures are at work to conserve certain features of embryonic development. In the mouse, the phylotypic stage occurs ~3-4 days after the embryo implants into the uterus, and it is also one that we will return to later in the text. Progression to first to gastrulation and then to the phylotypic stage, however, is predicated upon surviving the first few embryonic cell divisions. Let us not forget that all organisms begin as a single cell.

Development of the early mouse embryo

The first week is a dramatic time for the developing embryo (Fig. 1). The meeting of the sperm and the egg (oocyte) marks the time of fertilization, which in the mouse sets the developmental clock at embryonic day (E) 0. Within about 5 days, the large single-cell embryo (1-cell zygote) of the developing mouse segregates into embryonic versus precursor extraembryonic cells, in so doing transitioning from having cells of equivalent developmental potential to cells with specialized function (*differentiation*); it transitions from relying on RNA and protein molecules

stored in the cytoplasm, inherited from the oocyte, to transcribing genes from its own diploid genome; and, finally, it implants into the uterus. It is time to gastrulate.

One thing that does not occur within the first 5 days is growth. The dramatic changes in cell fate occur with minimal net gain of biomass. After fertilization, the zygote undergoes several rounds of cleavage cell division, meaning that the cells of the embryo divide without growing. Compaction begins at the morula stage (~E2.5), when adjacent cells form specialized attachments to each other and the mass of ~16 cells forms a tight clump of cells. Although all cells, or blastomeres, of the embryo possess near-identical developmental potential at this stage, there are now distinct biological differences between inner cells and outer cells of the morula (Cockburn and Rossant, 2010). The first irreversible lineage segregation event, or irreversible separation between cell types, occurs in the mouse by E3.5, when the embryo transitions from morula to the blastocyst. The newly formed blastocyst has two cell types, which are now set to give rise to distinct cell types in the subsequent embryo: outer cells now represent the nascent trophectoderm, which will generate extraembryonic tissues such as the placenta, while the cluster of cells in the inner cell mass (ICM) are now restricted to form only tissues of the embryo proper. The embryo also contains a large fluid-filled cavity called the blastocoel, formed by solute-pumping activity of the outer cells (Manejwala et al., 1989). The small group of inner cells, or pluripotent cells, is the central focus of this dissertation.

Now that the first lineage event has occurred, the floodgates to cellular specialization have opened. The next irreversible lineage segregation happens between E3.5 and E4.5 with the partitioning of the ICM into sub-populations that express either *Nanog* or *Gata6* (Chazaud and Yamanaka, 2016). Nanog-positive cells now represent the pluripotent cells of the epiblast, which will generate all the embryonic germ layers. Gata6-positive cells abut the epiblast cells to line the blastocoel, and they represent another extraembryonic tissue called the primitive endoderm (PrE). The PrE will specialize into the visceral endoderm, which emits inductive cues to help pattern the

embryo after implantation and contribute to the yolk sac, an important nutritive tissue for the post-implantation embryo (Rossant and Tam, 2009).

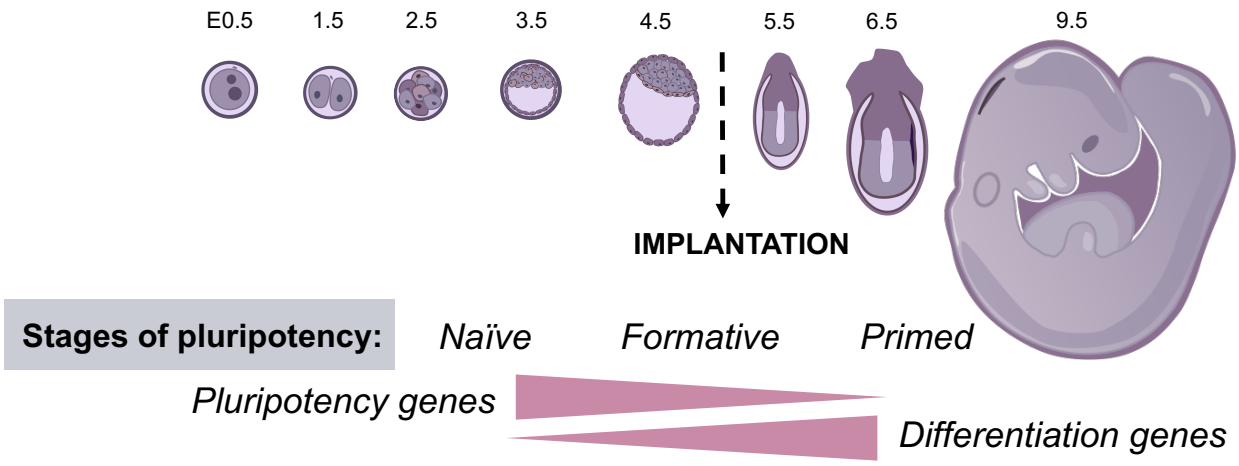

Figure 1. Timeline of early mouse development.
The fertilized egg at E0.5 undergoes cleavage division until ~E3.5, when the embryo becomes a blastocyst and begins to grow in volume. Three lineages are evident at E4.5: nascent trophectoderm (outer cell layer), primitive endoderm (line of cells touching blastocoel cavity), and the inner cell mass. The late blastocyst implants into the uterus ~E4.5-E5.5, at which point epiblast cells commence rapid mitoses. Gastrulation at the primitive streak begins at E6.5 (dark purple in figure), establishing the three germ layers and specifying primordial germ cells. Bottom: epiblast cells progress through stages of pluripotency, defined in large part by graded expression of pluripotency versus lineage genes. See text for details.

Whereas cell divisions of the cleavage-stage embryo occur slowly, early post implantation epiblast cells cycle extremely rapidly. To account for the rapid growth of the post-implantation mouse embryo, on average cells must divide once per ~5.1 hours. The actual division rate varies depending on cell type: epiblast cells located just anterior to the primitive streak divide at the astonishingly fast rate of *once per 2-3 hours* so that they can replenish the cells migrating through the primitive streak to form mesoderm and endoderm precursors (Snow, 1977). Thus, the embryo grows from about 150 cells at E5.5 to nearly 15,000 at E7.5 (Snow, 1981). Our lab has proposed that hypertranscription, or an elevation of a large part of the transcriptome, helps sustain

metabolic demands of the rapid-amplifying post-implantation epiblast (Guzman-Ayala et al., 2014; Percharde et al., 2017).

This short period of rapid growth poses several interesting developmental challenges. First, it places a critical demand on the mother. As the embryo implants and grows in size, it also extracts more nutrients from the uterine environment. Does it follow that embryos unlikely to give rise to viable offspring, either due to an intrinsic growth defect in the embryo or due to poor nutrient availability on the maternal side, should be pruned before implantation? Alternatively, is there a module in mammalian development that matches optimal uterine conditions to timing of embryonic development? (The answer to this question is yes—see, e.g., Bulut-Karslioglu et al. (Bulut-Karslioglu et al., 2016)). Second, what mechanisms help the embryo sustain this rapid embryonic growth? Finally, what mechanisms help control this rapid growth? Hypertranscription is a relative state, one that the embryo enters into and must exit from in order for development to proceed. We will consider aspects of these questions in chapters 1 and 2.

Model systems for early embryonic development

Pluripotency is difficult to study *in vivo* as it is transient and occurs in few cells. Much of our understanding of pluripotency derives from mouse embryonic stem (ES) cells cultured *in vitro*, first derived in 1981 (Evans and Kaufman, 1981; Martin, 1981). ES cells are defined by two major properties: the ability to generate both more of themselves (self-renewal) and three germ layers plus the germline of the developing embryo (pluripotency) (Bradley et al., 1984). Unlike pluripotency *in vivo*, pluripotent ES cells propagate essentially indefinitely under specific culture conditions. Since ES cells are also amenable to various manipulations and genetic perturbations and can be expanded, they make an ideal model for studying mechanisms of pluripotency.

An in-depth discussion of the emergence, maintenance, and exit from pluripotency is beyond the scope of this thesis. A major finding from mouse ES cell culture is that pluripotency exists along a spectrum, ranging from “naïve” to “primed” pluripotency, the latter term referring to

priming of lineage gene expression (Fig. 1) (Nichols and Smith, 2009). A defined culture medium supplemented with a Mek/Erk inhibitor and a Wnt agonist (two inhibitors, 2i) along with leukemia inhibitory factor (LIF) maintains a ground state of naïve pluripotency (Ying et al., 2008). This state is defined by low global levels of DNA methylation, low expression of lineage markers, and high expression of naïve pluripotency factors such as Nanog and Zfp42 (Rex1) (Marks et al., 2012). Molecularly, 2i ES cells resemble the ICM of the pre-implantation blastocyst (Boroviak et al., 2014). Culture in serum/LIF serves as a reasonable proxy for the fast-growing epiblast cells of the peri-implantation embryo described above. These cells show heterogenous morphology and expression of pluripotency, and at the molecular level they largely resemble the early post-implantation epiblast.

Primed pluripotency refers to the pluripotent cells of the post-implantation epiblast. These cells are functionally pluripotent, i.e. can generate all three germ layers, but they show reduced self-renewal and ability to contribute to embryo chimeras, characteristics reflecting their distinct molecular identity (Brons et al., 2007; Tesar et al., 2007). Embryos lose their ability to generate primed epiblast stem cells (EpiSCs) soon after the end of gastrulation, ~E8.25 (Kojima et al., 2014), corresponding to the loss of teratogenic potential (a proxy for pluripotency) observed by embryo transplant experiments (Beddington, 1983; Damjanov et al., 1971). Ectopic reactivation of Oct4 expression extends pluripotency up to E13.5 (Osorno et al., 2012), suggesting that vestiges of the developmental plasticity program linger past the normal interval of pluripotency. In sum, although it is difficult to study pluripotency *in vivo*, it is likely that ES cells reflect the trajectory of developmental competence in the developing embryo (Smith, 2017).

Other cellular models for pluripotency include primordial germ cells (PGCs), the precursors to the gametes (oocytes and sperm). In vitro, PGCs can give rise to Embryonic Germ Cells, which are functionally pluripotent. Additionally, under conditions of unrestrained growth PGCs can form germ cell carcinomas, including teratocarcinomas, or tumors composed of all three germ layers. These rare cancers were the source of embryonal carcinoma cells that served

as the first in vitro model for pluripotency and are still used today (Kleinsmith and Pierce, 1964). More recently, several groups have established methods to culture expanded-potential stem cells as a model of the totipotency-to-pluripotency transition, as these cells are capable of contributing to extraembryonic as well as embryonic tissues (Choi et al., 2017; Yang et al., 2017).

Within the last 15 years, another paradigm for pluripotency has emerged in the form of induced pluripotent stem cells (iPSCs). Building on decades of work that established that differentiated cell types can be induced to *de*-differentiate, or reprogram, and defined pathways of pluripotency came the discovery of pluripotency induction by ectopic expression of key pluripotency factors (Takahashi and Yamanaka, 2006). iPSCs hold great promise for a range of biomedical applications. They can be derived with relative ease from somatic human tissue, and thus they sidestep the need for human embryos, which have raised ethical concerns in the United States even though only discarded embryos from fertilization clinics are used for research.

The work presented in the subsequent chapters is aimed to explore mechanisms of chromatin regulation in early development, using mouse ES cells as a primary model system. Although my interest in pluripotency stems from a general interest in these cells that generate the entire embryo, they are important for other reasons. The transition from pluripotency to differentiation is a good model for cell fate transitions more generally, which are relevant to tissue development, homeostasis, and regeneration/repair. Moreover, pluripotent embryonic stem cells have essential parallels to other somatic and adult stem cells, especially those that involve activation and expansion of the stem cell compartment. They can also provide insight into cancer stem cells and other states of cellular quiescence.

Chapter 1:

The transcriptionally permissive chromatin state of embryonic stem cells is acutely tuned to translational output

Summary

A permissive chromatin environment coupled to hypertranscription drives the rapid proliferation of embryonic stem cells (ESCs) and peri-implantation embryos. We carried out a genome-wide screen to systematically dissect the regulation of the euchromatic state of ESCs. The results revealed that cellular growth pathways, most prominently translation, perpetuate the euchromatic state and hypertranscription of ESCs. Acute inhibition of translation rapidly depletes euchromatic marks in mouse ESCs and blastocysts, concurrent with delocalization of RNA polymerase II and reduction in nascent transcription. Translation inhibition promotes rewiring of chromatin accessibility, which decreases at a subset of active developmental enhancers and increases at histone genes and transposable elements. Proteome-scale analyses revealed that several euchromatin regulators are unstable proteins and continuously depend on a high translational output. We propose that this mechanistic interdependence of euchromatin, transcription and translation sets the pace of proliferation at peri-implantation and may be employed by other stem/progenitor cells.

Introduction

Stem and progenitor cells often display a distinct chromatin landscape associated with high levels of transcriptional activity (Gaspar-Maia et al., 2011; Percharde et al., 2017a). This chromatin state has been extensively studied in embryonic stem cells (ESCs) cultured in serum, which represent the rapidly proliferating pluripotent cells of the peri-implantation embryo (Smith, 2017). ESCs and pluripotent cells of the blastocyst display a remarkably decondensed chromatin pattern with low levels of compact heterochromatin (Ahmed et al., 2010; Efroni et al., 2008) and high levels of histone marks associated with transcriptional activity, such as H3/H4 acetylation and H3K4me3 (Ang et al., 2011; Lee et al., 2004). In agreement, ESCs are in a state of hypertranscription (Percharde et al., 2017a) that includes global elevation of nascent transcriptional output (Efroni et al., 2008).

Several factors have been implicated in the regulation of the permissive chromatin state of ESCs, including the histone acetyltransferases Tip60/p400 (Fazzio et al., 2008) and Mof (X. Li et al., 2012), the trithorax group protein Ash2l (Wan et al., 2013) and the ATP-dependent chromatin remodelers Ino80 (Wang et al., 2014) and Chd1 (Gaspar-Maia et al., 2009; Guzman-Ayala et al., 2014). We have shown that Chd1 binds broadly to the transcribed portion of the genome and promotes hypertranscription by both RNA Polymerases I and II in ESCs (Gaspar-Maia et al., 2009; Guzman-Ayala et al., 2014). This Chd1-driven state of elevated transcription is essential for growth of pluripotent epiblast cells of the mouse embryo at the time of implantation (Guzman-Ayala et al., 2014) and of hematopoietic stem/progenitor cells emerging from the endothelium at mid-gestation (Koh et al., 2015). These data indicate that a permissive chromatin associated with global hypertranscription is required for developmental transitions that involve rapid proliferation of stem/progenitor cells. While ESC chromatin has been the subject of many studies, the regulation of their permissive, hypertranscribing chromatin state has not been dissected on a

genome-wide scale. Moreover, a key question remains to be answered: how is hypertranscription set to the needs of rapidly proliferating pluripotent stem cells? In other words, how do pluripotent stem cells, such as ESCs, sense when not enough or too much transcription is occurring, and adjust their chromatin state accordingly?

We report here a genome-wide RNAi screen to systematically probe the permissive chromatin state of ESCs. Integrated analyses at the functional, chromatin, transcriptional and proteome level reveal that the growth capacity of ESCs, specifically the translational output, directly promotes a permissive chromatin environment, at least in part by maintaining the levels of unstable euchromatin regulators. The results reveal a dynamic positive feedback loop between permissive chromatin and translation that drives proliferation of pluripotent cells and may be tuned by signaling and availability of nutrients.

Results

A genome-wide RNAi screen identifies new regulators of euchromatin in ESCs

We sought to generate a live-cell reporter for euchromatin that would allow dissection of the dynamics and regulation of the euchromatic state of ESCs. The histone mark H3K4me3 is associated with active transcription, is directly and specifically bound by the double chromodomains of Chd1 (Flanagan et al., 2005) and is present at high levels in undifferentiated ESCs (Ang et al., 2011). We therefore generated mouse ESCs expressing a fusion between the Chd1 chromodomains and EGFP (referred to as Chd1chr-EGFP). As a control, we used ESCs expressing an Hp1α-EGFP fusion protein (Bulut-Karslioglu et al., 2014), which recognizes H3K9me3, a mark of constitutive heterochromatin. As anticipated, fluorescence in Chd1chr-EGFP ESCs displays a diffuse nuclear pattern, whereas it is restricted to DAPI-dense heterochromatin in Hp1α-EGFP ESCs (Figure S1A). Moreover, Chd1chr-EGFP signal positively correlates with endogenous Chd1 expression, H3K4me3 levels and nascent transcription (Figure S1B).

To assess whether the Chd1chr-EGFP reporter responds to manipulations of the chromatin state, we first knocked down Wdr5, a core component of MLL complexes that deposit H3K4me3 (Ang et al., 2011). Wdr5 knock-down completely depletes H3K4me3 levels and leads to a specific decrease in Chd1chr-EGFP reporter intensity within 3 days, with the Hp1α-EGFP reporter remaining unaffected (Figure S1C, D). Similarly, we observed a rapid decrease in Chd1chr-EGFP intensity along with reduced H3K4me3 levels upon retinoic acid (RA)-mediated differentiation of ESCs for 2 days, prior to any detectable changes in the activity of the Hp1α-EGFP reporter (Figure S1E, F). Taken together, these results indicate that the Chd1chr-EGFP reporter responds as expected to perturbations of the euchromatic landscape of ESCs.

To uncover regulators of the euchromatic state of ESCs, we next used the Chd1chr-EGFP ESCs to perform a genome-wide RNAi screen (Figure 1A). ESCs were infected with an ultra-complex lentiviral shRNA library comprised of ~30 shRNAs per gene. Cells were cultured for 3 days in serum/ leukemia inhibitory factor (LIF) medium and subsequently sorted into GFP^{low} and GFP^{high} populations by flow cytometry. Integrated shRNAs were isolated, amplified and sequenced. Differential enrichments in shRNAs per gene recovered from the GFP^{low} and GFP^{high} populations were used to estimate effect size, using HiTSelect (Diaz et al., 2015) (see methods for details). We previously used a similar approach to systematically identify barriers to human iPS cell generation (Qin et al., 2014). Applying this method at a 5% false discovery rate (FDR) cutoff, we identified 461 genes whose knockdown is associated with lower Chd1chr-EGFP fluorescence (Figure 1B. These genes are thus putative positive regulators of the euchromatic state of ESCs. In validation of the screen, this set of genes includes several previously described regulators of ESC chromatin, including Chd1 itself (Gaspar-Maia et al., 2009), Tip60/Kat5, p400 (Fazzio et al., 2008) and Mll4/Kmt2b (Denissov et al., 2014). Several other known euchromatin regulators, including Hira (Meshorer et al., 2006), Ino80 (Wang et al., 2014) and Hat1 (Nagarajan et al., 2013), are enriched at FDR<7.5% (Figure 1B).

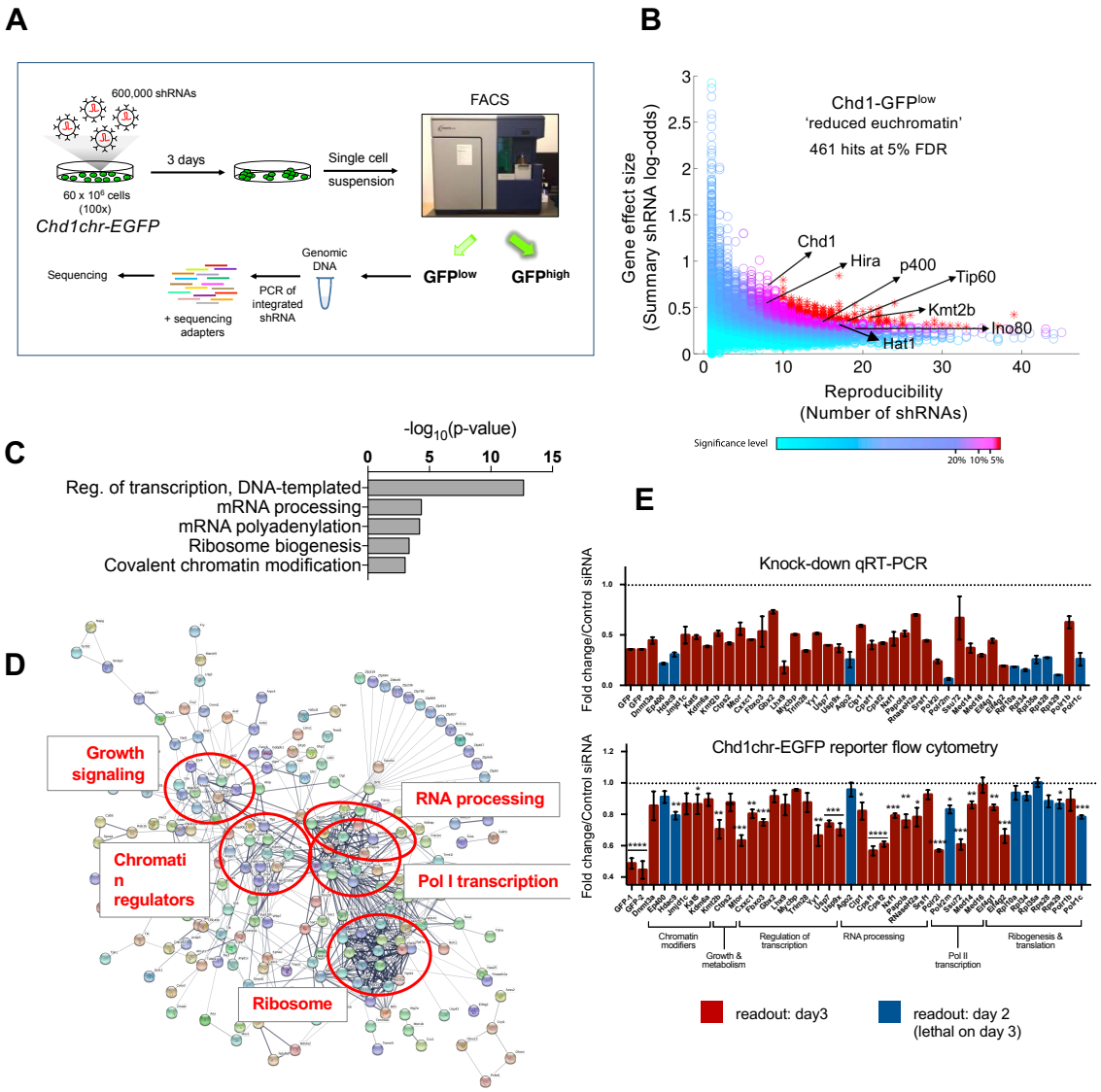

Figure 1.1. A genome-wide RNAi screen identifies regulators of euchromatin in ESCs. (A) RNAi screen workflow. (B) Results of the RNAi screen for the genes with shRNAs enriched in the GFP^{low} fraction. Each circle denotes a gene tested in the screen. Published regulators of open chromatin in ESCs are indicated by arrows. See Table S1 for the full screen results. (C) Gene ontology (GO) terms associated with significant RNAi screen hits. See Table S2 for the full list of GO terms. (D) Protein interaction network of significant RNAi screen hits, generated using STRING. (E) Secondary siRNA screen results. Genes were selected to represent each of the major pathways enriched in (C) and (D). Upper panel shows knockdown levels by qRT-PCR, normalized to scrambled siRNA control. Lower panel shows fluorescence level of the Chd1chr-EGFP reporter upon each knockdown. Readouts for both assays were measured on day 3 post-knockdown (red) or on day 2 (blue) if the knockdown was lethal by day 3. See methods and Table 1 for details. Error bars show mean ± standard deviation (SD) of 4 technical replicates. Graph is representative of 2 biological replicates. Statistical test performed is two-tailed t-test. *, p<0.05; **, p<0.01; ***, p<0.001; ****, p<0.0001.

To further refine the RNAi screen hits, we selected genes with robust RNA expression levels in ESCs (>1 FPKM in serum/LIF, (Bulut-Karslioglu et al., 2016)). The resulting 303 genes were clustered according to functional annotations (Gene Ontology, GO) and protein interaction data (Figure 1C and D. As expected, regulation of transcription and chromatin emerge as key processes modulating ESC euchromatin. Intriguingly, many factors involved in cellular growth and protein synthesis, notably RNA Polymerase (Pol) I complex components, ribosomal proteins and translation factors, are significantly enriched within screen hits. mTor, a key nutrient sensor and positive regulator of translation (Laplante and Sabatini, 2012), is the top hit in the screen. Validation of the RNAi screen was carried out by independent single gene knockdowns, using siRNAs that differ in sequence from the shRNAs used in the original screen. Importantly, knockdown of individual genes involved in translation and growth leads to significant decreases in Chd1chr-EGFP reporter intensity within 2-3 days, and in some cases the effect is stronger than loss of individual chromatin regulators (Figure 1E). These results suggest that translation and growth positively regulate euchromatin in ESCs.

Translation, mTor and Myc activities promote euchromatin in ESCs

We sought to expand upon the RNAi screen results using small molecule inhibitors of several growth-associated processes (Figure 2A). We found that inhibition of protein synthesis, mTor activity or Myc/Max complex activity leads to a rapid decrease in Chd1chr-EGFP fluorescence within 3 hours, while fluorescence of the Hp1α-EGFP reporter and an EGFP-only control remain unaltered during this acute time frame (Figure 2B and S2A). Activity of the Chd1chr-EGFP reporter closely follows the extent of translation inhibition as a result of each inhibitor treatment (Figure 2C and S2B). Chd1chr-EGFP fluorescence partially recovers by 24h of continuous inhibition, possibly due to a cellular adaptation to a lower growth state (Figure S2C). In contrast, inhibition of RNA Pol I or Pol II activity has no discernible effect on Chd1chr-EGFP fluorescence until 24h of treatment (Figure S2D). Chd1chr-EGFP signal recovers after release from translation

inhibition, with no impact on cell survival (Figure 2D and S2E). Co-treatment with the proteasome inhibitor MG132 partially rescues the decrease in Chd1chr-EGFP intensity induced by CHX, indicating that the Chd1chr-EGFP fusion protein itself may undergo partial turnover within this timeframe (Figure 2E, S2F). In contrast, Chd1chr-EGFP mRNA and chromatin-bound protein levels are only mildly affected after 3h of CHX treatment (Figure S2G, H). Taken together, the results suggest that the decrease in overall Chd1chr-EGFP fluorescence upon translation inhibition may be due to a combination of delocalization of the reporter protein within and away from the chromatin compartment, as well as protein turnover. Similar responses of the Chd1chr-EGFP reporter are observed in ESCs cultured in the presence of Gsk3 and Mek/Erk inhibitors (2i) (Figure S3), a condition that mimics the ground state of pluripotency (Ying et al., 2008). Thus, the Chd1chr-EGFP construct is a sensitive reporter that integrates the high levels of euchromatin, nascent transcription and nascent translation that characterize the undifferentiated state of ESCs. Given the higher levels of nascent transcription, steady-state RNAs (Bulut-Karslioglu et al., 2016) and Chd1chr-EGFP fluorescence in serum/LIF relative to 2i/LIF (Figure S3A), we focused on the acute impact of reduced translation on the chromatin state and transcription of ESCs in serum/LIF for the remainder of this study.

Euchromatic histone marks are rapidly depleted upon inhibition of translation

We next explored the dependency of euchromatin on translation in a reporter-free system, using wild-type ESCs. Notably, inhibition of translation using CHX for 3h leads to a reduction in the levels of histone marks associated with active promoters and enhancers, such as H3K4me3 and H3/H4 acetylation, without affecting overall histone H3 levels or repressive H3K9me2 (Figure 3A and S4A). We confirmed the global reduction in acetylated H4 by immunofluorescence and intracellular flow cytometry (Figure 3B and S4B). Pluripotent cells in the ICM of the E4.5 blastocyst respond similarly to a 3h inhibition of translation, with rapid reductions in H4K16ac and H3K4me3 (Figure 3C and S4C). H3K36me2 levels rise with increasing concentrations of CHX in a manner

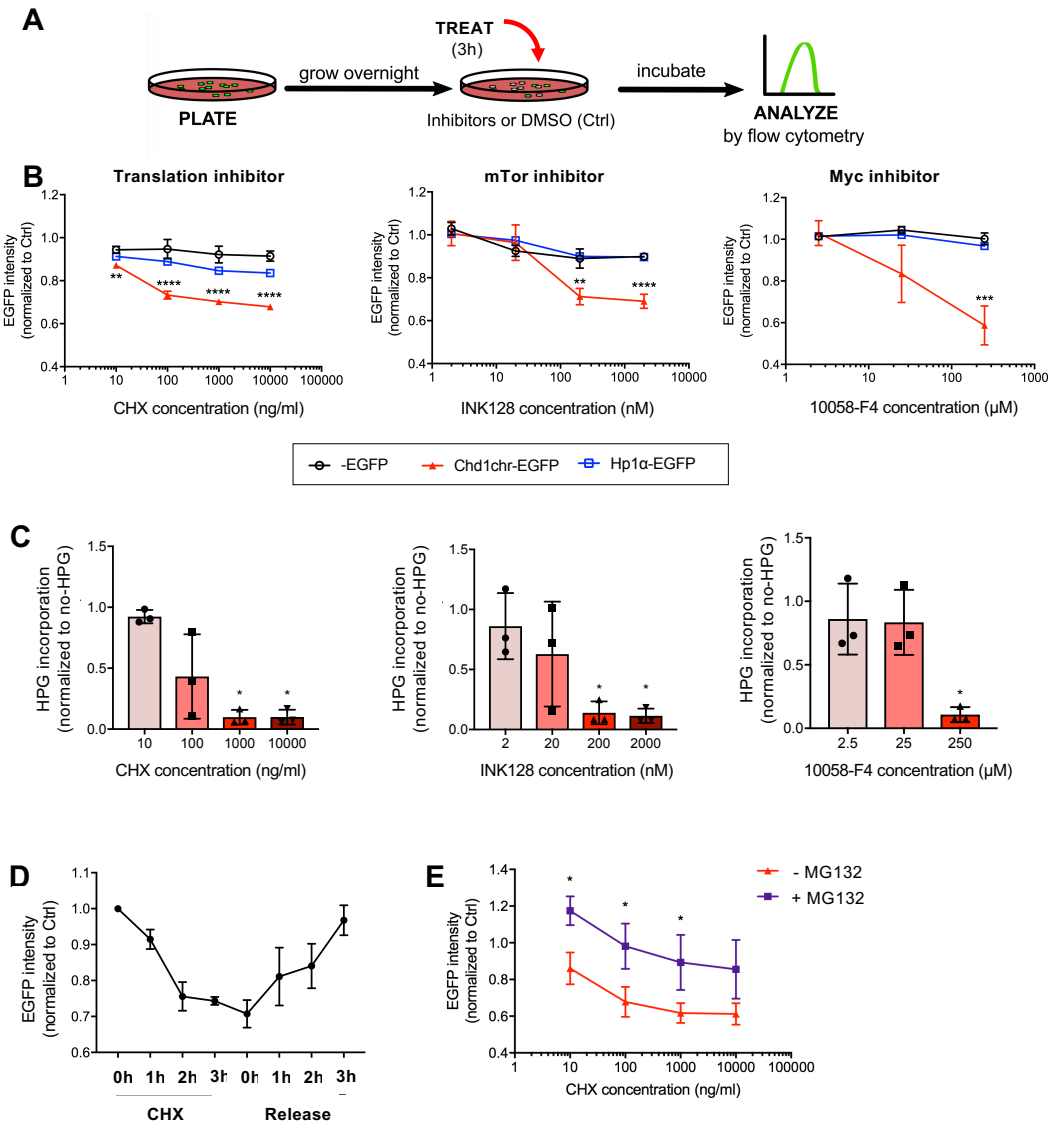

Figure 1.2. Translation, mTor and Myc dynamically regulate euchromatin reporter activity. (A) Schematic of small molecule-mediated inhibition. (B) Response of the Chd1chr-EGFP, Hp1α-EGFP and control EGFP ESCs to inhibition of translation, mTor, or Myc/Max at the indicated doses for 3 hours. Cells were treated with DMSO as control. Statistical significance was determined by Student's t-test. (C) Levels of nascent protein synthesis in wild-type ESCs by L-homopropargylglycine (HPG) incorporation during 3h inhibition of translation, mTor or Myc at the indicated doses. Median fluorescence intensity (MFI) was normalized to no-HPG controls and represented as a fraction of control (DMSO-treated) cells for each experiment. Each point represents a biological replicate. Error bars show mean ± SD. (D) Recovery of Chd1chr-EGFP reporter fluorescence following CHX (100 ng/ml) removal. (E) Proteasome inhibition partially rescues the effect of CHX on Chd1chr-EGFP intensity. Chd1chr-EGFP reporter ESCs were treated with DMSO or CHX ± MG132 (proteasome inhibitor) for 3h at the indicated doses. Graphs depicts mean ± SD of median fluorescence intensity (MFI) normalized to control cells of 4 technical replicates and is representative of 2 biological replicates (B, D) or 3 biological replicates (E). Statistical significance was determined by Student's unpaired t-test. *, $p<0.05$; **, $p<0.01$; ***, $p<0.001$; ****, $p<0.0001$.

anti-correlated with H3/H4 acetylation (Figure 3A and S4A), in agreement with the observation that H3K36me2 recruits histone deacetylases to prevent spurious transcription (B. Li et al., 2009).

Serum starvation, which is known to reduce translational output and mTor activity, also leads to a decrease in H3K4me3 and H3K27ac within 3-6 hours (Figure S4D). Direct mTor inhibition in ESCs and blastocysts using INK128 also leads to dynamic changes in histone acetylation within 3 hours. H3K27ac and H3K9ac levels acutely decrease upon mTor inhibition (Figure S4E, F). Although there can be specific differences in the responses between ESCs and ICM cells as well as between distinct manipulations, the overall response indicates that the euchromatic compartment is acutely sensitive to perturbations of translational output in pluripotent cells.

The analyses above indicate that histone acetylation is particularly sensitive to CHX and mTor inhibition. To gain insight into the genome-wide impact of inhibition of translation on histone acetylation, we performed ChIP-seq for H4K16ac after 3h of CHX treatment (Figure 3D-F and S4G, H). As previously described (X. Li et al., 2012), H4K16ac is concentrated around the TSSs of active genes and correlates well with expression levels (Figure 3D). We found that genes highly transcribed in ESCs undergo the strongest reductions in H4K16ac levels upon CHX, especially in the region immediately upstream of the TSS (Figure 3D). Ribosomal protein genes are particularly affected (Figure 3E and S4H). ChIP-qPCR confirmed these findings as well as the dose response of H4K16ac levels to the concentration of CHX initially observed by western blot (Figure 3A, F). By contrast, H3K4me3 is only slightly reduced at TSSs upon CHX treatment (Figure S4F). Thus, H4K16 acetylation at highly transcribed genes is acutely tuned to the levels of translational output in ESCs.

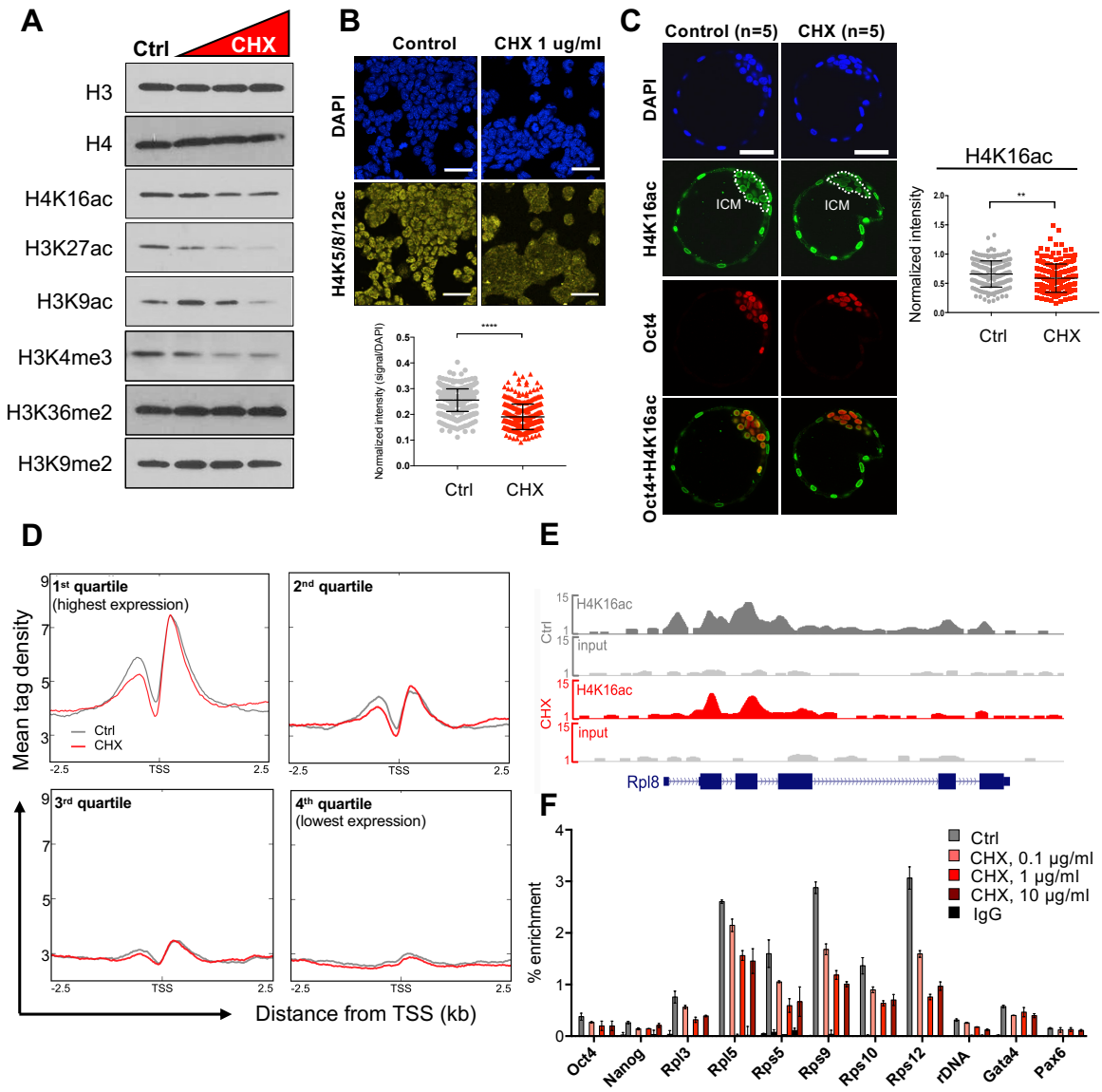

Figure 1.3. Inhibition of translation rapidly induces depletion of euchromatin marks in ESCs and blastocysts.

(A) Levels of indicated histone modifications upon 3 hours of CHX treatment at 0.1, 1 or 10µg/ml. See Figure S4A for biological replicates and quantifications. (B) Immunofluorescent detection and quantification of H4 acetylation (H4 K5/8/12) in DMSO- or CHX-treated ESCs. (C) Immunofluorescent detection of H4K16ac in control or CHX-treated (3 hours) E4.5 blastocysts and quantification in each Oct4+ cell (right panel). A representative z-section of each embryo is shown. (D) Correlation of CHX-induced H4K16ac changes with quartile of gene expression in ESCs (Bulut-Karslioglu et al., 2016). Profiles depict ChIP-seq tag density over annotated TSSs extended 2.5 kb upstream and downstream (3 hours CHX, 1 µg/ml). 1st quartile = highest expression, 4th quartile = lowest expression. (E) Representative genome browser view depicting H4K16ac in DMSO- or CHX-treated cells over the ribosomal protein gene *Rpl8*. (F) ChIP-qPCR documenting a dose-dependent response of H4K16ac following 3 hours of CHX. Error bars show mean ± SD of 3 technical replicates. Scale bars denote 50 µm. Statistical tests are two-tailed t-tests with Welch's correction. **, p<0.01; ****, p<0.0001.

Translational output positively feeds back into nascent transcription

The results above led us to ask whether acute inhibition of translation impacts nascent transcription. Remarkably, 3h inhibition of translation results in a ~60% decrease in global nascent transcription, assessed by measuring incorporation of the ribonucleotide analog 5-ethynyl uridine (EU) (Figure 4A). Nascent transcription of both Pol II-transcribed mRNA and Pol I-transcribed rRNA transcripts is ~90% decreased upon treatment with CHX for 3h (Figure 4B). Steady-state levels of the same mRNA and rRNA transcripts remain relatively stable within this time frame (Figure 4C). Thus, inhibition of translation, a manipulation often used to study protein stability and turnover, has an unexpected and rapid impact on nascent transcription in ESCs.

A reduction in nascent transcription could be due to increased pausing of RNA Pol II at the TSS or decreased occupancy at the TSS or along the gene body. ChIP-qPCR for total or elongating (S2p) RNA Pol II revealed that inhibition of translation leads to an overall decrease in polymerase occupancy at the TSS and gene body of highly expressed genes but not to increased promoter pausing (Figure 4D). We conclude that the decrease in nascent transcription is due to diminished recruitment or retention of RNA Pol II, which may be due to turnover of RNA Pol II subunits or of some of its recruiters/activators (see below). Similar to ESCs, pluripotent cells of the blastocyst display significant decreases in nascent transcription (Figure 4E) and elongating RNA Pol II levels (Figure 4F) upon 3h inhibition of translation. Taken together, our data document that acute inhibition of translation not only alters the euchromatin landscape but also leads to a strong repression of nascent transcription in pluripotent cells.

The permissive chromatin state of undifferentiated ESCs is particularly sensitive to acute inhibition of translation

The remarkably strong reduction in nascent transcription in ESCs upon inhibition of translation led us to further probe the status of pluripotency and differentiation markers. Oct4 and Nanog

protein levels are reduced upon 3h CHX treatment (Figure S5A, B), in agreement with the reported instability of these proteins (Buckley et al., 2012). However, a time-course analysis revealed that Oct4 and Nanog protein levels recover rapidly, within 1 hour after CHX withdrawal, in a pattern that closely resembles H4K16ac levels (Figure S5A, B) and Chd1chr-EGFP intensity (Figure 2D, S5B). Importantly, the steady-state mRNA levels of pluripotency factors and lineage commitment markers are not significantly changed upon 3h CHX (Figure S5C). Acute CHX treatment does not alter the ability of ESCs to differentiate into Embryoid Bodies (EBs), as EBs derived from DMSO- or CHX-treated cells show similar down-regulation of pluripotency markers and up-regulation of lineage markers (Figure S5D). Moreover, we have previously documented that long-term inhibition of mTor in ESCs and blastocysts is compatible with pluripotency (Bulut-Karslioglu et al., 2016). These results suggest that acute inhibition of translation has a profound impact on euchromatin and nascent transcription in ESCs but does not impair their developmental potential.

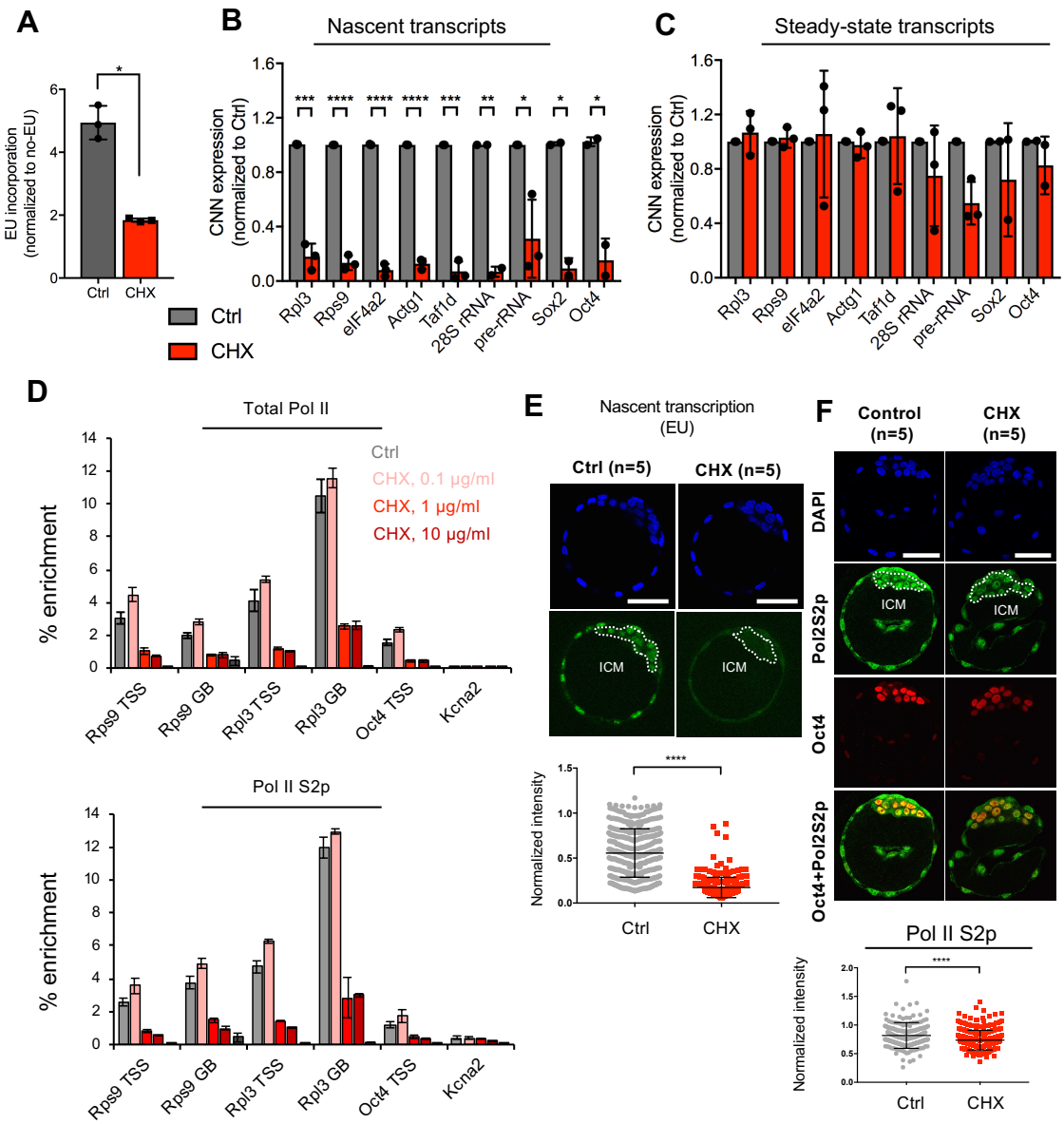

Figure 1.4. Nascent transcription is acutely sensitive to inhibition of translation in pluripotent cells.
(A) Levels of global nascent RNA synthesis assessed by EU incorporation in DMSO- or CHX-treated (3 hours) ESCs. MFI was normalized to no-EU controls for each experiment. Each point represents a biological replicate. (B) Nascent RNA capture followed by qRT-PCR in DMSO- or CHX-treated cells. Error bars show mean ± SD of 3 biological replicates. (C) Steady-state mRNA levels of genes shown in (B) in DMSO- and CHX-treated cells. No statistically significant differences were detected by Student's t-tests with the Holm multiple comparisons correction. (D) Enrichment of total or elongating (S2p, lower panel) RNA Pol II at TSSs and gene bodies (GB) of selected genes in DMSO- or CHX-treated cells. Graph depicts mean ± SD of 3 technical replicates and is representative of 2 biological replicates.

(E) Levels of nascent RNA synthesis assessed by EU incorporation in DMSO- or CHX-treated (3 hours) E4.5 blastocysts. A representative z-section of each embryo is shown. Scale bar denotes 50 μm. Right panel shows quantification of the EU signal in the ICM (indicated by white dotted lines). (F) Levels of elongating Pol II S2p in DMSO- or CHX-treated (3 hours) E4.5 blastocysts. Bottom panel shows quantification of the Pol II S2p signal in each Oct4+ cell. Statistical tests are two-tailed t-tests with Welch's correction when applicable. *, $p<0.05$; **, $p<0.01$; ***, $p<0.001$; ****, $p<0.0001$.

We next compared ESCs with non-pluripotent cells to assess the relative sensitivity of euchromatin and nascent transcription to translation inhibition across different cell types. We analyzed the levels of histone marks and nascent transcription as before in the following cell types: i) ESCs removed from LIF and treated with RA to induce differentiation for 3 days, ii) primary mouse embryonic fibroblasts (MEFs) derived from E12.5 embryos, and iii) multipotent neural stem/progenitor cells (NSPCs) isolated from the E12.5 mouse cortex (Hudlebusch et al., 2011). While ESCs rapidly deplete euchromatin marks and sharply reduce nascent transcription within 3 hours of CHX treatment (Figure 3A, 4A, S4A, S5E), these other cell types are overall less sensitive, with the exception of consistent reductions in H3K27ac (Figure S5E-G). Relative to ESCs, these other cell types have lower levels of basal nascent transcription, which displays a muted response to translation inhibition (Figure S5E-G). These results are in agreement with our observation that ESCs cultured in serum/LIF are hypertranscribing relative to a panel of multiple cell lines and tissues tested (Percharde et al., 2017b). We conclude that, while the response observed is not strictly specific to ESCs, their permissive, hypertranscribing chromatin state is particularly sensitive to acute inhibition of translation.

Several key euchromatin regulators are unstable proteins

The sensitivity of euchromatin to reductions in translational output in pluripotent cells, and the partial rescue of Chd1chr-EGFP reporter levels observed upon proteasome inhibition (Figure 2G), led us to hypothesize that key euchromatin regulators may be unstable proteins that require continuous synthesis. To test this, we quantitatively assessed proteome-wide changes in ESCs

after inhibition of translation using stable isotope labeling with amino acids in cell culture followed by mass spectrometry (SILAC-MS). We used a full block of translation (35 μg/mL of CHX) for either 1h or 3h to define the set of unstable proteins in ESCs (Figure 5A). We identified 4,078 unique proteins that were consistently depleted or enriched in the proteome at both time points of CHX treatment (Figure 5B). Cell cycle factors are over-represented in the depleted proteins, a finding that is expected given that cell cycle progression is predominantly regulated by short-lived proteins. Indeed, 3h inhibition of translation in ESCs moderately reduces the proportion of cells in S phase, with a concomitant increase in G_0/G_1 (Figure S6A, B). Fractionation of live cells in different stages of the cell cycle using a FUCCI reporter system (Nora et al., 2017) revealed that the impact of inhibition of translation on chromatin and transcription is observed throughout the cycle, although it is particularly evident in $S/G_2/M$ (Figure S6C-E). Regulators of chromatin, transcription and stem cell maintenance are also over-represented in the set of proteins rapidly depleted upon inhibition of translation (Figure 5B). Overall, these results are in agreement with protein turnover data from *S. cerevisiae* and mouse fibroblasts, where cell cycle and transcription factors were found to be preferentially unstable (Belle et al., 2006; Schwanhäusser et al., 2011). Interestingly, a block in translation leads to a relative enrichment in the proteome of proteins associated with translation and mRNA/rRNA processing (Figure 5B). The translation machinery is generally stable, and is potentially least affected by changes in protein synthesis rate (Schwanhäusser et al., 2011).

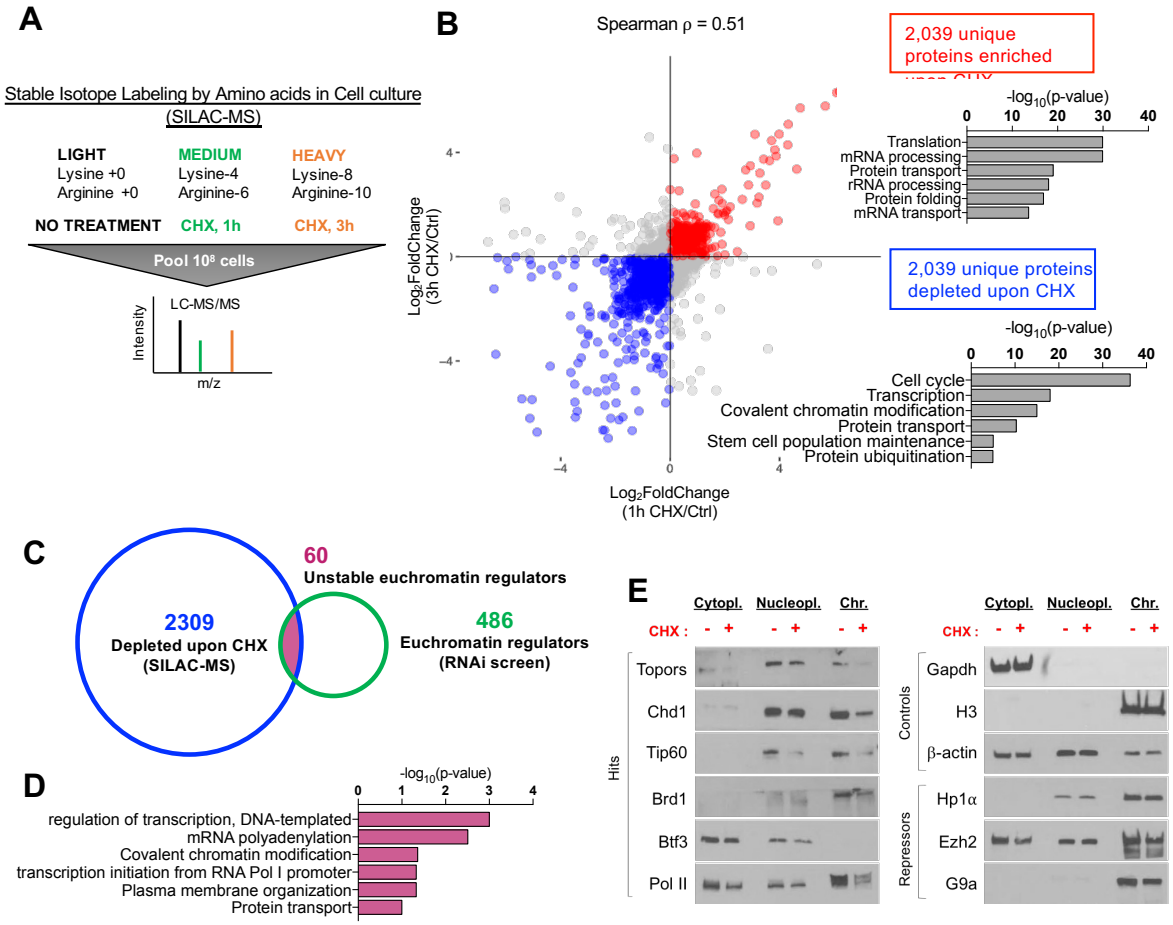

Figure 1.5. Key euchromatin regulators are unstable proteins that are rapidly depleted at the chromatin upon translation inhibition in ESCs.
(A) Schematic of SILAC-MS workflow. (B) Scatter plot for proteins detected by SILAC-MS following 1 or 3 hours of CHX treatment. CHX-enriched or -depleted proteins are shown in red or blue, respectively. Graphs show associated GO terms. (C) Venn diagram for the intersection of RNAi screen hits with unstable proteins as determined by SILAC-MS (blue set in B). 60 such genes were identified. (D) GO terms associated with the 60 overlapping genes in (C). (E) Western blots showing the abundance of indicated proteins in cellular fractions in DMSO- or CHX-treated (3 hours) cells. Left panel shows RNAi screen hits that are among the 60 proteins at the intersection shown in (C).

We next intersected the set of unstable proteins (Figure 5B, blue) with the RNAi screen hits (Figure 1B). This analysis yielded 60 proteins that are unstable euchromatin regulators (Figure 5C, D). They include several known regulators of euchromatin and transcriptional activation in stem and progenitor cells, including Chd1 itself (Gaspar-Maia et al., 2009; Guzman-Ayala et al., 2014; Koh et al., 2015), the Tip60-p400 acetyltransferase complex (Fazzio et al., 2008), and the Brd1 component of the MOZ/MORF acetyltransferase complex (Mishima et al., 2011). We validated a representative subset of unstable proteins by western blotting after treatment with 3h CHX (Figure 5E). Interestingly, RNA Pol II is also selectively depleted from the chromatin fraction upon CHX treatment, in line with ChIP experiments (Figure 4D). In contrast, control proteins such as H3, Gapdh and β-actin, as well as the heterochromatin regulators Hp1α, Ezh2 and G9a, remain largely unchanged upon 3h CHX treatment. Thus, several key euchromatin regulators of ESCs are preferentially unstable proteins *in situ*, providing a mechanism for the acute dependence of permissive chromatin and hypertranscription on translation.

A reduction in translational output rapidly deactivates developmental enhancers and primes transposable elements

Our studies to this point documented that a reduction in transcriptional output rapidly decreases the levels of activating histone marks and RNA Pol II at the promoters of highly expressed genes (Figures 3D-F, 4D), with a concomitant reduction in their nascent transcription (Figure 4B). However, the set of acutely unstable proteins in ESCs identified by SILAC-MS includes many sequence-specific transcription factors and chromatin regulators that are known to bind enhancers as well as promoters (e.g., Klf5, Gbx2, Zic1, Tip60/p400, Chd1, RNA Pol II, several Mediator subunits; see Figure 5). These results suggested that enhancer elements might also be sensitive to rapid shifts in translational output. We therefore carried out Assay for Transposase Accessible Chromatin with high throughput sequencing (ATAC-seq) to determine whether and how the landscape of chromatin accessibility in ESCs responds to acute (3h) inhibition of

translation (Figure S7A). We identified 454 regions that reproducibly lose accessibility and 734 regions that gain accessibility upon CHX treatment (Tables S7 and 8). Interestingly, most of these regions of differential accessibility are located 50-500 kb away from TSSs (Figure S7B).

Regions that become less accessible upon CHX treatment (CHX-lost) are associated with genes annotated with developmental functions (Figure 6A). To probe the chromatin environment of CHX-lost regions, we analyzed published datasets (see Methods). This analysis revealed that CHX-lost regions are active enhancers in wild-type ESCs (Calo and Wysocka, 2013), given their enrichment for DNase-hypersensitivity, H3K4me1, H3K27ac and p300 (Figure 6B). Thus, a subset of active enhancers associated with developmental functions in ESCs loses accessibility upon acute reduction in translational output. CHX-lost regions are highly enriched for DNA binding motifs of the transcription factors Klf4/5 and Zic1/3 (Figure 6B). Among those, Klf5 and Zic1 were detected at the protein level by SILAC-MS and are depleted upon 1h and 3h CHX treatment. Klf4 has previously been shown to be an unstable protein (Chen et al., 2005). Reduced accessibility at active developmental enhancers upon inhibition of translation may be due to turnover of both euchromatin regulators and specific transcription factors with functions during development.

Regions that become more accessible upon CHX treatment (CHX-gained) are generally not associated with any gene or functional signature, with the exception of histone clusters (Figure S7C). There is no significant accumulation of activating histone modifications on the majority of CHX-gained peaks. Rather, CHX-gained regions are embedded in domains of high levels of H3K9me3 (Figure 6C). We speculated that these regions might overlap genomic repeats. Indeed, CHX-gained peaks reside immediately upstream of long (~5kb) unmappable regions (Figure 6D). Moreover, ~50% and ~30% of CHX-gained peaks overlap with transposable elements (TEs) of the LINE1 and LTR families, respectively, and active subfamilies such as L1Md_T/F/A and IAP are particularly enriched (Figure 6E). Despite increased chromatin accessibility, the nascent

expression of histone clusters and TEs is still suppressed upon CHX treatment, albeit to a lesser extent than mRNAs from non-repetitive genes (Figure S7D, E). The gains in chromatin accessibility upon acute inhibition of translation may be due to the fact that these regions are enriched for AA/AT dinucleotides, which tend to repel nucleosomes (Valouev et al., 2011), and are marked by H3.3 and (acetylated) H2A.Z, histone variants associated with nucleosome instability (Jin et al., 2009) (Figure 6C). Taken together, our results reveal that the open chromatin landscape of ESCs is rapidly reprogrammed upon partial inhibition of translation, with decreased accessibility at active enhancers associated with development and increased accessibility at histone genes and transposable elements.

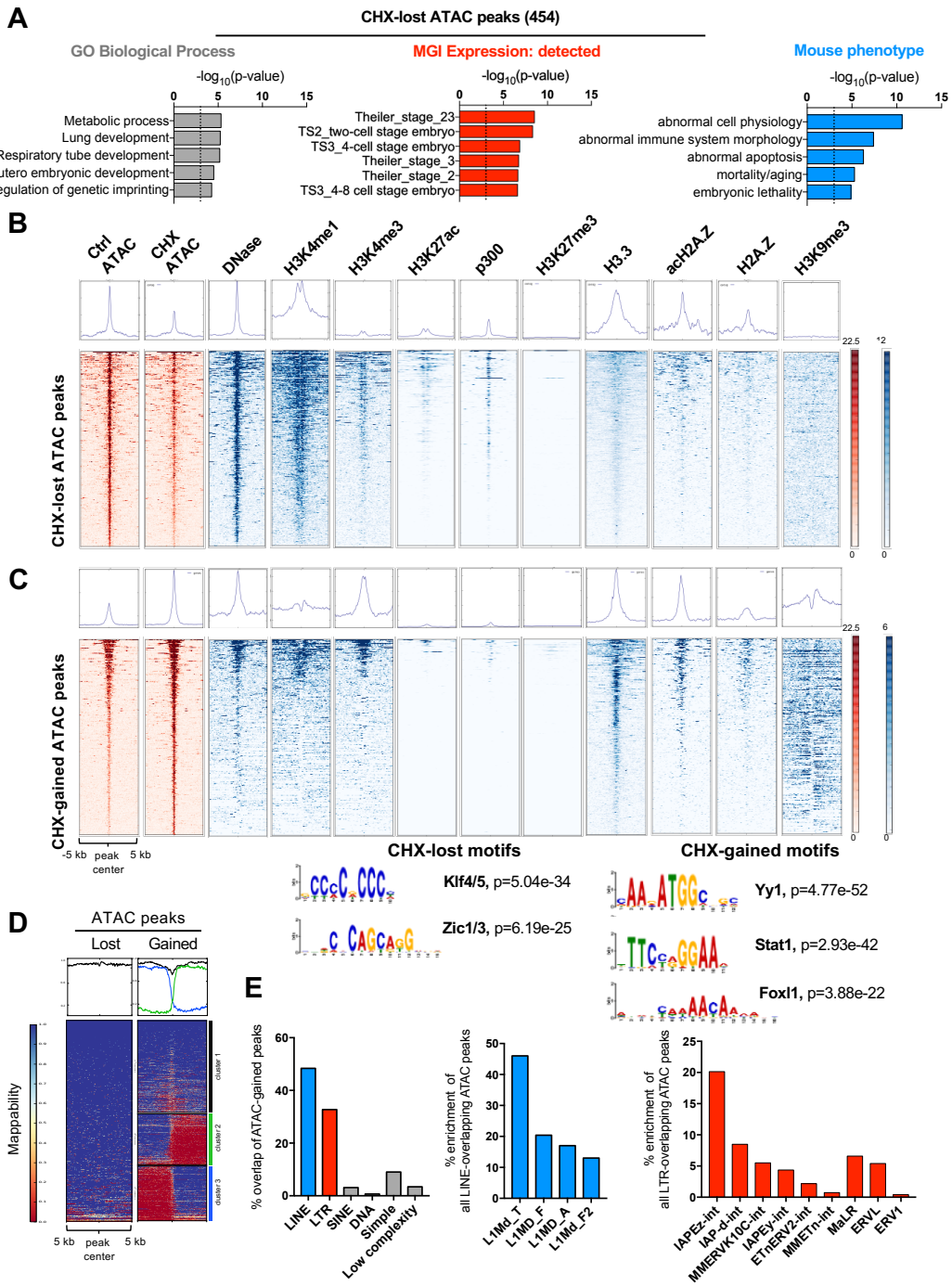

Figure 1.6. Inhibition of translation in ESCs induces reprogramming of chromatin accessibility at developmental enhancers, histone genes and transposable elements. (A) Functional terms associated with regions with loss of chromatin accessibility, determined by ATAC-seq, upon CHX treatment for 3 hours. (B, C) Heatmaps for enrichment of indicated histone modifications, variants and DNase-accessible sites on CHX-lost (B) or CHX-gained (C) ATAC-seq peaks. Right panels show enriched DNA motifs. (E) Heatmaps showing levels of mappability of CHX-lost or CHX-gained ATAC-seq peaks. The CHX-gained heatmap is divided into three clusters to denote regions of distinct mappability. (F) Enrichment of repetitive elements over CHX-gained ATAC-seq peaks.

Discussion

We report here that the transcriptionally permissive chromatin state of ESCs is acutely tuned to the levels of translational output. Our findings point to a positive feedback loop between chromatin and translation, whereby the permissive, hypertranscribing chromatin state in ESCs not only promotes an elevated translational output but also depends directly on such elevated translation (Figure 7A). We propose that this feedback loop, in turn, sets the rapid pace of proliferation in ESCs and of embryonic growth at peri-implantation.

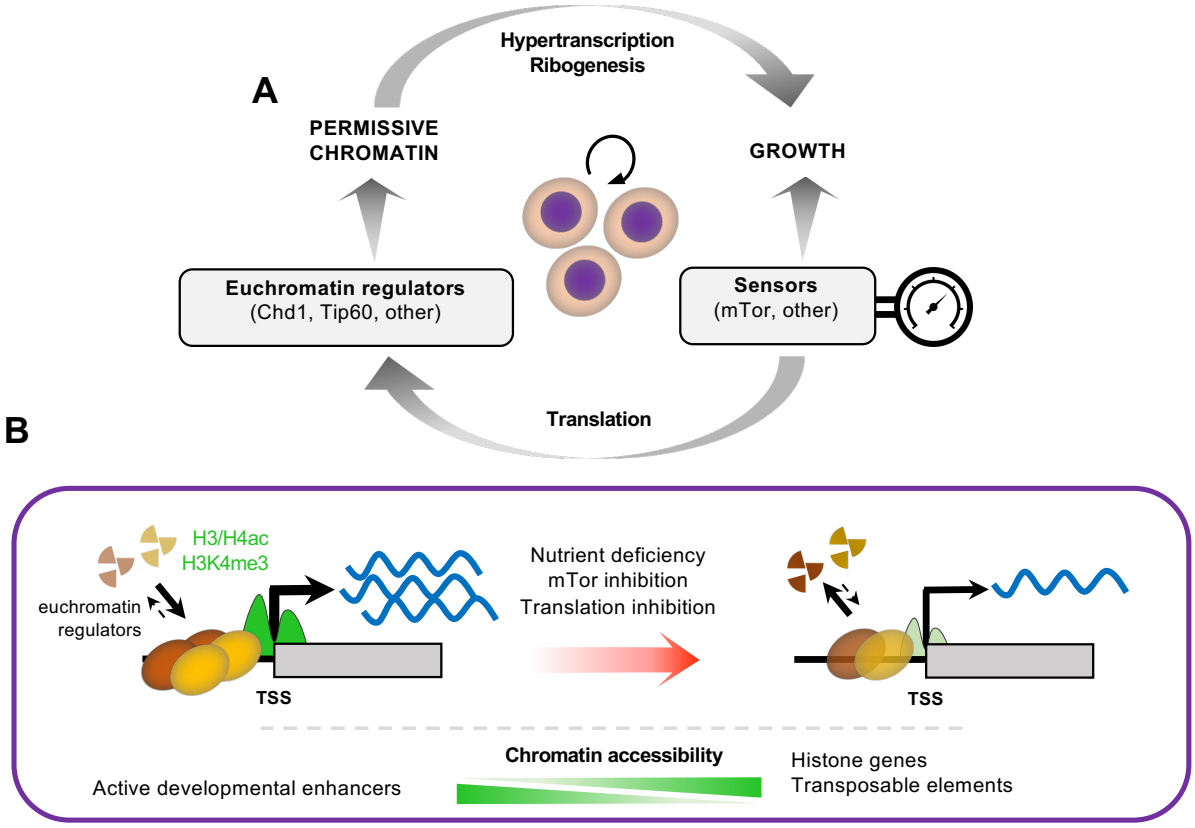

Figure 1.7. Proposed model for the dynamic feedback between translation, chromatin and transcription in ESCs.
(A) The permissive chromatin state of ESCs promotes growth by sustaining hypertranscription and ribogenesis, whereas growth promotes the permissive chromatin state by sustaining high levels of translational output. Signaling and nutrient sensors such as mTor act as rheostats of this positive feedback loop. (B) The permissive chromatin state of ESCs responds rapidly to changes in translational output, in part due to the instability of euchromatin regulators. See Discussion for details.

Our results document a remarkably fast response of euchromatin and transcription to perturbations of translation output in ESCs, whereas heterochromatin and its regulators appear to be more stable overall (Figure 7B). Histone acetylation may be a key integrator of the status of translation and nutrient availability in this context, given the instability of components of histone acetyltransferase complexes such as Tip60, p400 or Brd1 (Figure 5E) and the fact that histone acetylation is directly dependent on the glycolytic state of undifferentiated ESCs (Moussaieff et al., 2015). Moreover, histone acetylation controls the highly dynamic nature of euchromatin, but not heterochromatin, in ESCs (Melcer et al., 2012). The intricate relationship between different histone modifications associated with transcription, notably histone acetylation and H3K4me3 (Crump et al., 2011), likely contributes to propagate the impact of altered translational output across various layers of regulation of chromatin activity.

Considering the profound changes in levels of activating histone marks and nascent transcription after 3 hours of inhibition of translation, it is interesting that the overall landscape of chromatin accessibility at promoters and gene bodies is largely unaffected. These results suggest that, on a short time scale, nucleosome occupancy in these regions is relatively resistant to changes in chemical modifications of histones and RNA Pol II activity. At distal regions, acute inhibition of translation in ESCs induces loss of chromatin accessibility at a subset of developmental enhancers and gain at repeats. The net effect may be to limit spurious differentiation and prime a return to the high level of expression of histone genes and repeat elements that is typical of proliferating ESCs (Efroni et al., 2008), once translational output is re-established. In addition, it is possible that reduced translational output primes the chromatin of conserved LINE1 and LTR elements for retrotransposition, potentially as a stress response. It will be interesting to determine to what extent ESCs that recover from inhibition of translation are distinct from normally growing ESCs, including with regards to chromatin accessibility and TE activity.

While our findings document that protein instability is a key tuner of the euchromatic state of hypertranscription in ESCs, other layers of regulation such as RNA stability, signaling or metabolism are expected to play important roles. It is also important to note that reductions in translational output can have effects not limited to chromatin and transcription, notably on the cell cycle. Within 3 hours of inhibition of translation, the proportion of ESCs in S phase is reduced, with an accumulation of cells in G_0/G_1 (Figure S6A, B). Nevertheless, for the levels of CHX used here the proportion of ESCs in S phase remains high (40-60%) and, importantly, nascent transcription and euchromatin marks are reduced upon inhibition of translation in both populations of G_0/G_1 and $S/G_2/M$ cells (Figure S6D, E). Interestingly, histone acetylation is required for efficient activation of replication origins during S phase (Unnikrishnan et al., 2010), and loss of histone acetylation drives yeast in nutrient-limiting conditions to enter quiescence (McKnight et al., 2015). In addition, the major H4K16 acetyltransferase MOF directly binds to and maintains the expression of genes required for cell cycle progression in proliferating mouse embryonic fibroblasts (Sheikh et al., 2016). Such links between euchromatic histone marks, transcription, translation, glycolysis and cell cycle may serve to coordinate overall biosynthesis with rapid proliferation in ESCs in vitro and epiblast cells in vivo.

The highly dynamic levels of euchromatin regulators may be due both to the reported inefficiency of translation in ESCs (Sampath et al., 2008) and to control by the ubiquitination and sumoylation pathways (Buckley et al., 2012; Vilchez et al., 2012). Several proteins with roles in these pathways are hits in the RNAi screen. For example, Usp9x is a deubiquitinase required for early development (Pantaleon et al., 2001) and self-renewal of NSPCs (Jolly et al., 2009). Topors is an E3 SUMO/Ubiquitin ligase that targets chromatin modifiers (Pungaliya et al., 2007) and is itself unstable in ESCs (Figure 5E). These and other proteins may help coordinate an euchromatic/transcriptional response to perturbations in translational output via modification of chromatin factors. It will be of interest to dissect the role of the instability of specific euchromatin

regulators such as Tip60/p400 or Chd1, as well as the function of ubiquitination/sumoylation factors such as Usp9x or Topors, in maintaining the permissive chromatin state of ESCs.

The positive feedback loop between permissive chromatin and translational output identified here may drive rapid proliferation of undifferentiated pluripotent cells, but it cannot be perpetuated indefinitely. In this regard, it is noteworthy that mTor is the top hit in the RNAi screen. mTor may directly regulate permissive chromatin and hypertranscription, given its role in promoting histone hyperacetylation at the nucleolus and high levels of ribosomal RNA transcription (Tsang et al., 2003). Moreover, it was the identification of mTor as a key regulator of permissive chromatin in this study that led us to the finding that inhibition of mTor induces a reversible state of *hypo*transcription and developmental pausing in blastocysts and ESCs (Bulut-Karslioglu et al., 2016). The centrality of mTor in growth signaling, nutrient sensing, ribogenesis and translational regulation (Laplante and Sabatini, 2012) make it an ideal rheostat for the positive feedback between euchromatin and translation during development.

Beyond ESCs and early embryos, hypertranscription is employed by germline and somatic stem/progenitor cells during phases of growth and regeneration (Percharde et al., 2017b; 2017a). Recent studies have shown that rapidly expanding lineage-committed progenitors often have elevated levels of transcriptional and translational outputs relative to their parental stem cells (Blanco et al., 2016; Signer et al., 2014; Zhang et al., 2014). In contrast, a global reduction in translational output is characteristic of dormant states, such as developmental pausing (Bulut-Karslioglu et al., 2016; Scognamiglio et al., 2016) or hibernation (Frerichs et al., 1998) and can be induced by environmental stresses including nutrient deprivation, hypoxia, viral infection or exposure to toxins (Laplante and Sabatini, 2012; Olsnes, 1972). We speculate that the acute dependence of euchromatin and transcription on translational output may be a recurrent feature in stem/progenitor cells that is modulated by environmental perturbations.

Supplemental Figures

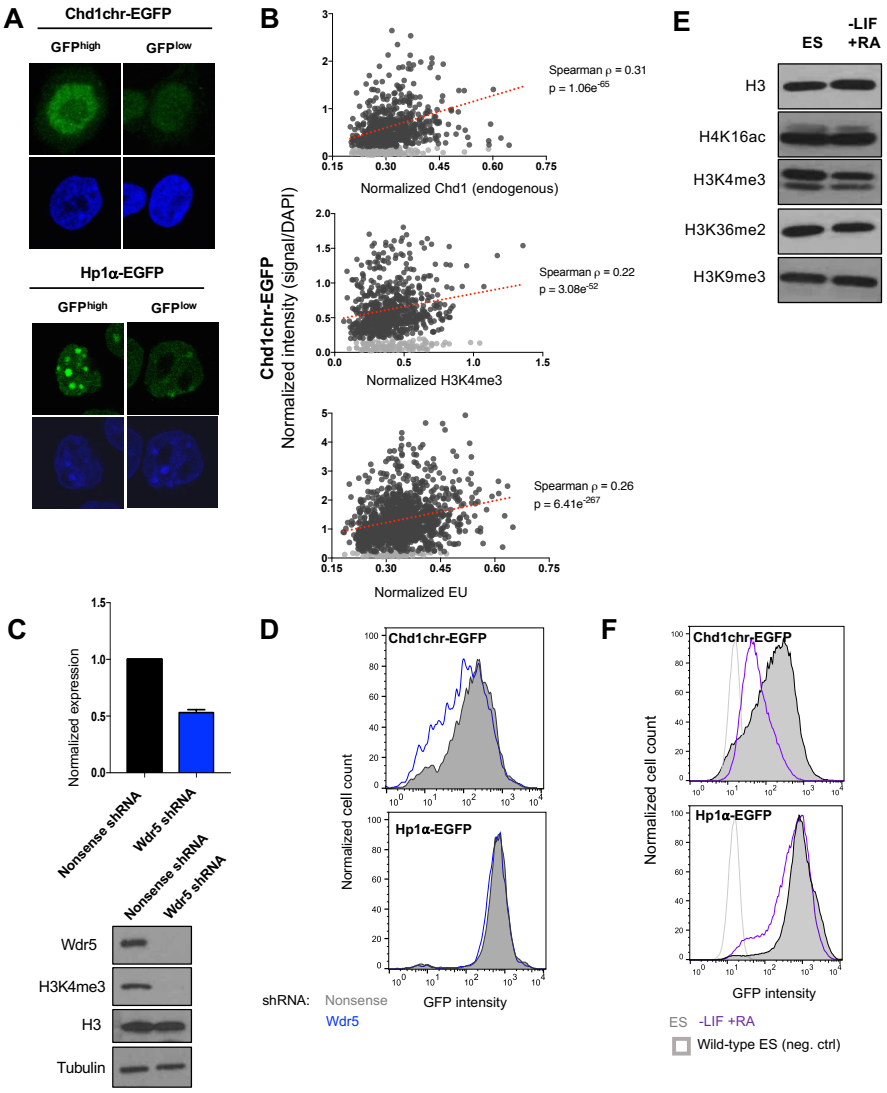

Figure S1.1. Characterization of Chd1chr-EGFP and Hp1α-EGFP reporters in ES cells. (A) Fluorescence imaging of the Chd1chr-EGFP and Hp1α-EGFP reporters. (B) Correlation of Chd1chr-EGFP reporter signal with endogenous Chd1, H3K4me3 and nascent transcription (EU). Single-cell quantification of immunofluorescence for the indicated markers was performed and normalized to DAPI. Cells with background levels of EGFP signal (grey points) were removed from the analysis. (C) mRNA and protein expression levels of Wdr5, a component of the MLL1 complex that deposits H3K4 methylation, upon transduction of ES cells with non-targeting or Wdr5-specific shRNAs. (D) Flow cytometry analysis of Chd1chr-EGFP and Hp1α-EGFP reporter fluorescence levels upon knock-down of Wdr5. Fluorescence was assayed 3 days post-transduction. (E) Analysis of chromatin marks upon RA-mediated differentiation of ES cells for 2 days. ES cells grown in serum/LIF were used as control. (F) Analysis of reporter fluorescence upon RA-mediated differentiation of ES cells for 2 days. ES cells grown in serum/LIF were used as control. Wild-type, non-fluorescent ES cells were used as negative controls for flow cytometry. A minimum of two biological replicates were performed for all experiments.

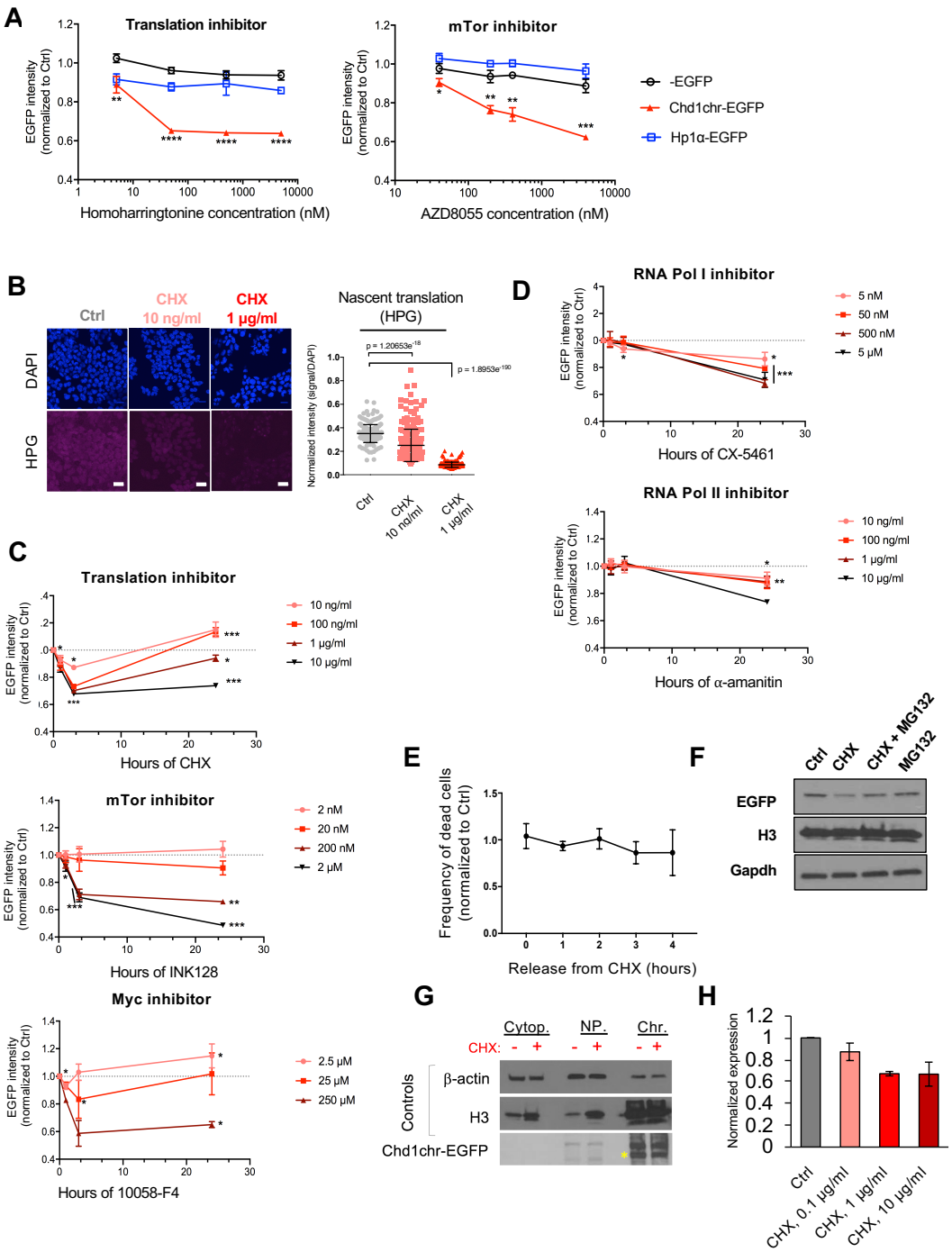

Figure S1.2. Characterization of the reporter response to small molecule-mediated inhibition of indicated cellular pathways.

(A) Response of the Chd1chr-EGFP, Hp1α-EGFP and control EGFP ES cells to inhibition of translation or mTor for 3 hours using independent inhibitors from those in Figure 2. Cells were treated with DMSO as control. Graphs show mean ± SD of 3-4 technical replicates and are representative of 2 biological replicates. Statistical significance was determined by a two-tailed Student's t-test.

(B) Fluorescence imaging of nascent translation by HPG incorporation upon DMSO or CHX treatment. Scale bars represent 20 μm. Right panel shows quantification of HPG signal. Statistical analysis performed is Mann Whitney *U* test. Error bars represent mean ± SD of at least 3 technical replicates. (C) Chd1chr-EGFP reporter fluorescence levels upon treatment with translation, mTor and Myc inhibitors for up to 24 hours. Cells were treated with DMSO as control. (D) Chd1chr-EGFP reporter fluorescence levels upon treatment with varying doses of Pol I and Pol II inhibitors for up to 24 hours. Cells were treated with DMSO as control. (E) Assessment of cell death of CHX-treated ES cells by SYTOX Blue incorporation. Error bars show mean ± SD of 4 technical replicates and are representative of at least 3 biological replicates. (F) Partial rescue of Chd1chr-EGFP fusion protein levels in whole-cell extracts upon inhibition of translation (CHX) ± inhibition of the proteasome (MG132). Error bars show mean ± SD of 2 biological replicates. Statistical tests are two-tailed t-test with Welch's correction when applicable. **, ***, **** = $p<0.01$, 0.001, 0.0001. (G) Chd1chr-EGFP protein levels in the cytoplasm, nucleoplasm and chromatin upon DMSO or CHX treatment (1 mg/ml) for 3 hours. Asterisk denotes the specific band with correct molecular weight. (H) Chd1chr-EGFP mRNA expression levels upon DMSO or CHX treatment for 3 hours. Error bars show mean ± SD of 3 technical replicates. Graph is representative of 2 biological replicates.

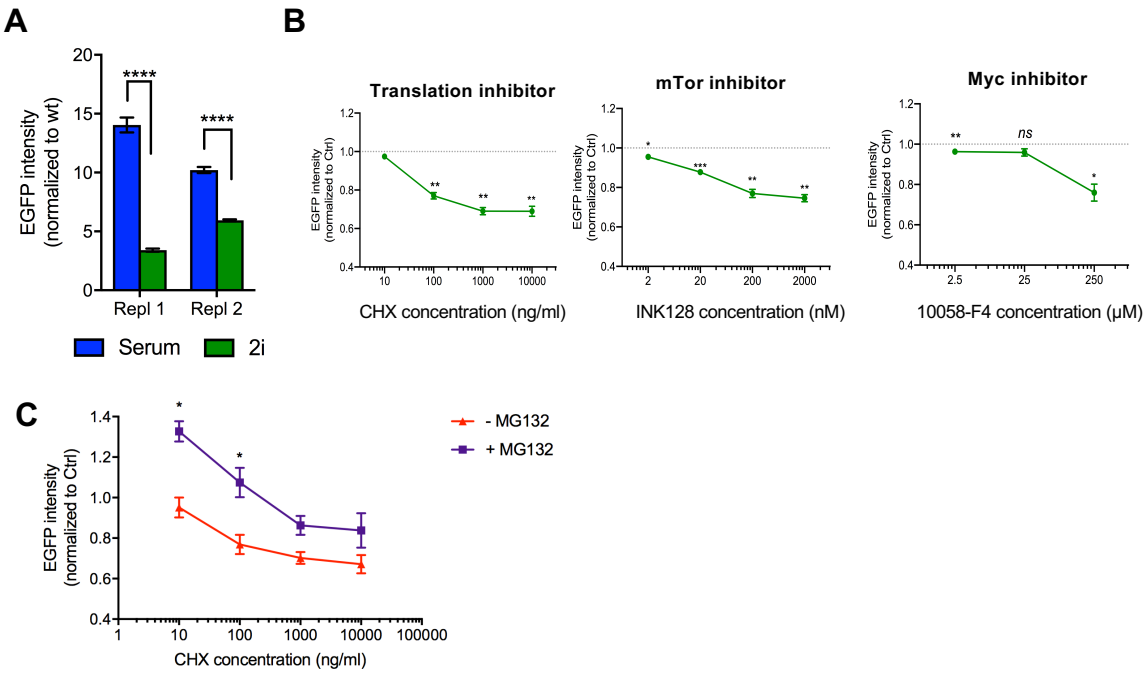

Figure S1.3. Reporter expression and sensitivity to inhibition of translation and growth pathways in 2i conditions.
(A) EGFP reporter expression in cells cultured in 2i or serum conditions. Fluorescence signal was normalized to wild-type (non-fluorescent) E14 cells. Error bars show mean ± SD of at least 8 technical replicates. (B) Normalized fluorescence levels of the Chd1chr-EGFP reporter in 2i/LIF upon small molecule-mediated inhibition of indicated pathways for 3 hours. (C) Normalized fluorescence levels of the Chd1chr-EGFP reporter in 2i/LIF upon partial rescue of the effects of CHX ± proteasome inhibition by MG132. Data represent mean ± SD of 2 biological replicates. *, **, *** = p<0.01, 0.001, 0.0001; ns = not significant.

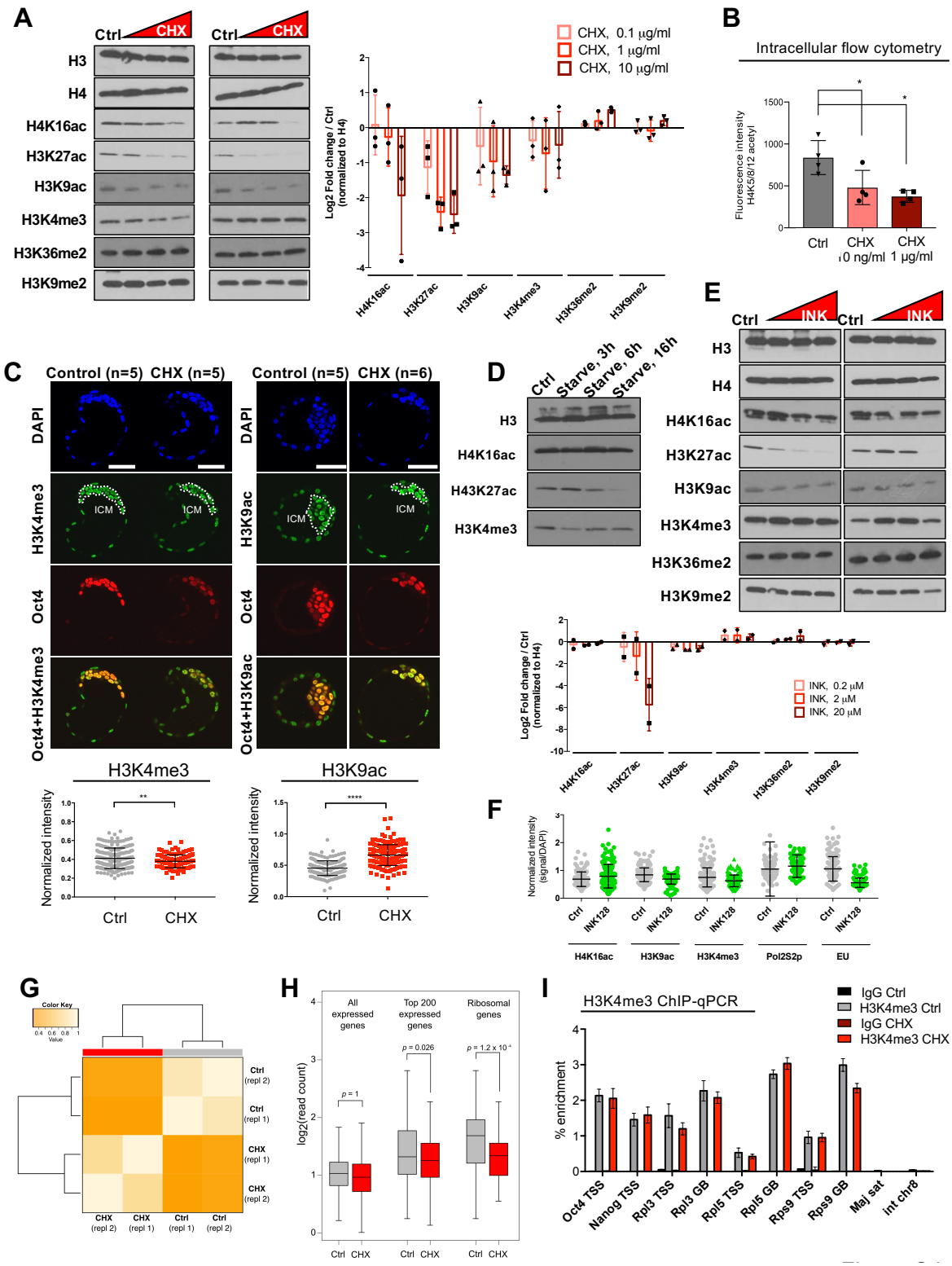

Figure S1.4. Chromatin response to inhibition of translation in ES cells and blastocysts. (A) Biological replicates of the western blot analysis shown in Figure 3A. Right panel shows quantification of the 3 biological replicates.

(B) Intracellular flow cytometry analysis of H4 acetylation (H4K5,8,12) in DMSO- or CHX-treated (3 hours) ES cells. Data shown are representative of 2 biological replicates. Statistical significance was determined by Mann Whitney *U* test. **** = $p<0.0001$. (C) Immunofluorescent detection of H3K4me3 and H3K9ac in control or CHX-treated (3 hours, 1 mg/ml) E4.5 blastocysts. Scale bars denote 50 μm. Bottom panels show quantification of the H3K4me3 or H3K9ac signal in each Oct4+ cell. Statistical significance was determined by Welch's two tailed t-test. **, *** = $p<0.01$, 0.001. (D) Western blot analysis of euchromatin marks in response to serum starvation for the indicated durations. Histone extracts from unstarved cells were used as controls. Figure represents two biological replicates. (E) Western blot analysis of euchromatin and heterochromatin marks in response to 3h treatment with the mTor inhibitor INK128. Data are quantified and reported as in (A). (F) Quantification of immunofluorescence staining of chromatin marks and nascent transcription (EU) in E4.5 blastocysts incubated with INK128. Blastocysts were treated as in Figure 3C. (G) Heatmap of H4K16ac ChIP-seq replicate correlation at the top 1000 most highly expressed genes in ES cells. (H) H4K16ac ChIP-seq read abundance over all expressed genes or gene subsets. (I) ChIP-qPCR for H3K4me3 enrichment over TSSs and gene bodies in DMSO- or CHX-treated cells (1 μg/ml, 3 hrs). Error bars show mean ± SD of 3 technical replicates. Graph is representative of 2 biological replicates.

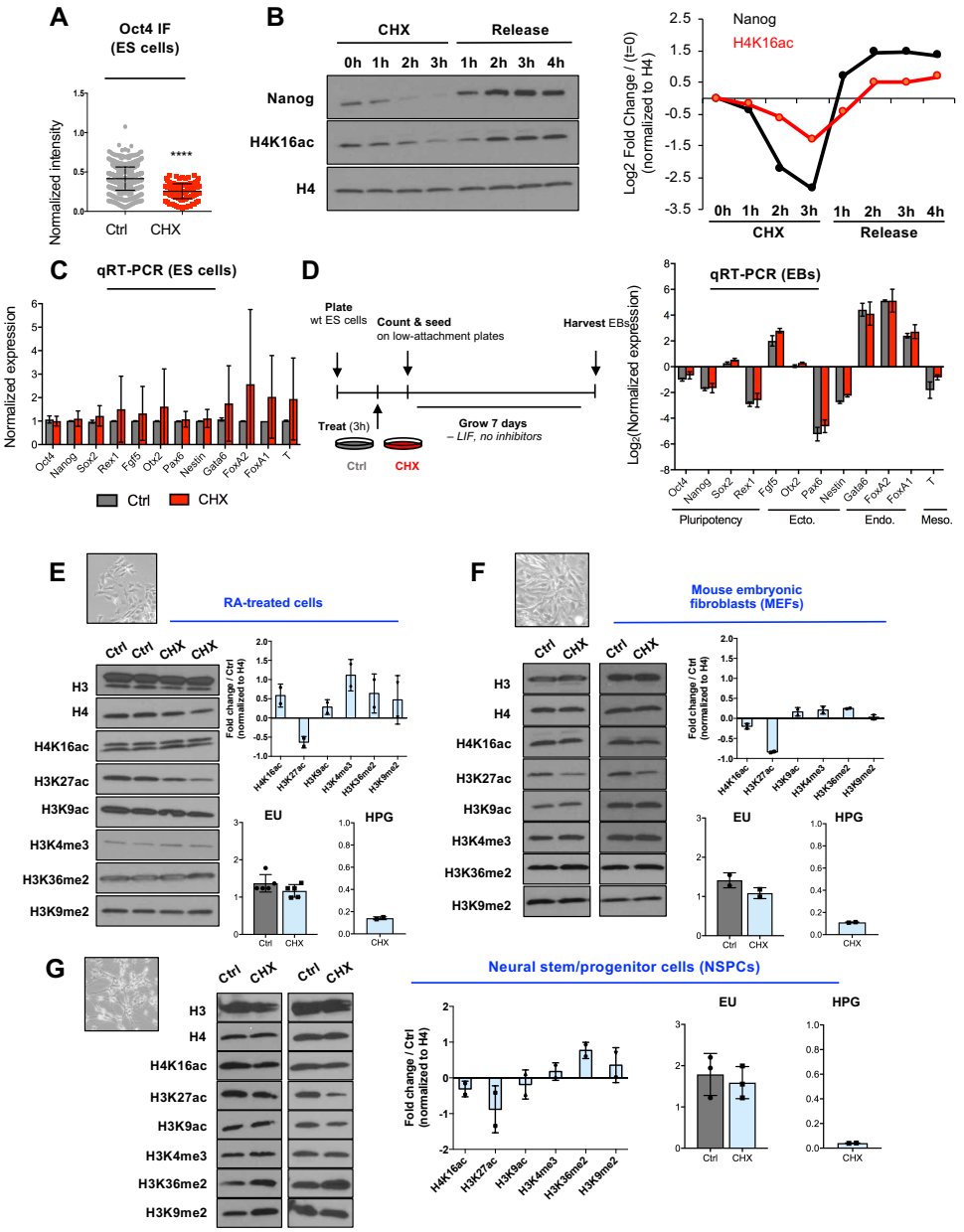

Figure S1.5. Effects of translation inhibition on ES cell pluripotency and on non-pluripotent cells.

(A) Quantification of Oct4 immunofluorescence in wild-type ES cells treated with DMSO or 1 µg/ml CHX for 3 hours. (B) Western blot analysis and quantification of Nanog, Oct4 and H4K16ac levels during addition of and release from CHX. (C) Cell number normalized qRT-PCR analysis of pluripotency and lineage markers in ES cells upon 3h of CHX. Data were normalized to Ctrl (DMSO). Error bars show mean ± SD of at least 2 biological replicates, each the mean of 3 technical qPCR replicates. No significant differences were detected by Student's t-test with multiple testing correction. (D) Schematic and results of acute CHX treatment and differentiation of wild-type ES cells into Embryoid Bodies (EBs). qRT-PCR analysis revealing no differences in pluripotency gene repression and lineage marker induction in EBs derived from ES cells treated for 3h with DMSO or CHX.

(Ecto. = ectoderm, Endo. = endoderm, Meso. = mesoderm). Data were normalized to the average of *Ubb* and *Rpl7* and are reported as $\log_2$-fold change relative to wild-type ES cells. Error bars show mean ± SD of 2 biological replicates, each the mean of 3 technical qPCR replicates. No significant differences were detected by Student's t-test with multiple testing correction. (E) Analysis of the chromatin, transcriptional, and translational responses to CHX in RA-treated ES cells. (F) Analysis of the chromatin, transcriptional, and translational responses to CHX in primary mouse embryonic fibroblasts (MEFs). (G) Analysis of the chromatin, transcriptional, and translational responses to CHX in neural stem/progenitor cells (NSPCs) isolated from E12.5 mouse cortex.

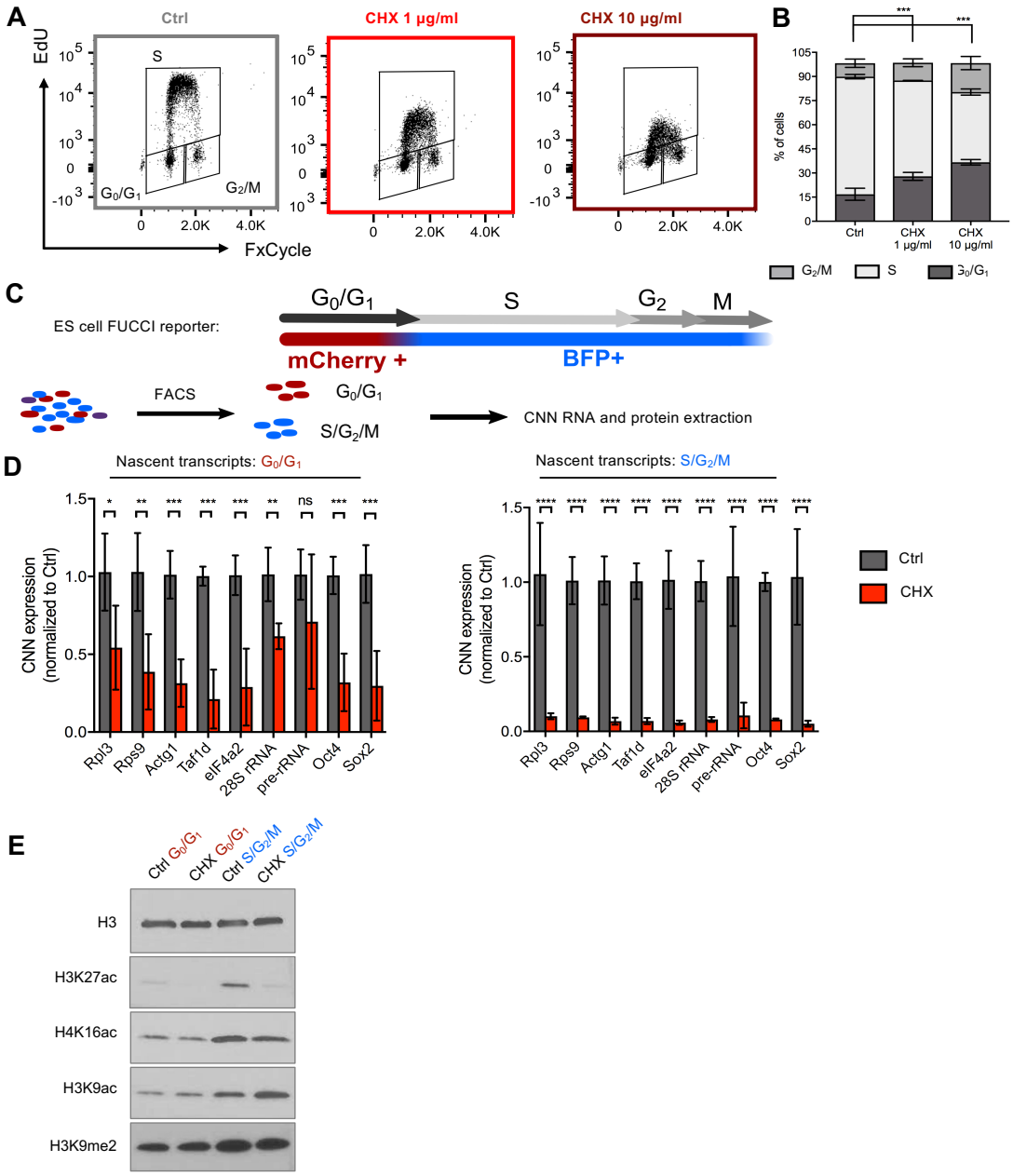

Figure S1.6. Impact of acute inhibition of translation on the cell cycle in ES cells.
(A) Representative flow cytometry plots depicting cell cycle distributions of wild-type ES cells upon DMSO or CHX treatment. (B) Quantification of cell cycle stage distributions in DMSO- or CHX-treated ES cells. Error bars show mean ± SD of 2 biological replicates. Statistical significance was assessed by Chi-square test. **p<0.01. (C) Schematic of the FUCCI cell line used in this study. (D) Nascent RNA capture followed by qRT-PCR in the indicated FACS-isolated populations of DMSO- or CHX-treated (1 µg/ml, 3h) FUCCI. Error bars show mean ± SD of 2 biological replicates. Statistical test performed was two-tailed t-test. *** = p<0.001. (E) Levels of indicated histone modifications in FACS-isolated populations of DMSO- or CHX-treated (1 µg/ml, 3h) FUCCI cells. Blots show 2 biological replicates.

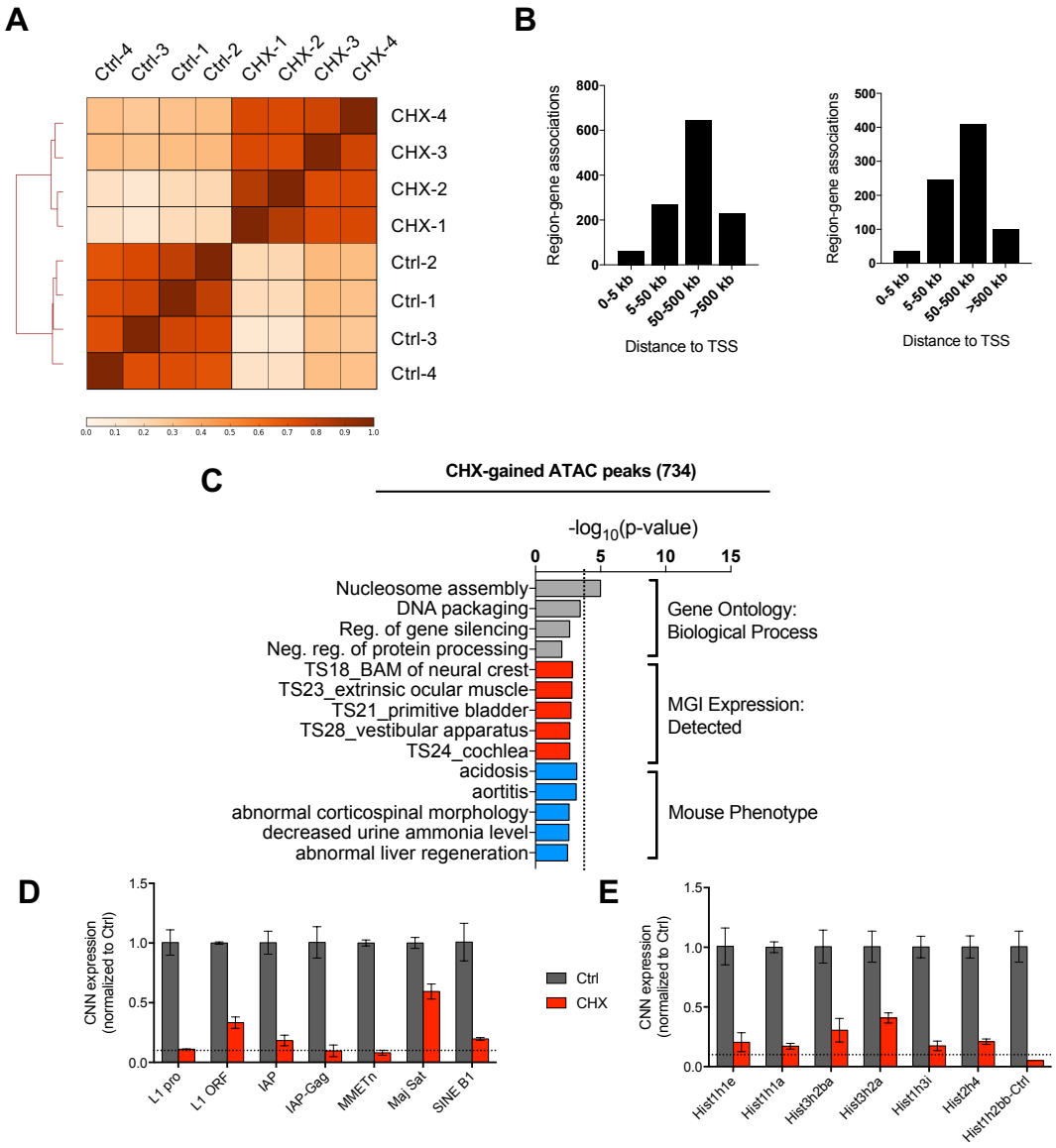

Figure S1.7. Characterization of chromatin accessibility and expression changes upon inhibition of translation in ES cells.
(A) Unsupervised clustering of individual ATAC-seq replicates upon DMSO or CHX treatment for 3 hours. The top 10,787 most variable regions, as determined by Macs14 algorithm, were used for clustering analysis. (B) Distance of CHX-gained or CHX-lost regions from transcription start sites (TSS). (C) Functional annotation of ATAC-seq peaks lost upon CHX treatment for 3 hours. See Table S9 for the full list of terms. (D) Levels of nascent transcription of indicated transposable elements in 3h DMSO- or CHX-treated ES cells, assessed by EU labeling followed by capture and qRT-PCR. Dotted lines represent the average level of downregulation for mRNAs depicted in Figure 4B. (E) Levels of nascent transcription of indicated histone genes in 3h DMSO- or CHX-treated ES cells, assessed by EU labeling followed by capture and qRT-PCR. Dotted lines represent the average level of downregulation for mRNAs depicted in Figure 4B.

Table 1.1 Oligonucleotide sequences

Secondary siRNA screen		
Target	**Fwd sequence**	**Rev sequence**
EGFP	CAAGGACGACGGCAACTACA	TTGTACTCCAGCTTGTGCCC
Ago2	ACCGTGGACACGAAGATCAC	AGGTATGGCTTCCTTCAGCG
Arrb2	GACACCAACCTGGCTTCCA	TAAGGTACCCTCTCCCAGCC
Clp1	GGTCGGAGGTTTCCAGAGGT	GAGAGGCCTCCACCTCAAAT
Cpsf1	TATGTGTACCGCCTGAACCG	GTGCCTGGGTCATACTCCAC
Cpsf2	GTTCCACTAGGGGTTGGGAA	AACCCCAGAGAGGGTGGTTA
ctps2	ACTGCGAGGGGAAGATTGC	TAATCACCGCGCCTCTCTTT
Cxxc1	AAGTCCGAGAAGAAGAAGGAGG	AAGTAGCTTCTTGCCGTGCT
Dnmt3a	CAGCTATTTACAGAGCTTCGGG	CATCGTCGGCTGCTTTGGTA
Eif4g1	GGGACCCTAATGTGGCACC	TTGGGATCCAGCAGGGTAGA
Eif4g2	AGATGACAACTCCGCAGCAA	GCTGAGCATACAGCGAGCTA
Ep400	CAGCAACAGCAGAGTCCTCA	GTGCCTGCAGCTGAGAAGTA
Fbxo3	CTGTCAGTTGGACAGTCGCT	ACCTAAACAAAGATGGTTGGTCTT
Gbx2	CAACTTCGACAAAGCCGAGG	CTTGCCCTTCGGGTCATCTT
Hdac9	ACGCACAGACAGATAGGAGG	AAAGGTGAGATGGGCTCCAG
Igf1	CTGCCTGGGTGTCCAAATGT	TCCGGAAGCAACACTCATCC
Jmjd1c	CGTCATTTGCTGCTCACAGG	TGGTATGGCTGAAAGGCACT
Kat5	GGAGGTGGGGGAGATAATCG	CCCTACGGGCTGACCCATT
Kdm6a	CCATGAACACAGCACAGCAGAA	TAGGACAGGCAGTGTGGACTC
Kmt2b	AGTCCCAGTGGCATCACTATTC	CATGGGGATTCAGAGGTGGC
Lhx9	TCGGTCTTTTCCCTCTCAAGTAGA	GGGCTGAGAGGGGGCATAC
Med14	GACACACATCCTCCGGGACT	ACCATCTACTGCTCATGTACCTT
Med16	GAGGGCCTTCCTGTGAACAA	AGTGAGATGGGCAGTTTCGG
Mtor	ATCCGCTACTGTGTCTTGGC	TTGATTCTCCCAATGCCGCT
Mycbp	CACGCTGACGAAAGTGTTGG	TGCCAATTCTAGGCGAAGCA
Nxf1	CGTGCTTCGCCGGATAAATG	ACCTACGATTCCCCTCACCA
Olfr1188	TCCCCTTGCTACAACTTGCC	TTCCTCCCTGCAGTGCTATG
Olfr958	CCCTCTTCGGTACTCGGTCA	AGGTATCAGCAGACGCCAAT
Papola	GGCGCCATGTTAGGACGAA	TTGTTGTGATCCCTGCGTTG
Polr1b	CGCTACCTCTCCCATTTCCG	CAAGGCTGGAATAGATGCCG
Polr1c	GTTTGGGGTTCGCAATGTCC	GACGAGGATCAGCGAGGATG
Polr2i	GATTACCAGCAGGAAGCCGA	TGGGGCAGTGCAAACATAGT
Polr2m	CTGTCCGTTTCCGGCATTTC	ATGGCAGCTTTCAGTTTGGC
RnaseH2a	ACTCCGATTATGGCTCAGGC	AAAGCACTCGGTCCACTTCT
Rpl10a	GTCAGGCTCAAGTCCACCC	CCAGGATACGTGGGATCTGC

Target	Fwd sequence	Rev sequence
Rpl34	CGAGATCAAACCCGGCTTCC	GACACACTTGGCACACATGG
Rpl35a	GATTGCTGGGGCCTGCT	ACCATACCGCTGTTTCCGTG
Rps28	CAGCCGCTCTATCATCCGAA	CCAGAACCCAGCTGCAAGAT
Rps29	CTGGAGTCACCCACGGAAGT	CAGTCGAATCCATTCAAGGTCG
Srsf1	GTGGAAGCTGGCAGGACTTA	AGGCAGTTTCTCCCTCGTGA
Ssu72	CCACTCTGGGAGCATTCCTT	GTGGAGAGAAAAGGGCCAACA
Trim28	TGCCCTGTCTACATTCGGC	TCGCTCTCCATCTCGAGTCT
Usp7	CCGAGGACATGGAGATGGA	TCACTCAGTCTGCTGAAGCG
Usp9x	TCGCCATATTGACGAGGCTG	CCCTGGTTGTCATTCCCTCC
Yy1	ACAGGCAAGAAACTCCCTCC	TTTGAGCTCTCAACGAACGC
Zfp467	GGCATCCACACAGAACAAGC	GAGCAGGCATCAGGAGACAT
ChIP-qPCR		
Target	**Fwd sequence**	**Rev sequence**
Pax6	CTAATCTGCCGAGCTGAACC	GCAGGCGCTAACTTTCCTTA
Gata4	CCTGGAAAATGTTGGGTAGC	TAGACAAAAGGGTGGGGAGA
Kcna2	TCCGGGACACAGGGATCTAA	CGAATTAAAGGGGCCGGCTG
Rps10	CACAGGGTGAAAACGCCAGA	ACAGCAGATACATGGGTGCC
Rps12	GTGACGCCGAATCTTGAACG	GAGTGTGATCCCAGCTCGTG
Rpl5	GAGTCTGGCCCTGTTTTCAGA	TAAACCGGGCTCAAATGGCA
Rpl3_TSS1	CGCAGATAGAGAGCGACCA	AAAGAGAGACAAGGCGGTTG
Rpl3_TSS2	GCCATCCCTACCAGACTGAC	GAATGGGCTGTTTTGTGCTT
Rpl3 GB	CTGGGGGCACATCTCATAGT	AGATAGGTCCCCTGCCTCTG
Rps9_TSS1	CGTCACTACAAGGCGACGTT	GGAGCCATCACTTGGCTTTA
Rps9_TSS2	GGTTGTGGAACAATCCCATT	CTCGGCTCTCAGAGAAATCC
Rps9 GB	TCAAGCAGCTGGACAGGTAA	TGACTCCAATCTCCCTCCAG
Gapdh	CGCCCTTGAGCTAGGACTG	ATGAAGGGGTCGTTGATGGC
Rps5	TCCTGTCTGTATCAGGGCGG	TCTTCTGAACTCCGTGTCCC
Kcna2	TCCGGGACACAGGGATCTAA	CGAATTAAAGGGGCCGGCTG
rDNA prom	CCTTTGAGGTCCGGTTCTTT	TCCAGGTCCAATAGGAACAGAT
Nanog_TSS	CCTGCAGGTGGGATTAACTGTG	CCTCAAGCCTCCTACCCTACC
Nanog_TSS	CTGGGTGCCTGGGAGAATAG	CAACGGCTCAAGGCGATAGA
Oct4_TSS-F	ATAGCGCTCGCCTCAGTTT	GGGACGGTTTCACCTCTCC
MajSat	GACGACTTGAAAAATGACGAAATC	CATATTCCAGGTCCTTCAGTGTGC

RT-PCR		
Target	**Fwd sequence**	**Rev sequence**
Rpl3	GATGAGTGTAAAAGGCGCTTC	CTTGGTGAAAGCCTTCTTCTT
Rps9	CGTCTCGACCAGGAGCTAAA	CTTGACCCTCCAAACCTCAC
Actg1	CCTGAACCCCAAAGCTAACA	ACATGGCTGGGGTATTGAAG
Taf1d	TGGATGATGATGGTTCACTTTC	GCCTGAGGATTTGTTGCTTC
eIF4a2	GAATTCCGATCAGGGTCAAG	CACTTGTTGCACGTCAATCC
28S rRNA	AAATGTGGCGTACGGAAGAC	CGTGCCGGTATTTAGCCTTA
pre-rRNA	TGTCGTTGTCACACCTGTCC	AAATAAGGTGGCCCTCAACC
Oct4	AGCCGACAACAATGAGAACC	TGGTCTCCAGACTCCACCTC
Sox2	GAACGCCTTCATGGTATGGT	TCTCGGTCTCGGACAAAA
Rpl7	AGCGGATTGCCTTGACAGAT	AACTTGAAGGGCCACAGGAA
Ubb	GCGGTTTGTGCTTTCATCAC	GGCAAAGATCAGCCTCTGCT
Nanog	TCAGATAGGCTGATTTGTTTGCC	CCTTGTCAGCCTCAGGACTTG
Rex1	AATAGGTAGAGCGCATCGCA	CACTGATCCGCAAACACCTG
Fgf5	TGCATCTGCTCTGCTCTAAGAAA	TCATCACATTCCCGAATTAAGCT
Otx2	TGGGCTGAGTCTGACCACTT	GCCCTAGTAAATGTCGTCCTCTC
Pax6	TTATTATCCGAGGGGGTCTGT	CAGGTTGCGAAGAACTCTGTT
Nestin	GGAGAGTCGCTTAGAGGTGC	GGAGAGTCGCTTAGAGGTGC
Gata6	TTAACACTGATTGCTGCAACG	GTTCATCGTAACGTGGCTGA
FoxA2	CATGGGACCTCACCTGAGTC	CATCGAGTTCATGTTGGCGTA
FoxA1	GAAAGGCTAGCCAGCTAGAGG	AGATGCAGCTGAGATTCGTG
T	TCAATGGAGGGGGACAGATCA	CCCCATTGGGAATACCCCG
Hist1h1e	CTTCCGGCTCGAGTTCTCTC	AGCCTTGGTGATGAGTTCGG
Hist1h1a	ACAACAGCCGCATCAAACTG	GTTTCTTAGCAGCCCCGGAT
Hist3h2ba	AACAAGCGCTCGACCATCAC	GAAAAGAGCCTTTGGGTTGGGG
Hist3h2a	GTTTTCGCTAGGTTTCTTTTCTGT	TATTCTAGCACAGCCGCCAG
Hist1h3i	TAGTGTACTGAGATGGCTCGT	CTCGGTCGACTTCTGGTAGC
Hist2h4	CGTGGTGTGCTGAAGGTGTT	GAGCGTACACCACATCCATAG
Hist1h2bb	CCCTCACTGCCTACCAGTTTC	ACCGAATAGCTCTCCTTGCG
L1 prom	ACTGCGGTACATAGGGAAGC	TGTGATCCACTCACCAGAGG
L1 ORF	CACTCCCACCCCACCTAGT	TAACTCTTTAGCAGTGCTCTCCTGT
IAP	TATGCCGAGGGTGGTTCTCTA	TGCGGCAAAACTTTATTGCTT
MMETn	TCAGACTGAAAGCCACATGC	CCGGAGACTAGCCTCAGCTT
MajSat	TGGAATATGGCGAGAAAACTG	AGGTCCTTCAGTGGGCATTT
SINE B1	GTGGCGCACGCCTTTAATC	GACAGGGTTTCTCTGTGTAG
Chd1chromo F	TTATTCCGCTAGCATGCAGCCTGAGGAC	-
EGFP reverse	-	CTCCTCGCCCTTGCTCACCA

Acknowledgments

We thank Hiten Madhani and members of the Santos Lab for critical reading of the manuscript. We thank Thomas Jenuwein for the Hp1α-EGFP vector; Amanda Nolte for virus production; UCSF Institute of Human Genetics for assistance with sequencing and sonication; Shreya Chand for assistance with mass spectrometry; Ava Carter for advice on ATAC-seq libraries; Elphège Nora for sharing FUCCI cells; and Daniel Lim, Elizabeth Hwang, Rebecca Andersen, and Malin Åkerblom for sharing NSPCs. Samples were sequenced at UCSF Institute of Human Genetics Core Facility and Center for Advanced Technology, which is supported by the NIH (5P30CA082103). Flow cytometry data were generated in the UCSF Parnassus Flow Cytometry Core, supported by the Diabetes Research Center (DRC) and the NIH (P30 DK063720). SILAC-MS was performed at the UCSF Mass Spectrometry Facility, supported by the Biomedical Technology Research Centers program of the NIH National Institute of General Medical Sciences (NIH NIGMS 8P41GM103481 and NIH 1S10OD016229) and by Dr. Mariam and Sheldon G. Adelson Medical Research Foundation. Further support comes from NIH grant U01MH105028 and the UCSF Program for Breakthrough Biomedical Research (PBBR) to M.T.M., a Shurl and Kay Curci Foundation Research Grant and a gift from the Dabbiere family to A.D., NIH grant 1F30HD093116 to T.A.M. and NIH grants R01GM113014 and R01OD012204 to M.R.-S.

Author Contributions

A.B.-K. and M.R.-S. conceived of the project. A.B.-K. designed and performed the RNAi screen. A.D. analyzed the RNAi screen output. A.B.-K. and T.A.M. designed, performed and analyzed all other experiments except mass spectrometry. J.A.O.-P. performed mass spectrometry on SILAC samples. M.P. helped with bioinformatics analyses. S.C. and G.K. designed and cloned the shRNA library under the supervision of M.T.M. A.L.B. supervised the SILAC-MS experiment. M.R.-S. supervised the project. A.B.-K., T.A.M. and M.R.-S. wrote the manuscript with feedback from all authors.

References

Afgan, E., Baker, D., van den Beek, M., Blankenberg, D., Bouvier, D., Čech, M., Chilton, J., Clements, D., Coraor, N., Eberhard, C., Grüning, B., Guerler, A., Hillman-Jackson, J., Kuster, Von, G., Rasche, E., Soranzo, N., Turaga, N., Taylor, J., Nekrutenko, A., Goecks, J. (2016). The Galaxy platform for accessible, reproducible and collaborative biomedical analyses: 2016 update. Nucleic Acids Res. 44, W3–W10. doi:10.1093/nar/gkw343

Ahmed, K., Dehghani, H., Rugg-Gunn, P., Fussner, E., Rossant, J., Bazett-Jones, D.P. (2010). Global chromatin architecture reflects pluripotency and lineage commitment in the early mouse embryo. PLoS ONE 5, e10531. doi:10.1371/journal.pone.0010531

Ang, Y.-S., Tsai, S.-Y., Lee, D.-F., Monk, J., Su, J., Ratnakumar, K., Ding, J., Ge, Y., Darr, H., Chang, B., Wang, J., Rendl, M., Bernstein, E., Schaniel, C., Lemischka, I.R. (2011). Wdr5 mediates self-renewal and reprogramming via the embryonic stem cell core transcriptional network. Cell 145, 183–197. doi:10.1016/j.cell.2011.03.003

Bassik, M.C., Lebbink, R.J., Churchman, L.S., Ingolia, N.T., Patena, W., LeProust, E.M., Schuldiner, M., Weissman, J.S., McManus, M.T. (2009). Rapid creation and quantitative monitoring of high coverage shRNA libraries. Nature Methods 6, 443–445. doi:10.1038/nmeth.1330

Belle, A., Tanay, A., Bitincka, L., Shamir, R., O'Shea, E.K. (2006). Quantification of protein half-lives in the budding yeast proteome. Proc. Natl. Acad. Sci. U.S.A. 103, 13004–13009. doi:10.1073/pnas.0605420103

Blanco, S., Bandiera, R., Popis, M., Hussain, S., Lombard, P., Aleksic, J., Sajini, A., Tanna, H., Cortés-Garrido, R., Gkatza, N., Dietmann, S., Frye, M. (2016). Stem cell function and stress response are controlled by protein synthesis. Nature 534, 335–340. doi:10.1038/nature18282

Brookes, E., de Santiago, I., Hebenstreit, D., Morris, K.J., Carroll, T., Xie, S.Q., Stock, J.K., Heidemann, M., Eick, D., Nozaki, N., Kimura, H., Ragoussis, J., Teichmann, S.A., Pombo, A.

(2012). Polycomb associates genome-wide with a specific RNA polymerase II variant, and regulates metabolic genes in ESCs. Cell Stem Cell 10, 157–170. doi:10.1016/j.stem.2011.12.017

Buckley, S.M., Aranda-Orgilles, B., Strikoudis, A., Apostolou, E., Loizou, E., Moran-Crusio, K., Farnsworth, C.L., Koller, A.A., Dasgupta, R., Silva, J.C., Stadtfeld, M., Hochedlinger, K., Chen, E.I., Aifantis, I. (2012). Regulation of pluripotency and cellular reprogramming by the ubiquitin-proteasome system. Cell Stem Cell 11, 783–798. doi:10.1016/j.stem.2012.09.011

Buenrostro, J.D., Wu, B., Chang, H.Y., Greenleaf, W.J. (2015). ATAC-seq: A Method for Assaying Chromatin Accessibility Genome-Wide. Curr Protoc Mol Biol 109, 21.29.1–21.29.9. doi:10.1002/0471142727.mb2129s109

Bulut-Karslioglu, A., Biechele, S., Jin, H., Macrae, T.A., Hejna, M., Gertsenstein, M., Song, J.S., Ramalho-Santos, M. (2016). Inhibition of mTOR induces a paused pluripotent state. Nature 540, 119–123. doi:10.1038/nature20578

Bulut-Karslioglu, A., La Rosa-Velázquez, De, I.A., Ramirez, F., Barenboim, M., Onishi-Seebacher, M., Arand, J., Galán, C., Winter, G.E., Engist, B., Gerle, B., O'Sullivan, R.J., Martens, J.H.A., Walter, J., Manke, T., Lachner, M., Jenuwein, T. (2014). Suv39h-Dependent H3K9me3 Marks Intact Retrotransposons and Silences LINE Elements in Mouse Embryonic Stem Cells. Molecular Cell 55, 277–290. doi:10.1016/j.molcel.2014.05.029

Calo, E., Wysocka, J. (2013). Modification of enhancer chromatin: what, how, and why? Molecular Cell 49, 825–837. doi:10.1016/j.molcel.2013.01.038

Carpenter, A.E., Jones, T.R., Lamprecht, M.R., Clarke, C., Kang, I.H., Friman, O., Guertin, D.A., Chang, J.H., Lindquist, R.A., Moffat, J., Golland, P., Sabatini, D.M. (2006). CellProfiler: image analysis software for identifying and quantifying cell phenotypes. Genome Biol. 7, R100. doi:10.1186/gb-2006-7-10-r100

Chen, Z.Y., Wang, X., Zhou, Y., Offner, G., Tseng, C.-C. (2005). Destabilization of Krüppel-like factor 4 protein in response to serum stimulation involves the ubiquitin-proteasome pathway.

Cancer Res. 65, 10394–10400. doi:10.1158/0008-5472.CAN-05-2059

Crump, N.T., Hazzalin, C.A., Bowers, E.M., Alani, R.M., Cole, P.A., Mahadevan, L.C. (2011). Dynamic acetylation of all lysine-4 trimethylated histone H3 is evolutionarily conserved and mediated by p300/CBP. Proc. Natl. Acad. Sci. U.S.A. 108, 7814–7819. doi:10.1073/pnas.1100099108

Denissov, S., Hofemeister, H., Marks, H., Kranz, A., Ciotta, G., Singh, S., Anastassiadis, K., Stunnenberg, H.G., Stewart, A.F. (2014). Mll2 is required for H3K4 trimethylation on bivalent promoters in embryonic stem cells, whereas Mll1 is redundant. Development 141, 526–537. doi:10.1242/dev.102681

Diaz, A.A., Qin, H., Ramalho-Santos, M., Song, J.S. (2015). HiTSelect: a comprehensive tool for high-complexity-pooled screen analysis. Nucleic Acids Res. 43, e16–e16. doi:10.1093/nar/gku1197

Efroni, S., Duttagupta, R., Cheng, J., Dehghani, H., Hoeppner, D.J., Dash, C., Bazett-Jones, D.P., Le Grice, S., McKay, R.D.G., Buetow, K.H., Gingeras, T.R., Misteli, T., Meshorer, E. (2008). Global Transcription in Pluripotent Embryonic Stem Cells. Cell Stem Cell 2, 437–447. doi:10.1016/j.stem.2008.03.021

ENCODE Project Consortium (2012). An integrated encyclopedia of DNA elements in the human genome. Nature 489, 57–74. doi:10.1038/nature11247

Fazzio, T.G., Huff, J.T., Panning, B. (2008). An RNAi screen of chromatin proteins identifies Tip60-p400 as a regulator of embryonic stem cell identity. Cell 134, 162–174. doi:10.1016/j.cell.2008.05.031

Flanagan, J.F., Mi, L.-Z., Chruszcz, M., Cymborowski, M., Clines, K.L., Kim, Y., Minor, W., Rastinejad, F., Khorasanizadeh, S. (2005). Double chromodomains cooperate to recognize the methylated histone H3 tail. Nature 438, 1181–1185. doi:10.1038/nature04290

Frerichs, K.U., Smith, C.B., Brenner, M., DeGracia, D.J., Krause, G.S., Marrone, L., Dever, T.E., Hallenbeck, J.M. (1998). Suppression of protein synthesis in brain during hibernation involves

inhibition of protein initiation and elongation. Proc. Natl. Acad. Sci. U.S.A. 95, 14511–14516.

Gaspar-Maia, A., Alajem, A., Meshorer, E., Ramalho-Santos, M. (2011). Open chromatin in pluripotency and reprogramming. Nat. Rev. Mol. Cell Biol. 12, 36–47. doi:10.1038/nrm3036

Gaspar-Maia, A., Alajem, A., Polesso, F., Sridharan, R., Mason, M.J., Heidersbach, A., Ramalho-Santos, J., McManus, M.T., Plath, K., Meshorer, E., Ramalho-Santos, M. (2009). Chd1 regulates open chromatin and pluripotency of embryonic stem cells. Nature 460, 863–868. doi:10.1038/nature08212

Goldberg, A.D., Banaszynski, L.A., Noh, K.-M., Lewis, P.W., Elsaesser, S.J., Stadler, S., Dewell, S., Law, M., Guo, X., Li, X., Wen, D., Chapgier, A., DeKelver, R.C., Miller, J.C., Lee, Y.-L., Boydston, E.A., Holmes, M.C., Gregory, P.D., Greally, J.M., Rafii, S., Yang, C., Scambler, P.J., Garrick, D., Gibbons, R.J., Higgs, D.R., Cristea, I.M., Urnov, F.D., Zheng, D., Allis, C.D. (2010). Distinct factors control histone variant H3.3 localization at specific genomic regions. Cell 140, 678–691. doi:10.1016/j.cell.2010.01.003

Guan, S., Price, J.C., Prusiner, S.B., Ghaemmaghami, S., Burlingame, A.L. (2011). A data processing pipeline for mammalian proteome dynamics studies using stable isotope metabolic labeling. Mol. Cell Proteomics 10, M111.010728. doi:10.1074/mcp.M111.010728

Guzman-Ayala, M., Sachs, M., Koh, F.M., Onodera, C., Bulut-Karslioglu, A., Lin, C.J., Wong, P., Nitta, R., Song, J.S., Ramalho-Santos, M. (2014). Chd1 is essential for the high transcriptional output and rapid growth of the mouse epiblast. Development 142, 118–127. doi:10.1242/dev.114843

Heinz, S., Benner, C., Spann, N., Bertolino, E., Lin, Y.C., Laslo, P., Cheng, J.X., Murre, C., Singh, H., Glass, C.K. (2010). Simple combinations of lineage-determining transcription factors prime cis-regulatory elements required for macrophage and B cell identities. Molecular Cell 38, 576–589. doi:10.1016/j.molcel.2010.05.004

Hooper, M., Hardy, K., Handyside, A., Hunter, S., Monk, M. (1987). HPRT-deficient (Lesch-Nyhan) mouse embryos derived from germline colonization by cultured cells. Nature 326,

292–295. doi:10.1038/326292a0

Huber, W., Carey, V.J., Gentleman, R., Anders, S., Carlson, M., Carvalho, B.S., Bravo, H.C., Davis, S., Gatto, L., Girke, T., Gottardo, R., Hahne, F., Hansen, K.D., Irizarry, R.A., Lawrence, M., Love, M.I., MacDonald, J., Obenchain, V., Oleś, A.K., Pagès, H., Reyes, A., Shannon, P., Smyth, G.K., Tenenbaum, D., Waldron, L., Morgan, M. (2015). Orchestrating high-throughput genomic analysis with Bioconductor. Nature Methods 12, 115–121. doi:10.1038/nmeth.3252

Hudlebusch, H.R., Skotte, J., Santoni-Rugiu, E., Zimling, Z.G., Lees, M.J., Simon, R., Sauter, G., Rota, R., De Ioris, M.A., Quarto, M., Johansen, J.V., Jørgensen, M., Rechnitzer, C., Maroun, L.L., Schrøder, H., Petersen, B.L., Helin, K. (2011). MMSET is highly expressed and associated with aggressiveness in neuroblastoma. Cancer Res. 71, 4226–4235. doi:10.1158/0008-5472.CAN-10-3810

Jin, C., Zang, C., Wei, G., Cui, K., Peng, W., Zhao, K., Felsenfeld, G. (2009). H3.3/H2A.Z double variant-containing nucleosomes mark “nucleosome-free regions” of active promoters and other regulatory regions. Nat. Genet. 41, 941–945. doi:10.1038/ng.409

Jolly, L.A., Taylor, V., Wood, S.A. (2009). USP9X enhances the polarity and self-renewal of embryonic stem cell-derived neural progenitors. Mol. Biol. Cell 20, 2015–2029. doi:10.1091/mbc.E08-06-0596

Karolchik, D., Hinrichs, A.S., Furey, T.S., Roskin, K.M., Sugnet, C.W., Haussler, D., Kent, W.J. (2004). The UCSC Table Browser data retrieval tool. Nucleic Acids Res. 32, D493–6. doi:10.1093/nar/gkh103

Koh, F.M., Lizama, C.O., Wong, P., Hawkins, J.S., Zovein, A.C., Ramalho-Santos, M. (2015). Emergence of hematopoietic stem and progenitor cells involves a Chd1-dependent increase in total nascent transcription. Proc. Natl. Acad. Sci. U.S.A. 112, E1734–43. doi:10.1073/pnas.1424850112

Ku, M., Jaffe, J.D., Koche, R.P., Rheinbay, E., Endoh, M., Koseki, H., Carr, S.A., Bernstein, B.E. (2012). H2A.Z landscapes and dual modifications in pluripotent and multipotent stem cells

underlie complex genome regulatory functions. Genome Biol. 13, R85. doi:10.1186/gb-2012-13-10-r85

Langmead, B., Salzberg, S.L. (2012). Fast gapped-read alignment with Bowtie 2. Nature Methods 9, 357–359. doi:10.1038/nmeth.1923

Laplante, M., Sabatini, D.M. (2012). mTOR signaling in growth control and disease. Cell 149, 274–293. doi:10.1016/j.cell.2012.03.017

Lee, J.-H., Hart, S.R.L., Skalnik, D.G. (2004). Histone deacetylase activity is required for embryonic stem cell differentiation. Genesis 38, 32–38. doi:10.1002/gene.10250

Li, B., Jackson, J., Simon, M.D., Fleharty, B., Gogol, M., Seidel, C., Workman, J.L., Shilatifard, A. (2009). Histone H3 lysine 36 dimethylation (H3K36me2) is sufficient to recruit the Rpd3s histone deacetylase complex and to repress spurious transcription. J. Biol. Chem. 284, 7970–7976. doi:10.1074/jbc.M808220200

Li, H., Handsaker, B., Wysoker, A., Fennell, T., Ruan, J., Homer, N., Marth, G., Abecasis, G., Durbin, R., 1000 Genome Project Data Processing Subgroup (2009). The Sequence Alignment/Map format and SAMtools. Bioinformatics 25, 2078–2079. doi:10.1093/bioinformatics/btp352

Li, X., Li, L., Pandey, R., Byun, J.S., Gardner, K., Qin, Z., Dou, Y. (2012). The histone acetyltransferase MOF is a key regulator of the embryonic stem cell core transcriptional network. Cell Stem Cell 11, 163–178. doi:10.1016/j.stem.2012.04.023

Liao, Y., Smyth, G.K., Shi, W. (2013). The Subread aligner: fast, accurate and scalable read mapping by seed-and-vote. Nucleic Acids Res. 41, e108–e108. doi:10.1093/nar/gkt214

McKnight, J.N., Boerma, J.W., Breeden, L.L., Tsukiyama, T. (2015). Global Promoter Targeting of a Conserved Lysine Deacetylase for Transcriptional Shutoff during Quiescence Entry. Molecular Cell 59, 732–743. doi:10.1016/j.molcel.2015.07.014

McLean, C.Y., Bristor, D., Hiller, M., Clarke, S.L., Schaar, B.T., Lowe, C.B., Wenger, A.M., Bejerano, G. (2010). GREAT improves functional interpretation of cis-regulatory regions. Nat.

Biotechnol. 28, 495–501. doi:10.1038/nbt.1630

Melcer, S., Hezroni, H., Rand, E., Nissim-Rafinia, M., Skoultchi, A., Stewart, C.L., Bustin, M., Meshorer, E. (2012). Histone modifications and lamin A regulate chromatin protein dynamics in early embryonic stem cell differentiation. Nat Comms 3, 910. doi:10.1038/ncomms1915

Meshorer, E., Yellajoshula, D., George, E., Scambler, P.J., Brown, D.T., Misteli, T. (2006). Hyperdynamic plasticity of chromatin proteins in pluripotent embryonic stem cells. Developmental Cell 10, 105–116. doi:10.1016/j.devcel.2005.10.017

Méndez, J., Stillman, B. (2000). Chromatin association of human origin recognition complex, cdc6, and minichromosome maintenance proteins during the cell cycle: assembly of prereplication complexes in late mitosis. Mol. Cell. Biol. 20, 8602–8612.

Mishima, Y., Miyagi, S., Saraya, A., Negishi, M., Endoh, M., Endo, T.A., Toyoda, T., Shinga, J., Katsumoto, T., Chiba, T., Yamaguchi, N., Kitabayashi, I., Koseki, H., Iwama, A. (2011). The Hbo1-Brd1/Brpf2 complex is responsible for global acetylation of H3K14 and required for fetal liver erythropoiesis. Blood 118, 2443–2453. doi:10.1182/blood-2011-01-331892

Moussaieff, A., Rouleau, M., Kitsberg, D., Cohen, M., Levy, G., Barasch, D., Nemirovski, A., Shen-Orr, S., Laevsky, I., Amit, M., Bomze, D., Elena-Herrmann, B., Scherf, T., Nissim-Rafinia, M., Kempa, S., Itskovitz-Eldor, J., Meshorer, E., Aberdam, D., Nahmias, Y. (2015). Glycolysis-mediated changes in acetyl-CoA and histone acetylation control the early differentiation of embryonic stem cells. Cell Metabolism 21, 392–402. doi:10.1016/j.cmet.2015.02.002

Nagarajan, P., Ge, Z., Sirbu, B., Doughty, C., Agudelo Garcia, P.A., Schlederer, M., Annunziato, A.T., Cortez, D., Kenner, L., Parthun, M.R. (2013). Histone acetyl transferase 1 is essential for mammalian development, genome stability, and the processing of newly synthesized histones H3 and H4. PLoS Genet. 9, e1003518. doi:10.1371/journal.pgen.1003518

Nora, E.P., Goloborodko, A., Valton, A.-L., Gibcus, J.H., Uebersohn, A., Abdennur, N., Dekker, J., Mirny, L.A., Bruneau, B.G. (2017). Targeted Degradation of CTCF Decouples Local Insulation of Chromosome Domains from Genomic Compartmentalization. Cell 169, 930–

944.e22. doi:10.1016/j.cell.2017.05.004

Olsnes, S. (1972). Toxic proteins inhibiting protein synthesis. Naturwissenschaften 59, 497–502.

Orlando, D.A., Chen, M.W., Brown, V.E., Solanki, S., Choi, Y.J., Olson, E.R., Fritz, C.C., Bradner, J.E., Guenther, M.G. (2014). Quantitative ChIP-Seq normalization reveals global modulation of the epigenome. Cell Rep 9, 1163–1170. doi:10.1016/j.celrep.2014.10.018

Pantaleon, M., Kanai-Azuma, M., Mattick, J.S., Kaibuchi, K., Kaye, P.L., Wood, S.A. (2001). FAM deubiquitylating enzyme is essential for preimplantation mouse embryo development. Mech. Dev. 109, 151–160.

Percharde, M., Bulut-Karslioglu, A., Ramalho-Santos, M. (2017a). Hypertranscription in Development, Stem Cells, and Regeneration. Developmental Cell 40, 9–21. doi:10.1016/j.devcel.2016.11.010

Percharde, M., Wong, P., Ramalho-Santos, M. (2017b). Global Hypertranscription in the Mouse Embryonic Germline. Cell Rep 19, 1987–1996. doi:10.1016/j.celrep.2017.05.036

Pungaliya, P., Kulkarni, D., Park, H.-J., Marshall, H., Zheng, H., Lackland, H., Saleem, A., Rubin, E.H. (2007). TOPORS functions as a SUMO-1 E3 ligase for chromatin-modifying proteins. J. Proteome Res. 6, 3918–3923. doi:10.1021/pr0703674

Qin, H., Diaz, A., Blouin, L., Lebbink, R.J., Patena, W., Tanbun, P., LeProust, E.M., McManus, M.T., Song, J.S., Ramalho-Santos, M. (2014). Systematic identification of barriers to human iPSC generation. Cell 158, 449–461. doi:10.1016/j.cell.2014.05.040

Ramirez, F., Ryan, D.P., Grüning, B., Bhardwaj, V., Kilpert, F., Richter, A.S., Heyne, S., Dündar, F., Manke, T. (2016). deepTools2: a next generation web server for deep-sequencing data analysis. Nucleic Acids Res. 44, W160–5. doi:10.1093/nar/gkw257

Sampath, P., Pritchard, D.K., Pabon, L., Reinecke, H., Schwartz, S.M., Morris, D.R., Murry, C.E. (2008). A Hierarchical Network Controls Protein Translation during Murine Embryonic Stem Cell Self-Renewal and Differentiation. Cell Stem Cell 2, 448–460. doi:10.1016/j.stem.2008.03.013

Schwanhäusser, B., Busse, D., Li, N., Dittmar, G., Schuchhardt, J., Wolf, J., Chen, W., Selbach, M. (2011). Global quantification of mammalian gene expression control. Nature 473, 337–342. doi:10.1038/nature10098

Scognamiglio, R., Cabezas-Wallscheid, N., Thier, M.C., Altamura, S., Reyes, A., Prendergast, Á.M., Baumgärtner, D., Carnevalli, L.S., Atzberger, A., Haas, S., Paleske, von, L., Boroviak, T., Wörsdörfer, P., Essers, M.A.G., Kloz, U., Eisenman, R.N., Edenhofer, F., Bertone, P., Huber, W., van der Hoeven, F., Smith, A., Trumpp, A. (2016). Myc Depletion Induces a Pluripotent Dormant State Mimicking Diapause. Cell 164, 668–680. doi:10.1016/j.cell.2015.12.033

Sheikh, B.N., Bechtel-Walz, W., Lucci, J., Karpiuk, O., Hild, I., Hartleben, B., Vornweg, J., Helmstädter, M., Sahyoun, A.H., Bhardwaj, V., Stehle, T., Diehl, S., Kretz, O., Voss, A.K., Thomas, T., Manke, T., Huber, T.B., Akhtar, A. (2016). MOF maintains transcriptional programs regulating cellular stress response. Oncogene 35, 2698–2710. doi:10.1038/onc.2015.335

Signer, R.A.J., Magee, J.A., Salic, A., Morrison, S.J. (2014). Haematopoietic stem cells require a highly regulated protein synthesis rate. Nature 509, 49–54. doi:10.1038/nature13035

Smith, A. (2017). Formative pluripotency: the executive phase in a developmental continuum. Development 144, 365–373. doi:10.1242/dev.142679

Tsang, C.K., Bertram, P.G., Ai, W., Drenan, R., Zheng, X.F.S. (2003). Chromatin-mediated regulation of nucleolar structure and RNA Pol I localization by TOR. EMBO J. 22, 6045–6056. doi:10.1093/emboj/cdg578

Unnikrishnan, A., Gafken, P.R., Tsukiyama, T. (2010). Dynamic changes in histone acetylation regulate origins of DNA replication. Nat Struct Mol Biol 17, 430–437. doi:10.1038/nsmb.1780

Valouev, A., Johnson, S.M., Boyd, S.D., Smith, C.L., Fire, A.Z., Sidow, A. (2011). Determinants of nucleosome organization in primary human cells. Nature 474, 516–520. doi:10.1038/nature10002

Vilchez, D., Boyer, L., Morantte, I., Lutz, M., Merkwirth, C., Joyce, D., Spencer, B., Page, L., Masliah, E., Berggren, W.T., Gage, F.H., Dillin, A. (2012). Increased proteasome activity in human embryonic stem cells is regulated by PSMD11. Nature 489, 304–308. doi:10.1038/nature11468

Wan, M., Liang, J., Xiong, Y., Shi, F., Zhang, Y., Lu, W., He, Q., Yang, D., Chen, R., Liu, D., Barton, M., Songyang, Z. (2013). The trithorax group protein Ash2l is essential for pluripotency and maintaining open chromatin in embryonic stem cells. J. Biol. Chem. 288, 5039–5048. doi:10.1074/jbc.M112.424515

Wang, L., Du, Y., Ward, J.M., Shimbo, T., Lackford, B., Zheng, X., Miao, Y.-L., Zhou, B., Han, L., Fargo, D.C., Jothi, R., Williams, C.J., Wade, P.A., Hu, G. (2014). INO80 facilitates pluripotency gene activation in embryonic stem cell self-renewal, reprogramming, and blastocyst development. Cell Stem Cell 14, 575–591. doi:10.1016/j.stem.2014.02.013

Ying, Q.-L., Wray, J., Nichols, J., Batlle-Morera, L., Doble, B., Woodgett, J., Cohen, P., Smith, A. (2008). The ground state of embryonic stem cell self-renewal. Nature 453, 519–523. doi:10.1038/nature06968

Zhang, Q., Shalaby, N.A., Buszczak, M. (2014). Changes in rRNA transcription influence proliferation and cell fate within a stem cell lineage. Science 343, 298–301. doi:10.1126/science.1246384

Zhang, Y., Liu, T., Meyer, C.A., Eeckhoute, J., Johnson, D.S., Bernstein, B.E., Nusbaum, C., Myers, R.M., Brown, M., Li, W., Liu, X.S. (2008). Model-based analysis of ChIP-Seq (MACS). Genome Biol. 9, R137. doi:10.1186/gb-2008-9-9-r137

Materials and Methods

EXPERIMENTAL MODEL AND SUBJECT DETAILS

Mice

Swiss Webster females (6- to 12-week-old) and males (6 week- to 6 month-old) were used. Animals were maintained on 12 h light/dark cycle and provided with food and water *ad libitum* in individually ventilated units (Lab Products at UCSF) in the specific-pathogen free facilities at UCSF. All procedures involving animals were performed in compliance with the protocol approved by the IACUC at UCSF, as part of an AAALAC-accredited care and use program (protocol AN091331-03).

Mouse embryonic stem cells

Wild-type E14 male ESCs (source: Bill Skarnes, Sanger Institute) were used for all reporter-free experiments. ES-FBS cells were cultured in DMEM GlutaMAX with Na Pyruvate, 15% FBS, 0.1 mM Non-essential amino acids, 50 U/ml Penicillin/Streptomycin, 0.1 mM EmbryoMax 2-Mercaptoethanol and 2000 U/ml ESGRO supplement. For the experiments in 2i medium, E14 ESCs initially grown in serum were passaged at least 4 times in 2i medium before use. 2i medium was composed of DMEM/F-12, Neurobasal medium, 1x N2/B27 supplements, 1 μM PD0325901, 3 μM CHIR99021, 50 μM Ascorbic acid and 2000 U/ml ESGRO supplement. Cells were cultured in 0.5% FBS for serum starvation experiments. Cells were not authenticated and tested negative for mycoplasma contamination.

Chd1chr-EGFP reporter cell line

A single PCR fragment containing the double chromodomains of Chd1 (amino acids 262 to 460) was isolated and cloned in frame into the pCAGGS-EGFP-IRES-Puro plasmid. Stable Chd1chr-

EGFP expressing ESC lines were generated by transfecting 4 µg *PvuI*-linearized vector into 10^6 wild-type E14 ESCs, followed by Puromycin selection.

Mouse embryonic fibroblasts

Primary MEFs were derived from CD1 E12.5 mouse embryos and used at passage 3-6. MEFs were cultured in DMEM GlutaMAX with Na Pyruvate, 10% FBS, 0.1 mM Non-essential amino acids, 50 U/ml Penicillin/Streptomycin.

Neural stem/progenitor cells (NSPCs)

Early-passage NSPCs (p5-p10), originally derived from mouse E12.5 cortex (Hudlebusch et al., 2011), were cultured on poly-D-lysine and laminin coated plates in medium containing: 50% DMEM/F12, 50% Neurobasal, 1x N2 and B27 supplements, 0.1 mM Non-essential amino acids, 50 U/ml Penicillin/Streptomycin, 0.11 mg/ml Na Pyruvate, 5 mM HEPES, 1x GlutaMAX, 0.1 mg/ml Fraction V BSA, 2 µM EmbryoMax 2-Mercaptoethanol, 20 ng/ml bFGF, 10 ng/ml EGF and 2 µg/ml Heparin sodium salt.

METHOD DETAILS

Embryo culture

Wild-type mice were mated, blastocysts were collected at E3.5 after detection of the copulatory plug by flushing uteri of pregnant females using M2 medium (Zenith Biotech) supplemented with 2% BSA (Sigma). Subsequent embryo culture was performed in 3.5-cm plates under light mineral oil (Zenith Biotech) in 5% O_2, 5% CO_2 at 37°C in $KSOM^{AA}$ Evolve medium (Zenith Biotech) with 2% BSA until E4.5.

Wdr5 knock-down

Wdr5 shRNAs were designed based on the siRNA sequences from Ang et al (Ang et al., 2011). Control shRNA includes non-targeting sequence (Qin et al., 2014). shRNAs were cloned into the pSicoR-mCherry plasmid and constructs was packaged into lentivirus. Chd1chr-EGFP and Hp1α-EGFP ESCs were transduced with the lentiviral vectors. mCherry-positive cells with integrated shRNAs were sorted and knock-down was confirmed by qRT-PCR 72h post-transduction. EGFP fluorescence levels were analyzed on day 3 on an Avalon S3 Cell Sorter (Propel Labs).

Retinoic-acid mediated differentiation

Chd1chr-EGFP and Hp1α-EGFP ESCs were used. LIF was withdrawn from ES-FBS medium and retinoic acid was added at a final concentration of 5 μM. EGFP fluorescence levels were analyzed on day 3 on an Avalon S3 Cell Sorter (Propel Labs). For nascent transcription and chromatin analyses, LIF was withdrawn from ES-FBS medium for 1 day and 5 μM retinoic acid was added for 2 days before 3h DMSO or CHX treatment.

Western blot analysis

For histone analysis, histones were acid extracted and TCA-precipitated as follows: $7x10^6$ cells were washed in ice-cold PBS with 5 mM Na Butyrate. Cells were lysed in Triton Extraction Buffer (PBS, 0.5% Triton X-100, 1x Protease Inhibitor Cocktail, 1 mM PMSF, 5 mM NaVO4 and 5 mM NaF) for 10 minutes and centrifuged. The pellet was resuspended in 0.2N HCl and histones were extracted overnight. Extracted histones were precipitated with TCA, washed with ice-cold acetone and resuspended in water. For analysis of cellular fractions, cytoplasmic, nucleoplasmic and chromatin fractions were isolated as previously described (Méndez and Stillman, 2000). Cells were initially resuspended in Buffer A (10 mM HEPES pH7.9, 10 mM KCl, 1.5 mM $MgCl_2$, 0.34 M sucrose, 10% glycerol, 1 mM DTT, 0.1% Triton X-100, 1x Halt protease inhibitor cocktail (Thermo Fisher Scientific), 1 mM PMSF, 5 mM NaF and 1 mM $NaVO_4$). Cells were incubated for 5 minutes on ice, then spun down at 1,300 g for 5 minutes at 4°C. Cytoplasmic fraction (supernatant) was transferred to new tubes. Pellets (nuclei) were resuspended in buffer B (3 mM EDTA, 0.2 mM EGTA, 1 mM DTT, 1x Halt protease inhibitor cocktail, 1 mM PMSF, 5 mM NaF and 1 mM $NaVO_4$). Nuclei were incubated for 5 minutes on ice, then spun down at 1,700 g for 5 minutes at 4°C. Nucleoplasmic fraction (supernatant) was transferred to new tubes. Pellets (insoluble chromatin) were resuspended in 1x Laemmli Buffer with 5% β-mercaptoethanol and sonicated using the Bioruptor for 5 minutes with settings high, 30 seconds on, 30 seconds off. Extracts were loaded into 4-15% Mini-Protean TGX SDS Page gels (Bio-Rad). Proteins were transferred to PVDF membranes. Membranes were blocked in 5% milk/PBS-T buffer for 30 min and incubated either overnight at 4°C or for 1 hour at room temperature with the following antibodies: H4K16ac (RRID:AB_310525), H3K4me3 (RRID:AB_1163444), H3K9me2 (RRID:AB_449854), Hp1α (RRID:AB_11213599), Gapdh (RRID:AB_2107445), H3K27ac, (RRID:AB_2716381) H3K9ac (RRID:AB_2716379), H3 (RRID:AB_302613), H4 (RRID:AB_305837), H3K36me2 (RRID:AB_1280939), β-actin (RRID:AB_2305186), RNA Pol II (RRID:AB_306327), RNA Pol II

S2P (RRID:AB_304749), G9a (RRID:AB_2532211), Ezh2 (RRID:AB_10694683), Topors (RRID:AB_10852342), Chd1 (RRID:AB_11179073), Btf3 (RRID:AB_2067525), Brd1 (RRID:AB_2618449), Tip60 (RRID:AB_1950610), EGFP (RRID:AB_221569) and anti-rabbit/mouse/goat secondary antibodies (RRID:AB_2307391; RRID:AB_2338504; RRID:AB_656964). Membranes were incubated with ECL or ECL Plus reagents and exposed to X-ray films (Thermo Fisher Scientific). Quantification of WB bands were carried out using the Gimp image analysis software.

For analysis of FUCCI ESCs, cells were plated overnight before 3h treatment with CHX at 1 µg/ml or DMSO. Cells were collected by trypsinization and sorted on a FACS AriaII (BD Biosciences) into mCherry+ (G_0/G_1) and BFP+ ($S/G_2/M$) cell fractions. $4x10^5$ cells of each fraction were sorted for histone extraction and western blotting as above.

Genome-wide shRNA screen

The ultracomplex EXPANDed shRNA library targeting the mouse genome was designed similarly to human shRNA libraries described before (Bassik et al., 2009). In brief, the library contains approximately 30 independent shRNAs per gene for all mouse protein-coding genes, for a total of ~600,000 shRNAs, hence the term “ultracomplex.” The full list of shRNA sequences present in the library is available upon request. Pooled sequences coding for the shRNAs were cloned downstream of a U6 promoter in a modified pSicoR lentiviral vector containing a EF1a-Puro-T2A-mCherry cassette. All vectors were pooled to generate one lentiviral library representing the 600,000 shRNAs. The entire pooled library was then used to generate lentiviruses at the UCSF ViraCore. $6.6x10^7$ Chd1chr-EGFP ESCs were infected at an MOI (multiplicity of infection) ≤ 1 with the shRNA library, such that each shRNA is targeted to 100 cells (100x coverage). Cells were plated on thirteen 15 cm cell culture plates at a density of $5x10^6$ per 15 cm plate. Culture medium

was changed daily; cells were harvested for analysis on day 3. mCherry-positive cells were sorted into GFP^{low} and GFP^{high} populations on an Avalon S3 Cell Sorter (Propel Labs). Integrated shRNAs were isolated by PCR using oligos which contained sequencing adapters and barcodes. Screen results were analyzed as described before (Diaz et al., 2015).

Single-gene knock down experiments

siRNAs were ordered as pools of 4 sequences from GE Dharmacon's Cherry-Pick libraries. Chd1chr-EGFP ESCs were transfected with the siRNAs in 96-well plates. qRT-PCR and flow cytometry analyses were performed on day 2 or 3 as indicated. Fluorescence was analyzed on a BD Dual Fortessa.

Inhibitor treatments

Cells were incubated for indicated durations and concentrations with the following inhibitors: INK128 (Medchem), 10058-F4 (Sigma), Cycloheximide (Amresco), α-amanitin (Sigma), CX-5461 (Selleckchem), MG-132 (Selleckchem), Homoharringtonine (Sigma), and AZD8055 (Selleckchem). Control cells were treated with DMSO. Inhibitors were withdrawn and cells were washed just prior to downstream analyses. For all CHX release experiments, cells were treated with DMSO or CHX for indicated durations. Cells were washed with PBS before addition of fresh medium and harvesting at indicated time points. For all embryo experiments, inhibitors were added to E4.5 blastocysts for the last 3 hours of culture.

Global nascent transcription and translation analysis

For measurements of global transcriptional and translational output, wild-type E14 cells, RA-differentiated ESCs, MEFs, or NSPCs were plated and cultured overnight in their respective medium. E3.5 blastocysts were cultured *ex vivo* to E4.5 as described above. 5-ethynyl uridine (EU) was added at a final concentration of 1 mM or L-homopropargylglycine (HPG) at a final

concentration of 25 μM, both for the last 45 minutes of 3h treatments. During nascent translation experiments, normal media were replaced with media containing Met-/Cys-free DMEM 45 minutes prior to the addition of HPG. Cells were trypsinized and processed according to the instructions of the Click-iT RNA (or HPG) Alexa Fluor 488 or 594 HCS Assay kits. For each experiment, cells without EU or HPG added were processed in parallel and subjected to the Click reaction as a control. Data were collected on a BD Dual Fortessa flow cytometer, analyzed using FlowJo v10, and plotted using Prism 7. Datasets show similar variance. All fluorescence values are reported as median fluorescence intensity (MFI). All graphs shown represent fold-change MFI of sample relative to no-EU or no-HPG controls.

Nascent RNA capture followed by qRT-PCR

To measure nascent transcriptional changes at specific loci, ESCs were analyzed using the Click-iT Nascent RNA Capture Kit. $4x10^5$ cells were plated and cultured overnight. The next day, EU was added at a final concentration of 200 μM and cells were incubated for 30 minutes during DMSO or CHX treatment. Cells were washed, harvested by trypsinization and counted (Bio-Rad Automated Cell Counter TC20, Bio-Rad). Total RNA was isolated from the same number of DMSO- or CHX-treated cells using the Qiagen RNeasy Micro Kit (Qiagen) and processed according to the manufacturer's instructions. RNA was quantified using a Qubit 2.0 Fluorometer. qPCR was performed with KAPA SYBR FAST qPCR Master Mix (Kapa Biosystems) and amplified on a 7900HT Real-time PCR machine (Applied Biosystems).

For analysis of FUCCI ESCs, cells were plated overnight before 3h treatment with CHX at 1 μg/ml or DMSO. EU was added at a final concentration of 200 μM for the last 30 minutes of drug treatment. Cells were collected by trypsinization and sorted on a FACS AriaII (BD Biosciences) into mCherry+ (G_0/G_1) and BFP+ ($S/G_2/M$) cell fractions. $2x10^5$ cells of each fraction were sorted for RNA isolation and used for nascent RNA capture as above.

Immunofluorescent staining and imaging

Wild-type E14 ESCs were plated on gelatin in 8-chamber polystyrene vessels. Adhered cells were incubated with DMSO or CHX at the indicated concentrations for 3 hours. Cells were then fixed in 4% paraformaldehyde for 10 minutes, washed with DPBS and permeabilized with 0.2% Triton X-100 in PBS for 5 minutes. After blocking in PBS, 2.5% BSA, 5% donkey serum for 1 hour, cells were incubated overnight at 4^{o}C with anti-H4K5/8/12ac antibody (Millipore, RRID:AB_870989). Cells were washed in PBS-Tween20, 2.5% BSA, incubated with fluorescence-conjugated secondary antibody for 2 hours at room temperature and mounted in VectaShield mounting medium with DAPI (Vector Laboratories). Imaging was performed using a Leica SP5 confocal microscope with automated tile scanning. Blastocyst staining and imaging was performed as described before (Bulut-Karslioglu et al., 2016) using blastocysts flushed at E3.5 and cultured until E4.5 (see Embryo Culture for details). CHX or DMSO was added in the last 3 hours of culture. All quantifications were performed using the Cell Profiler software (Carpenter et al., 2006).

Intracellular flow cytometry

Wild-type E14 ESCs were cultured overnight in FBS/LIF before a 3h incubation in either CHX (100 ng/ml or 1 µg/ml) or DMSO (diluted to 1:10,000). Cells were fixed in 4% PFA for 15 minutes, permeabilized in 0.2% Triton X-100 for 3 minutes on ice, and blocked in 1% BSA in PBS. Primary incubation was performed with anti-H4K16ac antibody (Millipore, RRID:AB_310525) diluted 1:1000 in blocking solution, overnight at 4˚C. Cells were washed and incubated in secondary antibody (AlexaFluor 488, Life Technologies) and fluorescence intensity was measured on a BD Dual Fortessa flow cytometer. Data were analyzed using FlowJo v10. All fluorescence values are reported as median fluorescence intensity (MFI).

Cell cycle staging

Wild-type E14 ESCs were cultured overnight before a 3h incubation in DMSO or CHX (1 µg/ml and 10 µg/ml). 5-ethynyl 2'-deoxyuridine (EdU) was added to a final concentration of 10 µM during the final hour of drug treatment. Cells were trypsinized and processed according to the instructions of the Click-iT EdU Alexa Fluor 488 Flow Cytometry Assay Kit. FxCycle Violet Stain (diluted 1:1000) was used to detect DNA content, per manufacturer's instructions. Data were collected on a BD Dual Fortessa flow cytometer, analyzed using FlowJo v10, and plotted using FlowJo v10 and Prism 7. Statistical analysis by Chi-square test was conducted in Prism 7.

H4K16ac ChIP-seq

H4K16ac ChIPs were performed according to the recommendations of the Diagenode low-cell ChIP kit. Briefly, wt E14 cells were plated and cultured overnight. Cells were treated with CHX 1 µg/ml or DMSO diluted 1:10,000 in FBS/LIF medium for 3h. 10^5 cells were harvested per IP. Lysis and IP were performed in the presence of 1x Halt Protease inhibitors and sodium butyrate. Chromatin was sheared to an average size of 300 bp by a Covaris sonicator with the settings Duty 2, Intensity 3, 200 cycles per burst for 8 minutes. Shearing efficiency was checked by agarose gel. Fixed, sonicated chromatin was obtained from HEK 293 cells using the same method. IPs were performed using antibodies against H4K16ac or rabbit IgG. Following overnight IP and washes, genomic DNA was treated with RNase A. Reverse cross-linking was performed in the presence of Proteinase K at 65˚C overnight. Genomic DNA was cleaned up using Qiagen Minelute Columns and quantified by Qubit. Two biological replicates were collected per condition.

RNA Pol II ChIP-qPCR

ChIP was performed as described before (Brookes et al., 2012). After aspiration of culture medium, cells were washed with PBS and fixed on the culture dish using 1% formaldehyde in

PBS for 10 minutes at room temperature (RT). Glycine was added to a final concentration of 125 mM to quench formaldehyde for 5 minutes at RT. Cells were washed twice with ice-cold PBS, incubated in Swelling Buffer (25 mM HEPES pH 7.9, 1.5 mM $MgCl_2$, 10 mM KCl, 0.1% NP-40 with 1x Halt protease inhibitor cocktail (Thermo Fisher Scientific, Cat # 78425), 1 mM PMSF, 5 mM NaF and 1 mM $NaVO_4$) for 10 minutes, scraped, passed through an 18Gx11/2" needle (5x) and spun down at 3,000g, 4°C, 5 minutes. Nuclei were resuspended in Sonication Buffer (50 mM HEPES pH 7.9, 140 mM NaCl, 1mM EDTA, 1% Triton X-100, 0.1% Na-deoxycholate 0.1% SDS with 1x Halt protease inhibitor cocktail, 1 mM PMSF, 5 mM NaF and 1 mM $NaVO_4$) and sonicated using a Covaris S2 sonicator with settings 5% duty cycle, intensity 4, cycles per burst 200, frequency sweeping. 20 μl chromatin was incubated sequentially with 1 μl RNaseA and 5 μl proteinase K in 100 μl total volume at 37°C for 30 min and 65°C for 1h, purified using a Qiagen PCR purification kit and DNA content was quantified using a NanoDrop. Fragment size distribution was checked on a 1% agarose gel. Chromatin was snap frozen if not immediately used for IP. Chromatin volume equivalent to 25 μg DNA was used for each IP. Chromatin was immunoprecipitated using total 2 μg RNA Pol II (Abcam, RRID:AB_306327) and RNA Pol II S2p (Abcam, RRID:AB_304749) antibodies and 30 μl Protein A Dynabeads per IP in 500 μl total volume of Sonication Buffer overnight at 4°C. Beads were washed 3x with low salt buffer (0.1 % SDS, 1% Triton, 2 mM EDTA, 150 mM NaCl, 10 mM Tris-HCl pH 8.0), 1x with high salt buffer (0.1 % SDS, 1% Triton, 2 mM EDTA, 500 mM NaCl, 10 mM Tris-HCl pH 8.0), 1x with TE buffer (10 mM Tris-HCl pH 8.0, 1 mM EDTA), then resuspended in 100 μl Elution Buffer (50 mM Tris pH 7.5, 1 mM EDTA, 1% SDS). Resuspended beads were sequentially incubated with 1 μl RNaseA 37°C for 30 min with and 5 μl proteinase K at and 65°C for 4h to overnight. Eluate was separated from beads and purified using Qiagen PCR purification columns.

SILAC-Mass Spectrometry

To differentially label wild-type E14 ESCs with light, medium and heavy amino acids, we replaced the following components in the ES-FBS culture medium (see above): DMEM formulated without lysine and arginine instead of DMEM, dialyzed serum instead of regular FBS, lysine and arginine added separately to light (regular L-lysine and L-arginine), medium (L-lysine 4,4,5,5-D4 and L-arginine 13C6) and heavy (L-lysine 13C6, 15N2 and L-arginine 13C6, 15N4) media. All SILAC reagents were purchased from Cambridge Isotope Laboratories. L-proline was included in all media (included in with other non-essential amino acids) and the absence of arginine-to-proline conversion was verified by MS. Complete labeling (>99%) was confirmed by MS before starting the experiment. To quantitatively identify changes in protein levels upon inhibition of protein synthesis, cells were treated with DMSO (light) or 35 µg/ml CHX for 1h (medium) or 3h (heavy). Cells were washed with PBS and lifted in ice-cold PBS with 1x protease inhibitor cocktail (Roche). 10^8 cells from each condition were pelleted and snap-frozen until MS analysis. Harvested cells were lysed in 8M urea in 80 mM NH_4HCO_3, sonicated on ice (3 pulses at 35% power, 20 s each) and centrifuged at 15000g for 10 min. Supernatant was collected and protein concentration estimated with BCA. Equal amounts (100 ug) of the 3 SILAC labeled samples were combined, and the proteins treated with 5 mM DTT at 56C for 10 min, and then with 10 mM iodoacetic acid at RT for 1 h, then diluted 4 times to 2 M urea and digested o/n with trypsin (2% of total protein) at 37C. Samples were acidified with 5% formic, and peptides were extracted using SepPack cartridges. 200 ug of tryptic peptides where resuspended in 20 mM ammonium formiate pH 10.3, and separated in a 1 x 100mm Gemini 3um C18 column (Phenomenex) in a MeCN gradient (2 to 30 % in 60 min) in the presence of 20 mM ammonium formiate pH 10.3. 70 fraction were collected and combined in 18 final fractions, evaporated, resuspended in 0.1 formic acid and analyzed by LCMSMS in a Q Exactive Plus mass spectrometer. Peptides were loaded in a 200 cm monolithic C18 silica column (GL Sciences, Tokyo, Japan), and separated in a gradient of acetonitrile

(288min 2 to 25%, 36 min to 32%, 18 min to 40%, 18 min to 60%, 5 min to 8%) in 0.1% formic The liquid chromatography eluate was interfaced with a 7 μm ID EasySpray emitter (Thermo Scientific) to the MS. Samples were analyzed in positive ion mode, and in information-dependent acquisition mode to automatically switch between MS and MS/MS acquisition. MS spectra were acquired in profile mode in the m/z range between 350-1500 m/z at 70,000 resolution. All samples were analyzed with a TOP10 method, the 10 most intense multiple charged ions over a threshold of 17000 counts were selected to perform HCD experiments. Product ions were analyzed in centroid mode with resolution R=17500. Isolation window was set to 4 Th. A dynamic exclusion window was applied that prevented selection of the same m/z for 10s after its acquisition.

ATAC-seq

ATAC-seq was performed as described before (Buenrostro et al., 2015) on 50,000 cells each of DMSO- or 1 μg/ml CHX-treated E14 ESCs, in quadruplicates. A total of 11 cycles of amplification was performed. Library quality and quantity were analyzed by Bioanalyzer (Agilent) and KAPA library quantification kit for Illumina platforms (KAPA Biosciences). Samples were sequenced on a HiSeq 4000 using single-end 50 bp sequencing reads.

QUANTIFICATION AND STATISTICAL ANALYSIS

H4K16ac ChIP-Seq

HEK 293 chromatin was spiked in to a final concentration of 2.5% before library preparation. Sequencing libraries were prepared using the NEBNext ChIP-seq Library Prep for Illumina Kit (New England Biolabs) following manufacturer's instructions. Libraries were constructed from 3 or 5 ng of DNA and quality was assessed by High Sensitivity DNA Assay on an Agilent 2100 Bioanalyzer (Agilent Technologies). Samples were sequenced on a HiSeq 4000 using single-end 50 bp reads. Sequencing reads that passed quality control were trimmed of adaptors using Trim Galore! and aligned to mm9 and hg19 using bowtie2 (Langmead and Salzberg, 2012) version

2.2.4 with no multimapping. Normalization factors for each sample, excluding inputs, were calculated from the ratio of total reads aligning to mm9 compared to total reads aligning to hg19 (Orlando et al., 2014). Reads were deduplicated using samtools (H. Li et al., 2009) and analyzed by custom R scripts, available upon request. Read coverage was assigned using the featureCounts function of the *Rsubread* package (version 1.24.1) (Liao et al., 2013) in R Bioconductor (Huber et al., 2015), using all coding genes of mm9 with a 2kb 5' extension and disallowing multiple overlap. Read abundance over each gene was scaled by the respective normalization factor and then divided by the read abundance in the corresponding input. Replicate correlation was assessed by Pearson correlation between the top 1000 most-enriched genes, and replicates were pooled by summing the featureCounts of each replicate. Merged samples were used to produce all plots shown. Top-expressed genes were based on published CNN RNA-seq of E14 ESCs (Bulut-Karslioglu et al., 2016). Tag density plots were produced using deepTools on Galaxy (http://deeptools.ie-freiburg.mpg.de/) (Afgan et al., 2016; Ramirez et al., 2016). Boxplots were produced in R. Tracks were visualized using the UCSC Genome Browser.

SILAC-mass spectrometry

Peaklists were generated using PAVA in-house software (Guan et al., 2011) based on the RawExtract script from Xcalibur v2.4 (Thermo Fisher Scientific). The peak lists were searched against the human subset of the UniProt database as of June 17, 2013, (73955/36042779 entries searched) using in-house ProteinProspector with settings described below. A randomized version of all entries was concatenated to the database for estimation of false discovery rates in the searches. Peptide tolerance in searches was 20 ppm for precursor and 30 ppm for product ions, respectively. Peptides containing two miscleavages were allowed. Carboxymethylation of cysteine was allowed as constant modification; acetylation of the N terminus of the protein, pyroglutamate formation from N terminal glutamine, oxidation of methionine, and loss of the protein initial methionine, were allowed as variable modifications, as well as 2H(4) labelling in

lysine and 13C(6) labelling in arginine, and 15N(2) 13C(6) labelling in lysine and 15N(4) 13C(6) labelling in arginine, limiting the allowed combination of labels: if K and R occur in the same peptide, Protein Prospector only allows pairing of K0 with R0, K4 with R6 and K8 to R10. In all cases, the number of modification was limited to two per peptide. A minimal ProteinProspector protein score of 20, a peptide score of 15, a maximum expectation value of 0.05 and a minimal discriminant score threshold of 0.0 were used for initial identification criteria. FDR was limited to 1%. Quantification: SILAC quantification measurements were extracted from the raw data by Search Compare in Protein Prospector. Search Compare averaged together MS scans from -10 s to +30 s from the time at which the MS/MS spectrum was acquired in order to produce measurements averaged over the elution of the peptide. SILAC ratios were calculated, and base 2 logarithms of these values were used for further analysis. If quantitative data are available from isotopic envelopes identified as different charge states of the same peptide, the median of the log2 of the calculated SILAC ratios was used for that peptide. For proteins, the median of all the log2 ratios for peptides unique to that protein was calculated, and the distribution of log2 ratios normalized by its median value.

ATAC-seq

Raw reads were trimmed of adaptors and aligned to the mouse genome build mm10 using Bowtie2 version 2.2.4. Reads were deduplicated, sorted, and converted to bigWig format using samtools. BigWig files from individual replicates were used to assess correlation strength between replicates (Figure S6) using deepTools/multibigwigsummary and plotCorrelation tools. Peak calling was performed on each biological replicate pair using Macs14. Peaks from different biological replicates were then intersected. Peaks which were detected in at least 3 out of 4 replicates were selected for further analysis. As such, 734 peaks were found to be gained and 454 peaks were found to be depleted upon CHX treatment. Gene ontology analysis of these peaks was performed using GREAT software (McLean et al., 2010). The region-gene association

was confined to 5 kb upstream and 1 kb downstream of each gene. To compare enrichment of histone marks, variants and DNase-seq signal over our ATAC-seq peaks, we used the datasets indicated in the Key Resources Table. All heatmaps were generated using the deepTools package (Ramirez et al., 2016) on the Galaxy platform (Afgan et al., 2016). Motif analysis was done using Homer version 4.7 (Heinz et al., 2010). Analysis of repeats was done using repeat annotations from UCSC, custom R scripts and Galaxy Bedtools.

Other

All other replications and statistical analyses are explained in Figure Legends.

DATA AND SOFTWARE AVAILABILITY

Sequencing data have been deposited in Gene Expression Omnibus (GEO) under accession number GSE98358.

Chapter 2:

Usp9x regulates a peri-implantation switch in PRC2 activity

Introduction

Chromatin state transitions are central to stem cell fate determination (Chen and Dent, 2014). Pluripotent stem cells *in vitro* and in the peri-implantation embryo undergo extensive rewiring of their chromatin landscape in preparation for lineage commitment (Gökbuget and Blelloch, 2019). Crucially, this remodeling includes a global redistribution of repressive histone H3 lysine 27 tri-methylation (H3K27me3) from broad distal blankets to promoter-proximal peaks at developmental genes (Zheng et al., 2016) (van Mierlo et al., 2019), raising questions about the molecular mechanisms that regulate facultative heterochromatin in peri-implantation development. Here we report that the deubiquitinase Usp9x promotes activity of Polycomb Repressive Complex 2 (PRC2), the highly conserved complex that deposits H3K27me3. We show that Usp9x levels capture the molecular transitions at implantation with remarkable fidelity. Transcriptome and chromatin analyses reveal that Usp9x-high mouse embryonic stem (ES) cells bear a molecular signature of pre-implantation, including elevated PRC2 activity and H3K27me3 deposition. Usp9x-low ES cells resemble the post-implantation, gastrulating epiblast. *Usp9x* deletion in the pluripotent epiblast manifests as developmental delay by embryonic day 9.5, and mutant embryos show evidence of delayed repression of early lineage genes. Mechanistically, we show that Usp9x deubiquitinates core members to promote pervasive H3K27me3 deposition. Usp9x recurs as a marker of “stemness” (Blanpain et al., 2004; Ramalho-Santos et al., 2002); is essential for fly, mouse, and human development (Fischer-Vize et al., 1992; Nagai et al., 2009); and is mutated in various neurological disorders and cancers (Murtaza et al., 2015). The regulatory axis outlined here may therefore apply to other settings where Usp9x and PRC2 regulate transitions in cell fate.

Results

We identified Ubiquitin Specific Protease 9x (Usp9x) in a recent RNAi screen for regulators of the chromatin state of ES cells cultured in serum with leukemia inhibitory factor (LIF) (Bulut-Karslioglu et al., 2018), which mimic the fast-growing pluripotent cells of the peri-implantation epiblast. To explore the roles of Usp9x in these cells, we established an auxin inducible degron (AID) model for targeted, tunable depletion of Usp9x at the protein level (Nishimura et al., 2009) (Fig. 1a). In ES cells homozygous for the *OsTir1* auxin receptor, we tagged endogenous *Usp9x* with enhanced green fluorescent protein (GFP) and a minimal AID or a 3x Flag tag (AID-Usp9x or Flag-Usp9x herein). Auxin drives Usp9x depletion within hours (Fig. S1a), although a subpopulation of cells resists degradation (Usp9x-high). We chose 8 hours (h) of auxin as the standard treatment duration and sorted Usp9x-high and Usp9x-low fractions by GFP expression (Fig. 1a, S1b-c).

Serum ES cells represent a heterogeneous mixture of “metastable” pluripotent cell states, and subpopulations are usually interconvertible. Usp9x-high and Usp9x-low fractions express comparable Oct4, but the latter show reduced Nanog (Fig. 1b). In colony formation assays, Usp9x-low ES cells show a ~5-fold self-renewal deficit relative to Usp9x-high or untreated ES cells (Fig. 1b). Surprisingly, isolated Usp9x-low cells did not re-distribute along a spectrum of expression after a 48h recovery without auxin (Fig. S1d-e), unlike the dynamics of some naïve pluripotency markers (Hackett and Surani, 2014).

To characterize Usp9x-high and Usp9x-low cells, we performed spike-in RNA-sequencing (RNA-seq). By principal component analysis (PCA), replicates cluster according to Usp9x status, and sorted control cells—including AID-Usp9x cells without auxin and Flag-Usp9x cells after auxin treatment—form an intermediate cluster (Fig. 1c). We calculated differential expression (DE) in Usp9x-high or Usp9x-low ES cells versus controls and compared their profiles to molecular

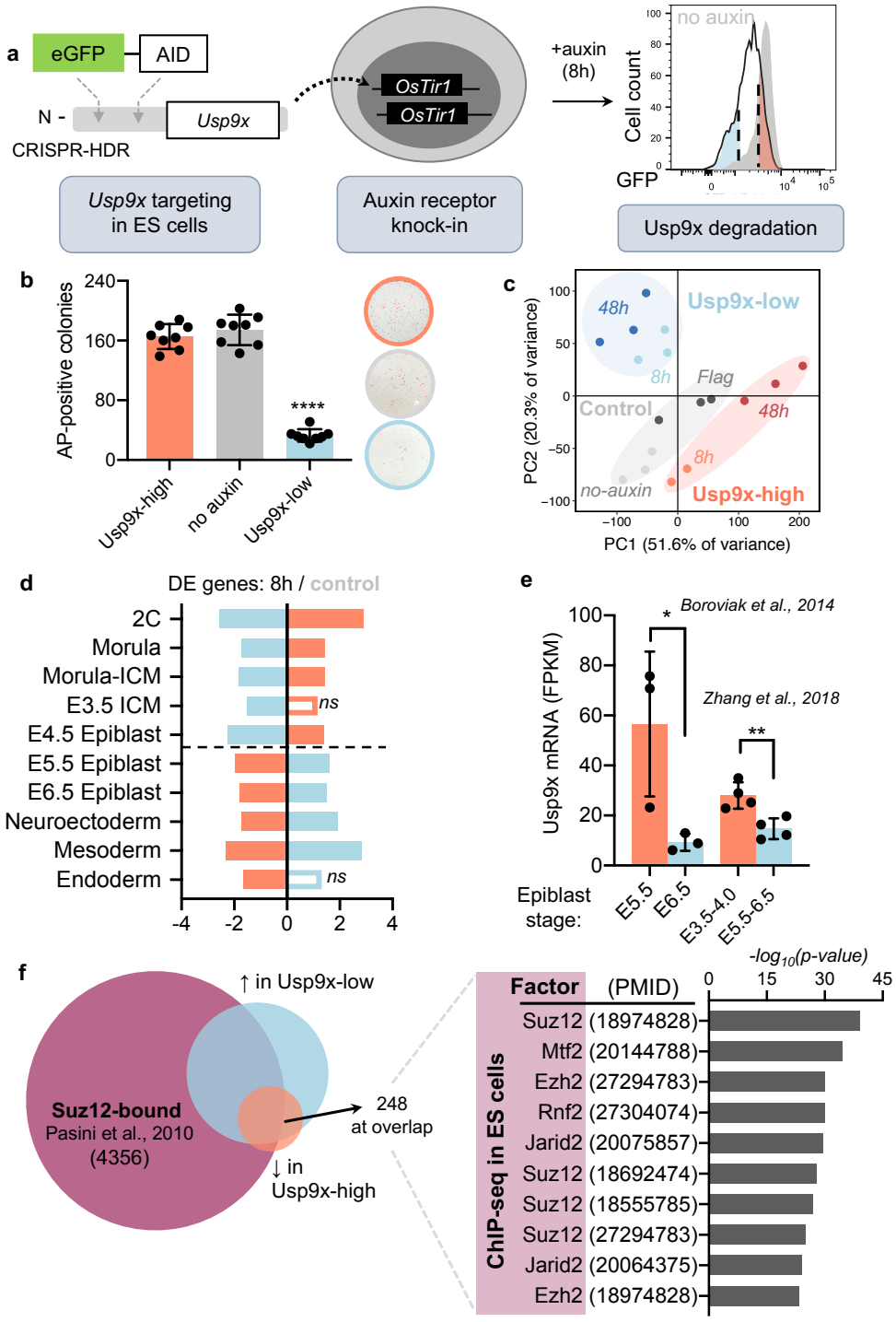

Figure 2.1. Usp9x level in ES cells captures a molecular signature of peri-implantation development.

a) Schematic of an auxin-inducible degron (AID) system for acute Usp9x depletion in mouse embryonic stem (ES) cells homozygous for *OsTir1*, the auxin receptor. See Methods for details. b) Usp9x-low ES cells show a self-renewal deficit. Representative images and quantification of colony formation assays (CFA) 5 days after plating at clonal density. Error bars depict mean ± SD of 4 replicate CFAs performed in two independent sorts. ****p < 0.0001 by one-way ANOVA

and multiple t-test comparisons to the no-auxin condition. c) Principal Component Analysis (PCA) of gene expression by spike-in normalized RNA-seq in the indicated samples. Each point represents a biological replicate. 8h: 8h auxin treatment. No-auxin: AID-Usp9x cells with vehicle (water) treatment. 48h: 8h auxin treatment followed by 48h recovery in serum/LIF medium. Flag: Flag-Usp9x cells after 8h auxin and 48h recovery. All cells were sorted. d) Transcriptional signatures of Usp9x-high or Usp9x-low ES cells correlate with different embryonic stages by Gene Set Enrichment Analysis (GSEA). Genes were ranked by differential expression (DE) and compared to gene lists representing the indicated stages of wild-type development. See Methods for references. *NS*, not significant (false discovery rate (FDR) > 0.05). e) Usp9x mRNA expression in the epiblast declines from pre- to post-implantation. Data are from (Boroviak et al., 2015; Zhang et al., 2018). Error bars depict mean ± SD of 3-4 replicates. *p < 0.05, **p < 0.01 by Student's t-test with Welch's correction. f) Usp9x-high and Usp9x-low ES cells share many (248) DE genes that are targets of Polycomb Repressive Complex 2 (PRC2). Bar graph depicts the results of ChIP Enrichment Analysis by the Enrichr suite. A sample Suz12 dataset is shown in the Venn diagram at left, using the top-enriched factor from Enrichr. 172 of 248 overlapping DE genes (72%) are Suz12 targets (*P* < 2.2x10e16 by Fisher exact test) (Pasini et al., 2010a).

signatures of development using Gene Set Enrichment Analysis (GSEA) (Subramanian et al., 2005). We observed striking polarity based on Usp9x status; whereas the Usp9x-high state correlates to pre-implantation embryonic stages, Usp9x-low ES cells resemble the post-implantation epiblast and early lineages (Fig. 1d, S1e). Importantly, Usp9x expression itself declines from pre- to post-implantation in wild-type embryos (Fig. 1e)3, highlighting the physiologic relevance of this correlation.

The opposing molecular signatures Usp9x-high and Usp9x-low cells are reinforced after the 48h recovery (Fig. S1d). A salient difference between the two populations is a global difference in steady-state transcript levels. Usp9x-high cells settle into a state of *hypo*transcription (Bulut-Karslioglu et al., 2016), showing a suppression of the majority of the transcriptome relative to control cells. By contrast, Usp9x-low cells demonstrate relative *hyper*transcription, including ribosomal protein gene induction (Fig. S2a-b) (Percharde et al., 2017a) (Percharde et al., 2017a; 2017b). They also upregulate genes associated with differentiation- and development-related Gene Ontology (GO) terms, while the pattern of downregulated genes is reminiscent of a hypomethylated, naïve state of pluripotency driven by vitamin C addition to naïve (2i) ES cell

culture (Fig. S2c) (Blaschke et al., 2013). Taken together, these results show that Usp9x level models the molecular progression at implantation.

We wondered if the transcriptional signature of the acute (8h) time point held clues to the gene regulatory network establishing divergent cell fates. Consistent with their diametric GSEA signatures, Usp9x-high and Usp9x-low ES cells show polarized expression of many of the same genes. Of the 277 significantly downregulated genes in Usp9x-high cells, 248 (90%) are significantly DE but induced in Usp9x-low cells. ChIP-X Enrichment Analysis (ChEA) revealed that the divergent genes are highly enriched for Polycomb target genes, especially those bound by PRC2 (Fig. 1f) (Chen et al., 2013; Kuleshov et al., 2016; Pasini et al., 2010a). PRC2 is considered dispensable for pluripotency, as PRC2-knockout ES cells can be propagated in serum/LIF, albeit with precocious activation of lineage genes (Boyer et al., 2006; Leeb et al., 2010). Derepression of PRC2 target genes in Usp9x-low ES cells, however, leads to spontaneous differentiation (Fig. S2d), behavior that resembles *PRC2* deletions in primed mouse or human ES cells (Collinson et al., 2016; Moody et al., 2017; Shan et al., 2017). Taken together, these data suggest that Usp9x-high ES cells represent a highly PRC2-repressed, pre-implantation-like state of pluripotency, while premature activation of PRC2 targets in Usp9x-low ES cells promotes precocious differentiation.

We turned to the mouse embryo to study the consequences of Usp9x loss for developmental progression. To avoid possible roles in pre-implantation and trophectoderm development (Abed et al., 2019; Pantaleon et al., 2001), we crossed *Sox2-Cre* males with *Usp9x*$^{fl/fl}$ females to delete *Usp9x* strictly in epiblast derivatives of offspring (Hayashi et al., 2002). We genotyped and catalogued the morphology of mutant (mut, *Usp9x*$^{\Delta/X}$) versus control (ctrl, *Usp9x*$^{fl/X}$) embryos at several post-implantation stages (Fig. 2a, S3a).

Deviation from the expected (1:1) ratio arose by E11.5, at which point mutants accounted for only ~25% of recovered embryos and showed morphological abnormalities with 100% penetrance. Mutants that survive to E11.5 were relatively well-formed but show extensive hemorrhaging. The remainder showed pericardial edema, cerebral edema, and severe delay, pointing to a much earlier developmental arrest (Fig. 2b). At E9.5, *Usp9x* mutants showed developmental delay (delayed turning, open anterior neuropore) or gross abnormalities, including blunted posterior trunk development and exencephaly (Fig. 2b). These pleiotropic outcomes align with the phenotypes of chimeras derived from *Usp9x*-gene-trapped ES cells by E9.5 and the ubiquitous expression of Usp9x at E9.5 (Cox et al., 2010; Wood et al., 1997).

Going back one day in development to E8.5, *Usp9x* mutants appeared morphologically normal (Fig. S3c). This stage corresponds to the early stages of organogenesis, just after the dissolution of pluripotency (Beddington, 1983; Damjanov et al., 1971; Kojima et al., 2014). To find molecular changes anticipating later developmental delay, we performed whole-embryo RNA-seq on litter-matched controls and mutants from 2 litters (Fig. S3c). Mutants largely cluster away from controls by PCA and unsupervised hierarchical clustering (Fig. 2c, S3d). Thus, even though mutants appear normal at E8.5, they are readily distinguished from controls at the transcriptional level.

To account for staging differences between litters, we called DE genes between mutants and controls within each litter, applied a statistical cutoff (adjusted $P < 0.1$), and overlapped the gene lists to obtain refined sets of 71 upregulated and 66 downregulated genes in all mutants (Fig. 2d). Upregulated genes include targets of homeodomain-containing transcription factors (Isl1, F-box, Sox, T-box) that serve lineage-specific regulatory roles (Fig. 2e). The most-enriched factor is Isl1, an early marker of cardiac progenitor cells (Cai et al., 2003), consistent with GO analysis demonstrating upregulation of cardiac development among mesoderm and endoderm terms (Fig. S3e). As the heart is one of the first organs to develop, we wondered if *Usp9x* mutants still express

early genes at E8.5. Indeed, the genes upregulated in *Usp9x* mutants typically decline between E6.5 and E8.5 in wild-type embryos (Fig. 2f) (Beccari et al., 2018).

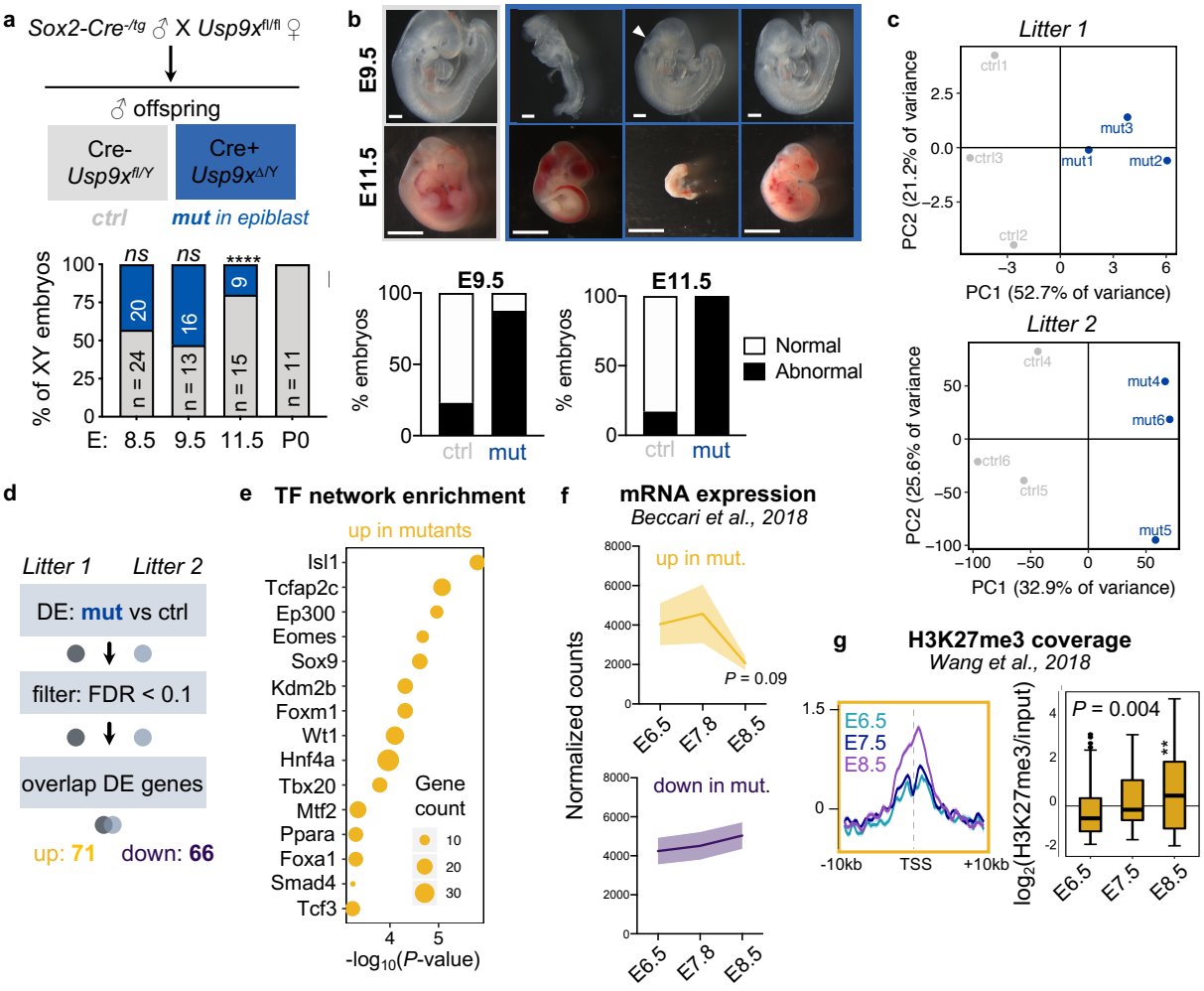

Figure 2.2. *Usp9x*-mutant embryos are slow to repress early lineage programs.
a) Schematic of genetic cross to delete *Usp9x* in epiblast derivatives of embryos. Below, quantification of male (XY) embryos at several post-implantation stages. We focused on XY embryos to extend our findings from XY mouse ES cells. b) Representative images of ctrl. Scale bar = 250 μm for E9.5, 2.8 mm for E11.5. Quantification is shown at right. c) PCA plots of mutants (mut) and controls (ctrl), numbered by litter. d) Outline of method to obtain differentially-expressed gene lists between mutant and control embryos. e) Output of Enrichr analysis for transcription factor (TF) binding enriched at genes up-regulated in *Usp9x* mutants. The 15 top-enriched features are shown. e) Expression of genes up- or down-regulated in the mutants during wild-type development (Beccari et al., 2018). f) During wild-type development (Wang et al., 2018), H3K27me3 accumulates over the genes upregulated in *Usp9x* mutants. Bottom panel: quantification of H3K27me3 signal over genes +10kb upstream. *P*-values obtained by $\chi 2$ test (a, b), Student's t-test with Welch's correction (f), and Wilcoxon rank-sum test (g). Lines show mean ± S.E.M. of 2-3 replicates per condition (f, g).

Delayed gene repression evokes the phenotype of PRC2-hypomorphic ES cells, which differentiate poorly due to inefficient repression of early genes and alternate lineage programs (Pasini et al., 2007; Thornton et al., 2014). In zebrafish and Xenopus (Akkers et al., 2009; Rougeot et al., 2019), PRC2 is essential for stage- and spatially-restricted expression of developmental regulators after gastrulation. The roles of PRC2 in the post-implantation epiblast remain obscure, as early reports observed peri-gastrulation lethality of constitutive *PRC2*-knockout embryos (Faust et al., 1995; O'Carroll et al., 2001; Pasini et al., 2004), although these findings are confounded by requirements for PRC2 in extraembryonic tissues (Rugg-Gunn et al., 2010). Intriguingly, recent chromatin immunoprecipitation-sequencing (ChIP-seq) studies documented a wave of de novo and spatially-regulated heterochromatin deposition after implantation in wild-type mouse embryos (Wang et al., 2018; Yang et al., 2019). We mined these data for the expected H3K27me3 dynamics over genes dysregulated in *Usp9x* mutants (Wang et al., 2018). The upregulated genes normally amass significant H3K27me3 by E8.5 (Fig. 2g), suggesting that heterochromatin helps repress them over time.

One upregulated gene reported to accumulate H3K27me3 in a spatial manner is Nodal (Yang et al., 2019), the TGF-beta superfamily member (Fig. S3f). Ongoing expression of factors such as Nodal may directly impede development. Consistent with this notion, the 66 genes *down*regulated in mutants are enriched for repressive chromatin factor binding, are normally induced between E6.5-E8.5, and correspond to protein metabolism and neuron morphogenesis GO terms (Fig. 2f, S3e,g-h). Taken together, these results suggest that *Usp9x*-mutant embryos are slow to repress early lineage genes. One explanation is that Usp9x promotes timely H3K27me3 deposition in early organogenesis.

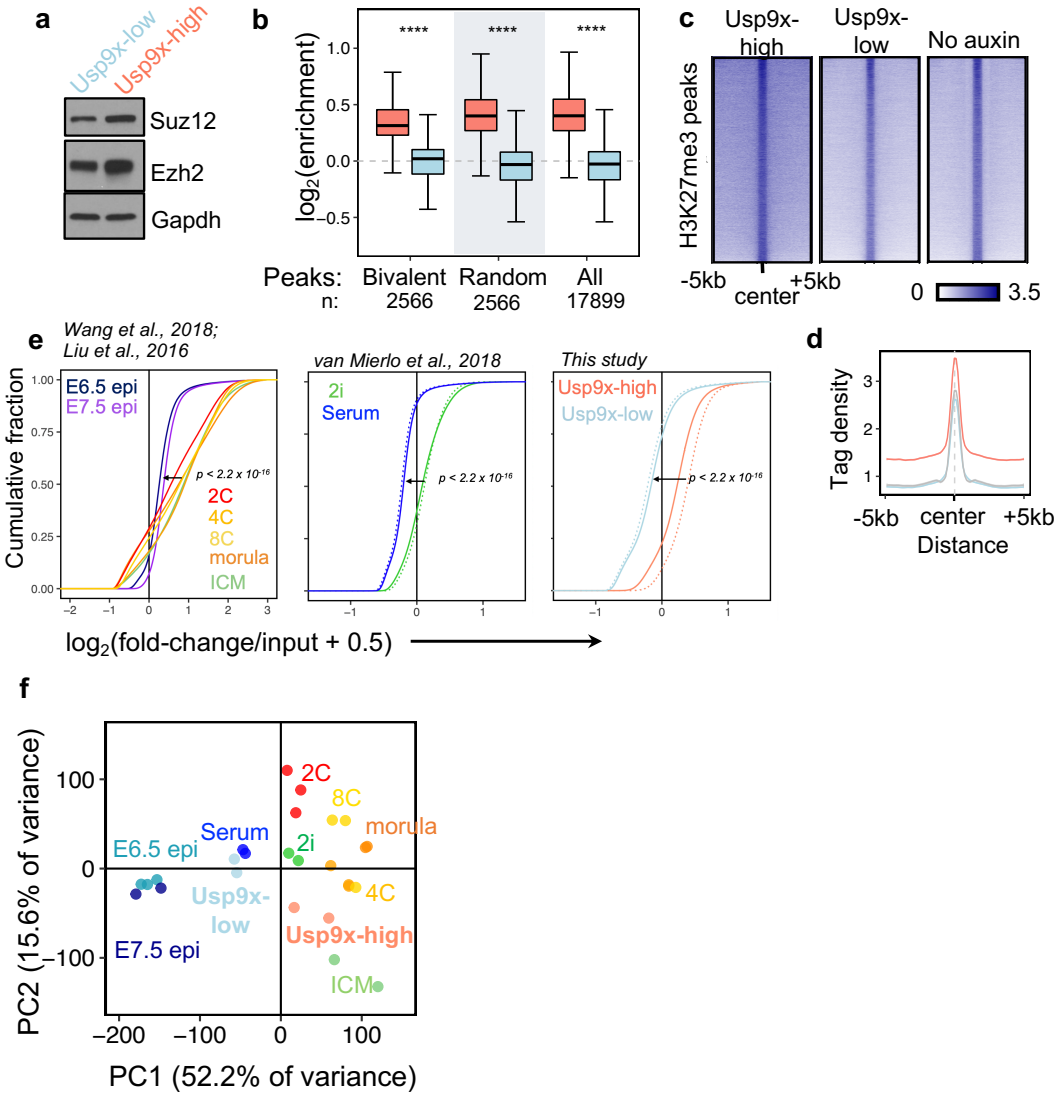

Figure 2.3. Usp9x promotes pervasive H3K27me3 deposition.
a) CNN western blots for PRC2 proteins in whole cell extracts, representative of 3 biological replicates. b) H3K27me3 coverage in Usp9x-high or Usp9x-low cells over bivalent peaks, a random peak set of the same size (2566), or all peaks found in ES cells at baseline (no auxin). c) Heatmaps depicting H3K27me3 chromatin immunoprecipitation (ChIP) signal spreading outside of peaks in Usp9x-high ES cells. Peaks are the same set in (b) and normalized to consistent lengths. d) Profile plot depicting the mean signal of coverage shown in (c). e) Pre-implantation embryos show global enrichment of H3K27me3 compared to post-implantation stages (E6.5 epiblast and E7.5 epiblast, epi). Plots show H3K27me3 reads falling in non-overlapping 10kb bins across the genome, adjusted for library size or exogenous spike-ins as relevant. f) PCA plots clustering Usp9x-high and Usp9x-low ES cells among the samples shown in (e) based on H3K27me3 distributions. PC1 separates pre-implantation-like from post-implantation-like states. Each point represents a biological replicate. Data from embryos as well as 2i and serum ES cells are from published sources (Liu et al., 2016; van Mierlo et al., 2019; Wang et al., 2018). ****$p < 2.2x10^{-16}$ by Wilcoxon rank-sum test (b) or Kolmogorov-Smirnov (KS) test (e). KS tests were performed on the average of replicates and the average of pre-implantation vs post-implantation states.

We returned to ES cells to explore how Usp9x regulates PRC2 activity. Consistent with a transcriptional signature of PRC2 derepression (Fig. 1f), Usp9x-low ES cells express PRC2 proteins at lower levels and show reduced H3K27me3 compared to Usp9x-high ES cells (Fig. 3a, Fig. S4a-b). We mapped changes between cell states using ChIP-seq. Usp9x-high cells show relative enrichment of H3K27me3 over bivalent promoters (Fig. 3b) (Marks et al., 2012), canonical PRC2 targets in ES cells. Gains are not limited to bivalent genes, however, as Usp9x-high cells are marked by higher H3K27me3 over all peaks present at baseline (no-auxin) as well as up- and down-stream of peaks (Fig. 3c, Fig. S4c). They also show H3K27me3 enrichment over repetitive elements (Fig. S4d) (Walter et al., 2016).

The pattern of Usp9x-high ES cells resembled recent reports that early embryos and naïve ES cells in 2i carry H3K27me3 in diffuse domains, not just at promoter-proximal peaks (Højfeldt et al., 2019; Kumar and Elsässer, 2019; van Mierlo et al., 2019; Zheng et al., 2016). Cumulative enrichment plots confirm the global elevation of the mark in Usp9x-high cells, resembling the pattern in 2i versus serum ES cells. Remarkably, a similar contrast emerges between pre-implantation stages and the post-implantation epiblast at E6.5 and E7.5 (Fig. 3e). PCA separates pre-implantation and post-implantation embryos along PC1. ES cell data follow this trajectory, with Usp9x-high and 2i ES cells aligning with pre-implantation while Usp9x-low and serum ES cells cluster with post-implantation stages (Fig. 3f). These results indicate that H3K27me3 enrichment across large swathes of the genome is a hallmark of pre-implantation pluripotency (Erhardt et al., 2003; Saha et al., 2013; Zhang et al., 2009).

Given the above results, we hypothesized that Usp9x is a PRC2 deubiquitinase. In co-immunoprecipitation assays on endogenous proteins, Usp9x interacts with Ezh2 and Suz12 in nuclear extracts from ES cells (Fig. 4a, S5a). Acute Usp9x depletion using the AID system led to

gain of poly-ubiquitinated forms of Suz12 and Ezh2 (Fig. 4b). Finally, loss of Usp9x activity in wild-type ES cells, either by the small molecule catalytic inhibitor WP1130 or overexpression of a mutant catalytic domain (C1566S), leads to accumulation of poly-ubiquitinated Ezh2 (Fig. S5b-c, Fig. 4c). Gain of ubiquitin tends to correlate with destabilization of Suz12 and Ezh2 (Fig. 4b-c). Taken together, these biochemical assays suggest that Usp9x acts as a PRC2 deubiquitinase in mouse ES cells.

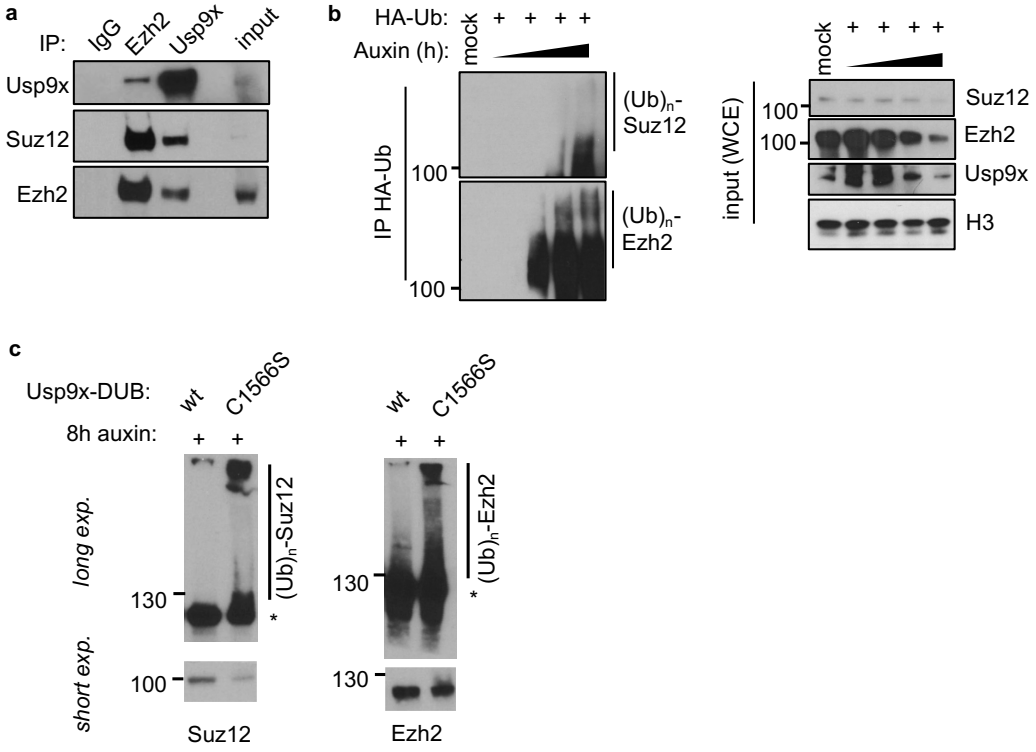

Figure 2.4. Usp9x is a PRC2 deubiquitinase.
a) Reciprocal co-immunoprecipitation (co-IP) of Ezh2 and Usp9x in wild-type ES cells. Both proteins also pull down Suz12. b) Acute auxin depletion over at time course from 0-8h leads to gain of ubiquitin at PRC2 proteins. HA-Ubiquitin (HA-Ub) was expressed at low levels to enable immunoprecipitation (IP). The high molecular weight smears represent ubiquitinated species of Suz12 and Ezh2 (designated by $(Ub)_n$). Input samples show destabilization of Suz12 and Ezh2. c) Comparison of overexpressing a wild-type (wt) versus catalytic-mutant (C1566S) form of the Usp9x catalytic domain in wild-type ES cells. Cells were treated with 8h auxin to deplete endogenous Usp9x. Whole cell-extracts are shown. At long exposures, high molecular-weight species of Suz12 (left) and Ezh2 (right) represent polyubiquitinated forms. Short exposure times show destabilization of the proteins. Westerns are representative of 2-3 biological replicates.

Discussion

Via transcriptional analysis of acute Usp9x depletion, we identified PRC2 members as key targets of Usp9x in ES cells. Mechanistically, we demonstrate that Usp9x deubiquitinates core PRC2 complex members and promotes high levels of H3K27me3 in ES cells. H3K27me3 is abundant in pre-implantation embryos (Erhardt et al., 2003; Saha et al., 2013; Zhang et al., 2009), where it marks transposable elements during hypomethylation (Walter et al., 2016; Wang et al., 2018) and regulates maternal imprints (Inoue et al., 2017; Matoba et al., 2018). That Usp9x-high ES cells enter a state of global hypotranscription implies that ubiquitous H3K27me3 suppresses large-scale transcription prior to implantation (Fig. S1a-b), possibly by preventing H3K27 acetylation (Lavarone et al., 2019; Lee et al., 2015; Pasini et al., 2010b).

Our results in ES cells suggest that physiologic decline of Usp9x at implantation helps constrict PRC2 activity during lineage induction (Fig. 5). RNA-seq in *Usp9x*-mutant epiblasts highlights the requirement for PRC2 to maintain fidelity of lineage commitments. Studies in mammalian systems have emphasized roles of PRC2 in regulating bivalent promoters, but evidence abounds that broad H3K27me3 domains arise in diverse cell types (Carelli et al., 2017; Hawkins et al., 2010; Pauler et al., 2009; Young et al., 2011). In fact, bivalency may represent a nadir of PRC2 activity—a mechanism to minimize expression of developmental regulators amidst low PRC2 expression (Miro et al., 2009; Mitiku and Baker, 2007); hypertranscription and lineage priming (Bulut-Karslioglu et al., 2018; Gaspar-Maia et al., 2009; Guzman-Ayala et al., 2014), rapid cell cycles that oppose H3K27me3 inheritance (Reverón-Gómez et al., 2018; Snow, 1977); and accumulation of H3K27me3 antagonists, including demethylases, DNA methylation, and activating chromatin marks (Schmitges et al., 2011; Wang et al., 2017). Consistent with this notion, bivalent promoters are CpG-dense and high-affinity PRC2 targets, sites where accessory proteins cooperatively recruit PRC2 in mammalian cells (Højfeldt et al., 2019; Li et al., 2017;

Oksuz et al., 2018; Perino et al., 2018). PRC2 deposits H3K27me2 throughout the genome, but binds transiently and is seldom detected outside of H3K27me3 peaks in ES cells (Ferrari et al., 2014; Laugesen et al., 2019). Oncogenic *EZH2* mutations stabilize the complex and cause widespread gain of H3K27me3 (McCabe et al., 2012; Sneeringer et al.; Yap et al., 2011). Our results highlight post-translational regulation as another mechanism to stabilize PRC2 at chromatin and promote H3K27me3 at low-affinity sites. Future studies are necessary to understand how Usp9x integrates activities of other substrates with PRC2 and to identify the E3 ubiquitin ligase(s) that acts on PRC2 in early development.

Supporting the designation of Usp9x as “stemness” factor, loss-of-function studies document that Usp9x limits stem/progenitor cell expansion during neural development (Premarathne et al., 2017), T cell development (Naik et al., 2014), and intestinal regeneration (Khan et al., 2018). In humans, *USP9X* mutations are implicated in X-linked neurodevelopmental syndromes (Homan et al., 2014; Reijnders et al., 2016; Tarpey et al., 2009), Parkinson disease (Rott et al., 2011), Turner Syndrome (Jones et al., 1996), seizures (Paemka et al., 2015), and numerous cancers (Bailey et al., 2018; Pérez-Mancera et al., 2012; Schwickart et al., 2010). PRC2 has well-appreciated roles in human physiology, ranging from development to cancer (Comet et al., 2016; Deevy and Bracken, 2019). Thus, although we have focused on peri-implantation development, a Usp9x-PRC2 axis that specifies H3K27me3 domains has broad biomedical implications.

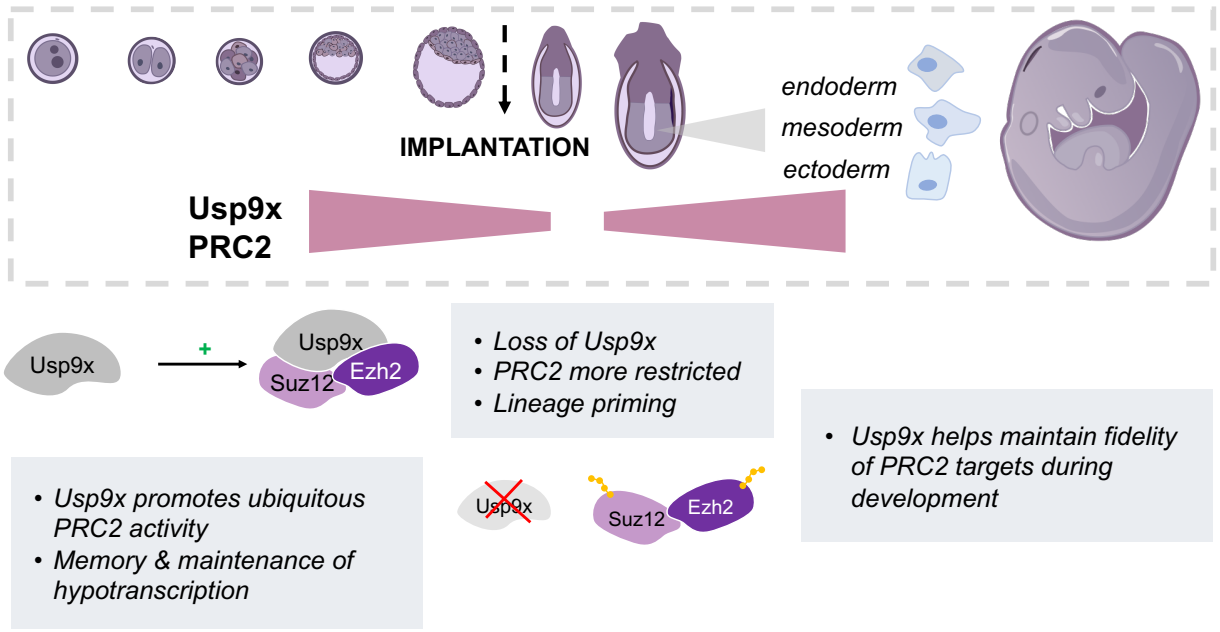

Figure 2.5. Model for the role of Usp9x in regulating PRC2 activity in peri-implantation development and early lineage commitment.
Our results suggest that the Usp9x-PRC2 axis acts at two points during early development. First, during pre-implantation, Usp9x deubiquitinates and stabilizes core PRC2 members Suz12 and Ezh2. This results in high activity of the complex, repression of lineage genes, and self-renewal. Second, re-expression of Usp9x after E8.5 may stabilize PRC2 during a wave of de novo H3K27me3 deposition after lineage formation. *Usp9x*-mutant epiblasts show molecular abnormalities by E8.5 defined by ongoing expression of early lineage pathways.

Supplemental Figures

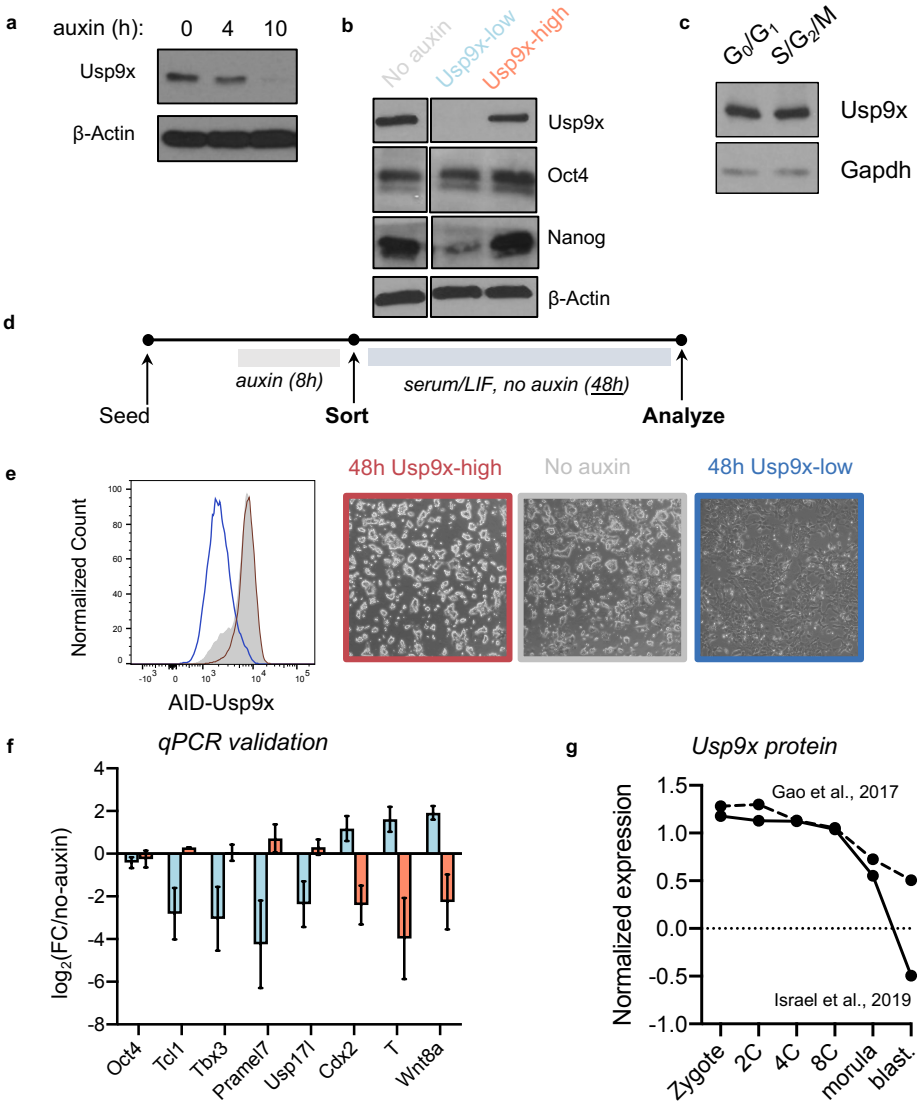

Figure S2.1. Characterization of the AID-Usp9x ES cell line.
a) Auxin treatment drives acute Usp9x depletion at the protein level. Cell-number normalized (CNN) western blot of endogenous Usp9x protein over a time course of auxin, 0-10h. b) CNN western blot confirming endogenous Usp9x depletion in Usp9x-low and retention in Usp9x-high ES cells, sorted as depicted in (a). c) The Usp9x-low does not represent a distinct phase of the cell cycle. ES cells were sorted by stage according to a FUCCI cell cycle reporter (Nora et al., 2017). d) Diagram of experiments assessing the ability of sorted Usp9x-high or Usp9x-low ES cells to recover after acute auxin treatment, relevant to (c) and Fig. S2. e) After recovery, 48h Usp9x-low ES cells do not recover Usp9x expression, measured by GFP fluorescence, and adopt heterogeneous, differentiated morphologies. f) Usp9x protein expression declines over pre-implantation development. Normalized data are plotted from quantitative proteomic analysis of wild-type embryos in (Gao et al., 2017; Israel et al., 2019). All western blots represent 2-3 biological replicates.

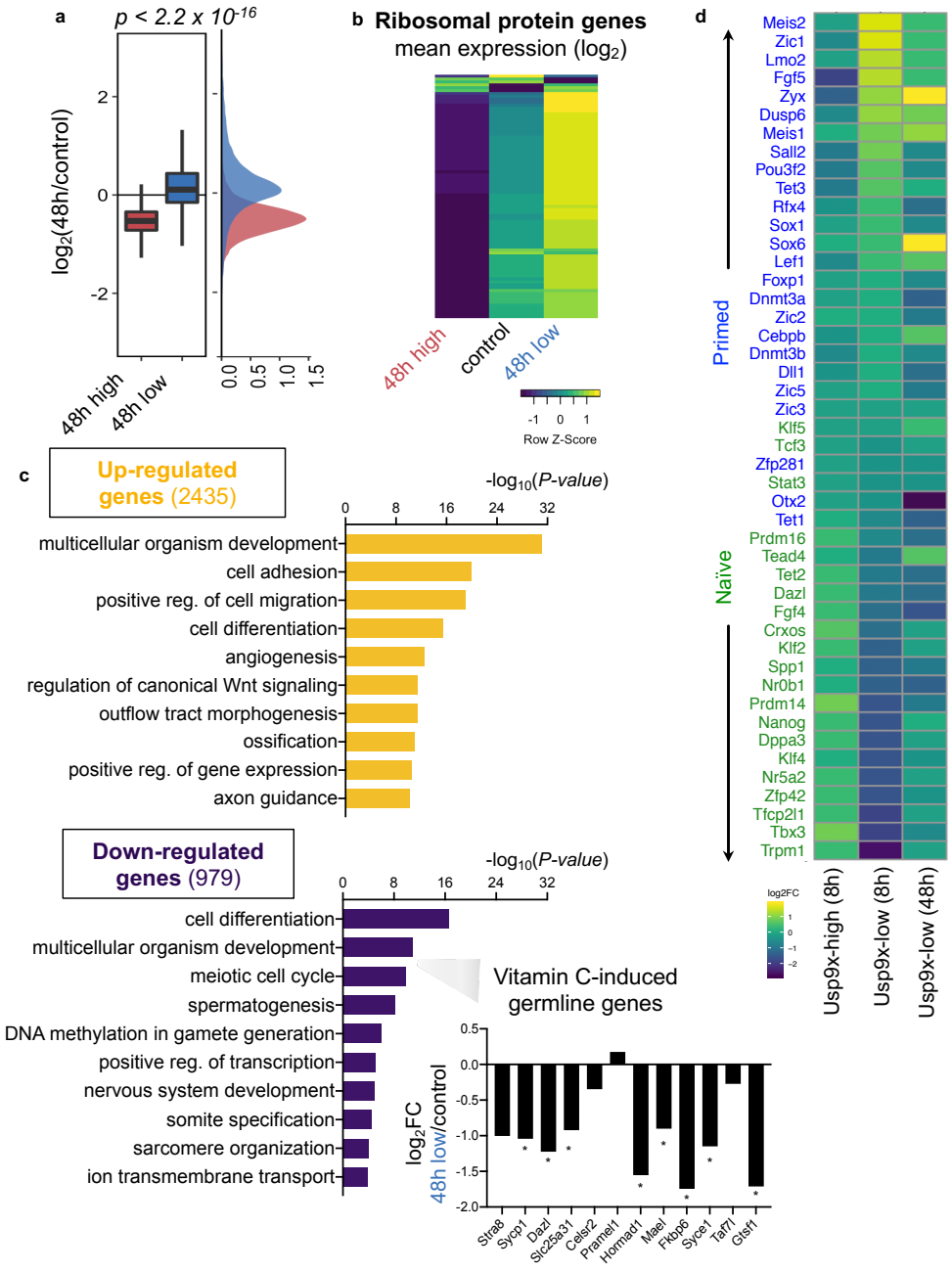

Figure S2.2. Isolating ES cells by Usp9x expression induces divergent cell fates.
a) Steady-state transcriptomes of 48h Usp9x-high or Usp9x-low ES cells based on spike-in normalized RNA-seq. Boxplot and density plots show $\log_2$ fold-change expression of all genes relative to expression in control cells. *P*-value calculated by the Wilcoxon rank-sum test. b) Relative expression of ribosomal protein genes in Usp9x-high, Usp9x-low, or control cells at 48h. c) Gene Ontology (GO) analysis of genes significantly upregulated or downregulated in Usp9x-low ES cells after 48h, relative to controls. Inset: germline genes induced by vitamin C addition to naïve ES cell culture. The output of DEseq2 is plotted as $\log_2$ fold-change (FC) in expression. *adjusted *P*-value < 0.05 from Wald test. d) Relative expression of a selection of primed and naïve pluripotency genes (Kalkan et al., 2017). Data are plotted as $\log_2$ fold-change in expression relative to controls.

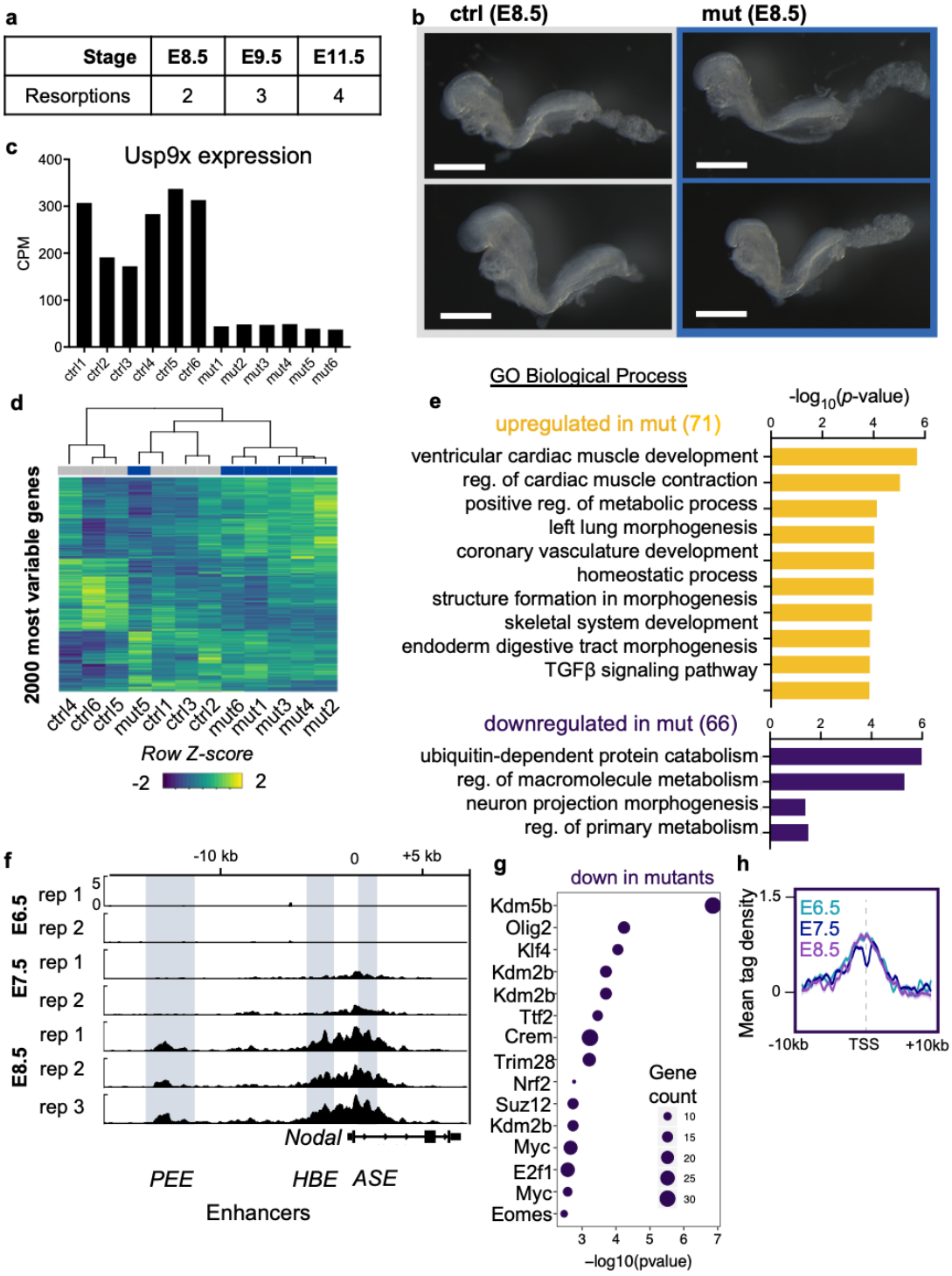

Figure S2.3. Further analysis of RNA-seq from E8.5 *Usp9x*-mutant embryos.
a) Number of resorptions counted at the indicated stages (no embryonic material detected in deciduum). They represent presumed mutants. b) Additional ctrl and mut XY embryos dissected at E9.5 and E11.5. Scale bar = 250 μm for E9.5, 2.8 mm for E11.5. c) Representative ctrl and mut embryos at E8.5, used for RNA-seq. Mutants were morphologically indistinguishable from controls at this stage. In total, n = 12 embryos collected from 2 litters were sequenced. Scale

bar = 500 μm. d) Normalized counts confirming low Usp9x mRNA expression in the 6 mutant embryos used for RNA-seq.
e) Unsupervised hierarchical clustering of the top 2000 most variable genes across samples from RNA-seq. Mutants largely cluster away from controls, except for mut5 (litter 2), which clusters with the controls from litter 1. f) Top-enriched GO terms for up- and down-regulated genes in *Usp9x* mutants. g) Enrichr TF analysis as in Fig. 2e but for genes downregulated in mutants. These genes are targets of repressive chromatin factors such as Kdm5b, Kdm2b, Trim28, and Suz12. Below, profile plots of H3K27me3 around the downregulated gene set. h) Sample genome browser tracks of H3K27me3 in wild-type embryos (E6.5-E8.5) at the *Nodal* locus. Known enhancer elements are highlighted and show gains of H3K27me3.
Embryo H3K27me3 data are from Wang et al. (Wang et al., 2018). Lines show the mean ± S.E.M. of 2-3 replicates per time point, and sample tracks show representative replicates.

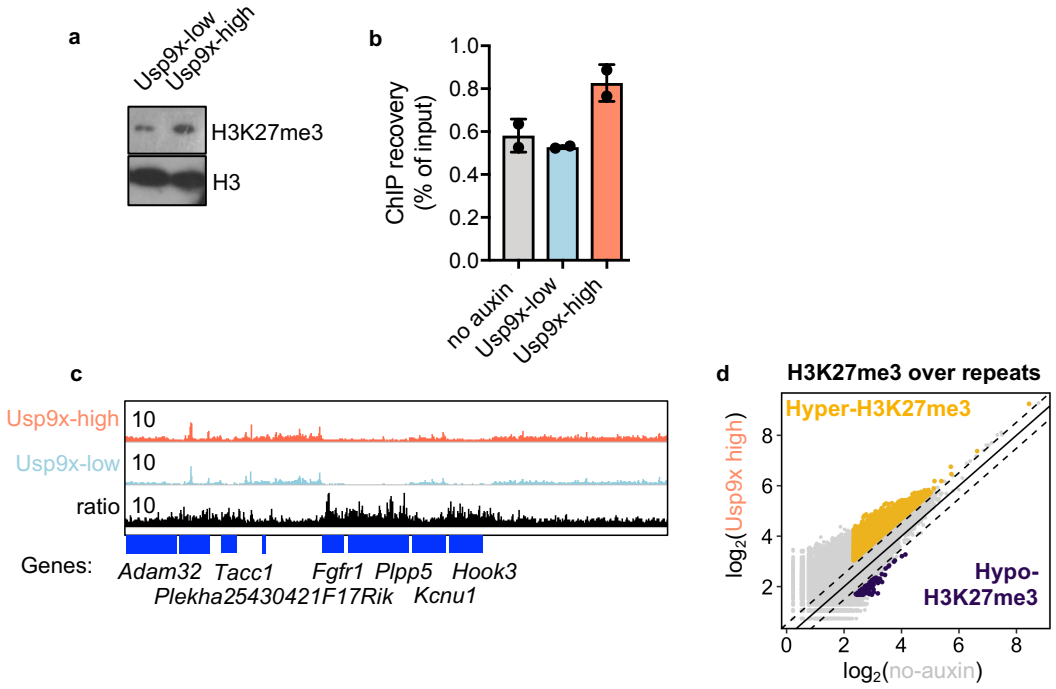

Figure S2.4. Additional analysis of H3K27me3 ChIP-seq in ES cells.
a) CNN western blot of H3K27me3 from histone extracts, representative of 2 biological replicates. b) ChIP recovery before sequencing with spike-ins recapitulates the global gain of H3K27me3 in Usp9x-high ES cells. c) Usp9x-high ES cells carry more H3K27me3 over repetitive elements compared to untreated (no-auxin) cells. Each point represents an individual element, and hyper- or hypo-methylated elements were selected by setting a cutoff of $\log_2$(Usp9x-high/untreated) > |0.7|. d) Representative genome browser view of H3K27me3 coverage in Usp9x-high and Usp9x-low cells and the ratio of the two. Elevated H3K27me3 signal in Usp9x-high cells is often observed outside of promoters.

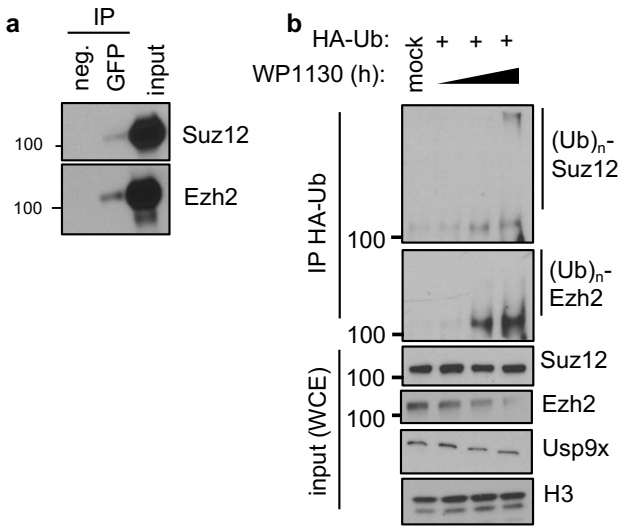

Figure S2.5. Additional validation of the Usp9x-PRC2 regulatory axis.
a) Co-IPs in AID-Usp9x cells. GFP = IP using GFP beads to isolate Usp9x. neg. = mock IP with negative control beads. b) Acute catalytic inhibition of Usp9x with the semi-selective inhibitor WP1130 leads to gain of ubiquitin at PRC2 proteins, similar to Fig. 4b. WP1130 treatment ranges from 0-4h.

Author Contributions

T.A.M. and M.R.-S. conceived of the project. T.A.M. designed, performed, and analyzed all experiments. E.P.N. generated stable *Tir1*-targeted mouse ES cells, provided the AID, and designed the cloning/targeting strategy, under the supervision of B. B. M.R.-S. supervised the project. T.A.M. wrote the manuscript.

Acknowledgments

We thank J. Lee and the Toronto Center for Phenogenomics for mouse support; E. Chow, K. Chan, and members of the UCSF Center for Advanced Technology and the LTRI Sequencing Core for assistance with sequencing; D. Goekbuget and K. Chan for assistance with sonication; J. Pearson for the HA-Ubiquitin plasmid; S. Biechele for cloning advice; and M. Percharde for guidance with bioinformatics. Flow cytometry and cell sorting data were generated in the UCSF Parnassus Flow Cytometry Core, supported by a Diabetes Research Center Grant and National Institutes of Health (NIH) grant P30 DK063720. This work was supported by NIH grant 1F30HD093116 (to T.A.M.). Research in the Santos lab is funded by a Canada 150 Research Chair in Developmental Epigenetics, Canadian Institutes of Health Research, Sinai Health Foundation and the Medicine by Design Program of the University of Toronto.

References

Abed, M., Verschueren, E., Budayeva, H., Liu, P., Kirkpatrick, D.S., Reja, R., Kummerfeld, S.K., Webster, J.D., Gierke, S., Reichelt, M., et al. (2019). The Gag protein PEG10 binds to RNA and regulates trophoblast stem cell lineage specification. PLoS ONE *14*, e0214110.

Akkers, R.C., van Heeringen, S.J., Jacobi, U.G., Janssen-Megens, E.M., FranCoijs, K.-J., Stunnenberg, H.G., and Veenstra, G.J.C. (2009). A Hierarchy of H3K4me3 and H3K27me3 Acquisition in Spatial Gene Regulation in Xenopus Embryos. Developmental Cell *17*, 425–434.

Ashburner, M., Ball, C.A., Blake, J.A., Botstein, D., Butler, H., Cherry, J.M., Davis, A.P., Dolinski, K., Dwight, S.S., Eppig, J.T., et al. (2000). Gene ontology: tool for the unification of biology. The Gene Ontology Consortium. Nat. Genet. *25*, 25–29.

Bailey, M.H., Tokheim, C., Porta-Pardo, E., Sengupta, S., Bertrand, D., Weerasinghe, A., Colaprico, A., Wendl, M.C., Kim, J., Reardon, B., et al. (2018). Comprehensive Characterization of Cancer Driver Genes and Mutations. Cell *173*, 371–385.e18.

Barry, C., Schmitz, M.T., Propson, N.E., Hou, Z., Zhang, J., Nguyen, B.K., Bolin, J.M., Jiang, P., McIntosh, B.E., Probasco, M.D., et al. (2017). Uniform neural tissue models produced on synthetic hydrogels using standard culture techniques. Exp. Biol. Med. (Maywood) *242*, 1679–1689.

Beccari, L., Moris, N., Girgin, M., Turner, D.A., Baillie-Johnson, P., Cossy, A.-C., Lutolf, M.P., Duboule, D., and Arias, A.M. (2018). Multi-axial self-organization properties of mouse embryonic stem cells into gastruloids. Nature 1–27.

Beddington, R.S. (1983). Histogenetic and neoplastic potential of different regions of the mouse embryonic egg cylinder. J Embryol Exp Morphol *75*, 189–204.

Blanpain, C., Lowry, W.E., Geoghegan, A., Polak, L., and Fuchs, E. (2004). Self-Renewal, Multipotency, and the Existence of Two Cell Populations within an Epithelial Stem Cell Niche. Cell *118*, 635–648.

Blaschke, K., Ebata, K.T., Karimi, M.M., Zepeda-Martínez, J.A., Goyal, P., Mahapatra, S., Tam, A., Laird, D.J., Hirst, M., Rao, A., et al. (2013). Vitamin C induces Tet-dependent DNA demethylation and a blastocyst-like state in ES cells. Nature *500*, 222–226.

Boroviak, T., Loos, R., Lombard, P., Okahara, J., Behr, R., Sasaki, E., Nichols, J., Smith, A., and Bertone, P. (2015). Lineage-Specific Profiling Delineates the Emergence and Progression of Naive Pluripotency in Mammalian Embryogenesis. Developmental Cell *35*, 366–382.

Boyer, L.A., Plath, K., Zeitlinger, J., Brambrink, T., Medeiros, L.A., Lee, T.I., Levine, S.S., Wernig, M., Tajonar, A., Ray, M.K., et al. (2006). Polycomb complexes repress developmental regulators in murine embryonic stem cells. Nature *441*, 349–353.

Bulut-Karslioglu, A., Biechele, S., Jin, H., Macrae, T.A., Hejna, M., Gertsenstein, M., Song, J.S., and Ramalho-Santos, M. (2016). Inhibition of mTOR induces a paused pluripotent state. Nature *540*, 119–123.

Bulut-Karslioglu, A., Macrae, T.A., Oses-Prieto, J.A., Covarrubias, S., Percharde, M., Ku, G., Diaz, A., McManus, M.T., Burlingame, A.L., and Ramalho-Santos, M. (2018). The Transcriptionally Permissive Chromatin State of Embryonic Stem Cells Is Acutely Tuned to Translational Output. Cell Stem Cell *22*, 369–383.e8.

Cai, C.-L., Liang, X., Shi, Y., Chu, P.-H., Pfaff, S.L., Chen, J., and Evans, S. (2003). Isl1 identifies a cardiac progenitor population that proliferates prior to differentiation and contributes a majority of cells to the heart. Developmental Cell *5*, 877–889.

Carelli, F.N., Sharma, G., and Ahringer, J. (2017). Broad Chromatin Domains: An Important Facet of Genome Regulation. Bioessays *39*, 1700124–1700127.

Chen, E.Y., Tan, C.M., Kou, Y., Duan, Q., Wang, Z., Meirelles, G.V., Clark, N.R., and Ma'ayan, A. (2013). Enrichr: interactive and collaborative HTML5 gene list enrichment analysis tool. BMC Bioinformatics *14*, 128–14.

Chen, T., and Dent, S.Y.R. (2014). Chromatin modifiers and remodellers: regulators of cellular differentiation. Nature Publishing Group *15*, 93–106.

Collinson, A., Collier, A.J., Morgan, N.P., Sienerth, A.R., Chandra, T., Andrews, S., and Rugg-Gunn, P.J. (2016). Deletion of the Polycomb-Group Protein EZH2 Leads to Compromised Self-Renewal and Differentiation Defects in Human Embryonic Stem Cells. CellReports *17*, 2700–2714.

Comet, I., Riising, E.M., Leblanc, B., and Helin, K. (2016). Maintaining cell identity: PRC2-mediated regulation of transcription and cancer. Nat. Rev. Cancer *16*, 803–810.

Cox, B.J., Vollmer, M., Tamplin, O., Lu, M., Biechele, S., Gertsenstein, M., van Campenhout, C., Floss, T., Kühn, R., Wurst, W., et al. (2010). Phenotypic annotation of the mouse X chromosome. Genome Res. *20*, 1154–1164.

Damjanov, I., Solter, D., and Škreb, N. (1971). Teratocarcinogenesis as related to the age of embryos grafted under the kidney capsule. W. Roux' Archiv F. Entwicklungsmechanik *167*, 288–290.

Deevy, O., and Bracken, A.P. (2019). PRC2 functions in development and congenital disorders. Development *146*, dev181354–13.

Dejosez, M., Levine, S.S., Frampton, G.M., Whyte, W.A., Stratton, S.A., Barton, M.C., Gunaratne, P.H., Young, R.A., and Zwaka, T.P. (2010). Ronin/Hcf-1 binds to a hyperconserved enhancer element and regulates genes involved in the growth of embryonic stem cells. Genes Dev. *24*, 1479–1484.

Erhardt, S., Su, I.-H., Schneider, R., Barton, S., Bannister, A.J., Perez-Burgos, L., Jenuwein, T., Kouzarides, T., Tarakhovsky, A., and Surani, M.A. (2003). Consequences of the depletion

of zygotic and embryonic enhancer of zeste 2 during preimplantation mouse development. Development *130*, 4235–4248.

Faust, C., Schumacher, A., Holdener, B., and Magnuson, T. (1995). The eed mutation disrupts anterior mesoderm production in mice. Development *121*, 273–285.

Ferrari, K.J., Scelfo, A., Jammula, S., Cuomo, A., Barozzi, I., Stützer, A., Fischle, W., Bonaldi, T., and Pasini, D. (2014). Polycomb-Dependent H3K27me1 and H3K27me2 Regulate Active Transcription and Enhancer Fidelity. Molecular Cell *53*, 49–62.

Fischer-Vize, J.A., Rubin, G.M., and Lehmann, R. (1992). The *fat facets* gene is required for *Drosophila* eye and embryo development. Development *116*, 985–1000.

Gao, Y., Liu, X., Bin Tang, Li, C., Kou, Z., Li, L., Liu, W., Wu, Y., Kou, X., Li, J., et al. (2017). Protein Expression Landscape of Mouse Embryos during Pre-implantation Development. Cell Reports *21*, 3957–3969.

Gaspar-Maia, A., Alajem, A., Polesso, F., Sridharan, R., Mason, M.J., Heidersbach, A., Ramalho-Santos, J., McManus, M.T., Plath, K., Meshorer, E., et al. (2009). Chd1 regulates open chromatin and pluripotency of embryonic stem cells. Nature *460*, 863–868.

Gökbuget, D., and Blelloch, R. (2019). Epigenetic control of transcriptional regulation in pluripotency and early differentiation. Development *146*, dev164772–16.

Gu, G., Wells, J.M., Dombkowski, D., Preffer, F., Aronow, B., and Melton, D.A. (2004). Global expression analysis of gene regulatory pathways during endocrine pancreatic development. Development *131*, 165–179.

Guzman-Ayala, M., Sachs, M., Koh, F.M., Onodera, C., Bulut-Karslioglu, A., Lin, C.J., Wong, P., Nitta, R., Song, J.S., and Ramalho-Santos, M. (2014). Chd1 is essential for the high transcriptional output and rapid growth of the mouse epiblast. Development *142*, 118–127.

Hackett, J.A., and Surani, M.A. (2014). Regulatory principles of pluripotency: from the ground state up. Cell Stem Cell *15*, 416–430.

Hawkins, R.D., Hon, G.C., Lee, L.K., Ngo, Q., Lister, R., Pelizzola, M., Edsall, L.E., Kuan, S., Luu, Y., Klugman, S., et al. (2010). Distinct epigenomic landscapes of pluripotent and lineage-committed human cells. Cell Stem Cell *6*, 479–491.

Hayashi, S., Lewis, P., Pevny, L., and McMahon, A.P. (2002). Efficient gene modulation in mouse epiblast using a Sox2Cre transgenic mouse strain. Mech. Dev. *119 Suppl 1*, S97–S101.

Homan, C.C., Kumar, R., Nguyen, L.S., Haan, E., Raymond, F.L., Abidi, F., Raynaud, M., Schwartz, C.E., Wood, S.A., Gecz, J., et al. (2014). Mutations in USP9X Are Associated with X-Linked Intellectual Disability and Disrupt Neuronal Cell Migration and Growth. The American Journal of Human Genetics *94*, 470–478.

Huang, D.W., Sherman, B.T., and Lempicki, R.A. (2009a). Systematic and integrative analysis of large gene lists using DAVID bioinformatics resources. Nat Protoc *4*, 44–57.

Huang, D.W., Sherman, B.T., and Lempicki, R.A. (2009b). Bioinformatics enrichment tools: paths toward the comprehensive functional analysis of large gene lists. Nucleic Acids Res. *37*, 1–13.

Højfeldt, J.W., Hedehus, L., Laugesen, A., Tatar, T., Wiehle, L., and Helin, K. (2019). Non-core Subunits of the PRC2 Complex Are Collectively Required for Its Target-Site Specificity. Molecular Cell 1–18.

Inoue, A., Jiang, L., Lu, F., Suzuki, T., and Zhang, Y. (2017). Maternal H3K27me3 controls DNA methylation-independent imprinting. Nature *547*, 419–424.

Israel, S., Ernst, M., Psathaki, O.E., Drexler, H.C.A., Casser, E., Suzuki, Y., Makalowski, W., Boiani, M., Fuellen, G., and Taher, L. (2019). An integrated genome-wide multi-omics analysis of gene expression dynamics in the preimplantation mouse embryo. Sci Rep *9*, 13356–15.

Jones, M.H., Furlong, R.A., Burkin, H., Chalmers, I.J., Brown, G.M., Khwaja, O., and Affara, N.A. (1996). The Drosophila developmental gene fat facets has a human homologue in

Xp11.4 which escapes X-inactivation and has related sequences on Yq11.2. Hum. Mol. Genet. *5*, 1695–1701.

Kalkan, T., Olova, N., Roode, M., Mulas, C., Lee, H.J., Nett, I., Marks, H., Walker, R., Stunnenberg, H.G., Lilley, K.S., et al. (2017). Tracking the embryonic stem cell transition from ground state pluripotency. Development *144*, 1221–1234.

Kent, W.J., Sugnet, C.W., Furey, T.S., Roskin, K.M., Pringle, T.H., Zahler, A.M., and Haussler, D. (2002). The human genome browser at UCSC. Genome Res. *12*, 996–1006.

Khan, O.M., Carvalho, J., Spencer-Dene, B., Mitter, R., Frith, D., Snijders, A.P., Wood, S.A., and Behrens, A. (2018). The deubiquitinase USP9X regulates FBW7 stability and suppresses colorectal cancer. J. Clin. Invest. *128*, 1326–1337.

Kim, D., Pertea, G., Trapnell, C., Pimentel, H., Kelley, R., and Salzberg, S.L. (2013). TopHat2: accurate alignment of transcriptomes in the presence of insertions, deletions and gene fusions. Genome Biol. *14*, R36–13.

Kojima, Y., Kaufman-Francis, K., Studdert, J.B., Steiner, K.A., Power, M.D., Loebel, D.A.F., Jones, V., Hor, A., de Alencastro, G., Logan, G.J., et al. (2014). The transcriptional and functional properties of mouse epiblast stem cells resemble the anterior primitive streak. Cell Stem Cell *14*, 107–120.

Kuleshov, M.V., Jones, M.R., Rouillard, A.D., Fernandez, N.F., Duan, Q., Wang, Z., Koplev, S., Jenkins, S.L., Jagodnik, K.M., Lachmann, A., et al. (2016). Enrichr: a comprehensive gene set enrichment analysis web server 2016 update. Nucleic Acids Res. *44*, W90–W97.

Kumar, B., and Elsässer, S.J. (2019). Quantitative Multiplexed ChIP Reveals Global Alterations that Shape Promoter Bivalency in Ground State Embryonic Stem Cells. CellReports *28*, 3274–3284.e3275.

Langmead, B., and Salzberg, S.L. (2012). Fast gapped-read alignment with Bowtie 2. Nat Meth *9*, 357–359.

Laugesen, A., Højfeldt, J.W., and Helin, K. (2019). Molecular Mechanisms Directing PRC2 Recruitment and H3K27 Methylation. Molecular Cell *74*, 8–18.

Lavarone, E., Barbieri, C.M., and Pasini, D. (2019). Dissecting the role of H3K27 acetylation and methylation in PRC2 mediated control of cellular identity. Nature Communications 1–16.

Law, C.W., Chen, Y., Shi, W., and Smyth, G.K. (2014). voom: precision weights unlock linear model analysis tools for RNA-seq read counts. Genome Biol. *15*, R29.

Lee, H.-G., Kahn, T.G., Simcox, A., Schwartz, Y.B., and Pirrotta, V. (2015). Genome-wide activities of Polycomb complexes control pervasive transcription. Genome Res. *25*, 1170–1181.

Leeb, M., Pasini, D., Novatchkova, M., Jaritz, M., Helin, K., and Wutz, A. (2010). Polycomb complexes act redundantly to repress genomic repeats and genes. Genes Dev. *24*, 265–276.

Li, H., Liefke, R., Jiang, J., Kurland, J.V., Tian, W., Deng, P., Zhang, W., He, Q., Patel, D.J., Bulyk, M.L., et al. (2017). Polycomb-like proteins link the PRC2 complex to CpG islands. Nature *549*, 287–291.

Li, H., Handsaker, B., Wysoker, A., Fennell, T., Ruan, J., Homer, N., Marth, G., Abecasis, G., and Durbin, R. (2009). The Sequence Alignment/Map format and SAMtools. Bioinformatics *25*, 2078–2079.

Liu, H., and Naismith, J.H. (2008). An efficient one-step site-directed deletion, insertion, single and multiple-site plasmid mutagenesis protocol. BMC Biotechnol. *8*, 91.

Liu, X., Wang, C., Liu, W., Li, J., Li, C., Kou, X., Chen, J., Zhao, Y., Gao, H., Wang, H., et al. (2016). Distinct features of H3K4me3 and H3K27me3 chromatin domains in pre-implantation embryos. Nature *537*, 558–562.

Macfarlan, T.S., Gifford, W.D., Driscoll, S., Lettieri, K., Rowe, H.M., Bonanomi, D., Firth, A., Singer, O., Trono, D., and Pfaff, S.L. (2012). Embryonic stem cell potency fluctuates with endogenous retrovirus activity. Nature *487*, 57–63.

Marks, H., Kalkan, T., Menafra, R., Denissov, S., Jones, K., Hofemeister, H., Nichols, J., Kranz, A., Stewart, A.F., Smith, A., et al. (2012). The Transcriptional and Epigenomic Foundations of Ground State Pluripotency. Cell *149*, 590–604.

Matoba, S., Wang, H., Jiang, L., Lu, F., Iwabuchi, K.A., Wu, X., Inoue, K., Yang, L., Press, W., Lee, J.T., et al. (2018). Loss of H3K27me3 Imprinting in Somatic Cell Nuclear Transfer Embryos Disrupts Post-Implantation Development. Cell Stem Cell *23*, 343–354.e345.

McCabe, M.T., Graves, A.P., Ganji, G., Diaz, E., Halsey, W.S., Jiang, Y., Smitheman, K.N., Ott, H.M., Pappalardi, M.B., Allen, K.E., et al. (2012). Mutation of A677 in histone methyltransferase EZH2 in human B-cell lymphoma promotes hypertrimethylation of histone H3 on lysine 27 (H3K27). Proc. Natl. Acad. Sci. U.S.a. *109*, 2989–2994.

Mendez, J., and Stillman, B. (2000). Chromatin association of human origin recognition complex, cdc6, and minichromosome maintenance proteins during the cell cycle: assembly of prereplication complexes in late mitosis. Molecular and Cellular Biology *20*, 8602–8612.

Mi, H., Muruganujan, A., Ebert, D., Huang, X., and Thomas, P.D. (2019). PANTHER version 14: more genomes, a new PANTHER GO-slim and improvements in enrichment analysis tools. Nucleic Acids Res. *47*, D419–D426.

Miro, X., Zhou, X., Boretius, S., Michaelis, T., Kubisch, C., Alvarez-Bolado, G., and Gruss, P. (2009). Haploinsufficiency of the murine polycomb gene Suz12 results in diverse malformations of the brain and neural tube. Disease Models & Mechanisms *2*, 412–418.

Mitiku, N., and Baker, J.C. (2007). Genomic Analysis of Gastrulation and Organogenesis in the Mouse. Developmental Cell *13*, 897–907.

Moody, J.D., Levy, S., Mathieu, J., Xing, Y., Kim, W., Dong, C., Tempel, W., Robitaille, A.M., Dang, L.T., Ferreccio, A., et al. (2017). First critical repressive H3K27me3 marks in embryonic stem cells identified using designed protein inhibitor. Proc. Natl. Acad. Sci. U.S.a. *114*, 10125–10130.

Murtaza, M., Jolly, L.A., Gecz, J., and Wood, S.A. (2015). La FAM fatale: USP9X in development and disease. Cellular and Molecular Life Sciences *72*, 2075–2089.

Nagai, H., Noguchi, T., Homma, K., Katagiri, K., Takeda, K., Matsuzawa, A., and Ichijo, H. (2009). Ubiquitin-like Sequence in ASK1 Plays Critical Roles in the Recognition and Stabilization by USP9X and Oxidative Stress-Induced Cell Death. Molecular Cell *36*, 805–818.

Naik, E., Webster, J.D., DeVoss, J., Liu, J., Suriben, R., and Dixit, V.M. (2014). Regulation of proximal T cell receptor signaling and tolerance induction by deubiquitinase Usp9X. J Exp Med *211*, 1947–1955.

Nishimura, K., Fukagawa, T., Takisawa, H., Kakimoto, T., and Kanemaki, M. (2009). An auxin-based degron system for the rapid depletion of proteins in nonplant cells. Nat Meth *6*, 917–922.

Nora, E.P., Goloborodko, A., Valton, A.-L., Gibcus, J.H., Uebersohn, A., Abdennur, N., Dekker, J., Mirny, L.A., and Bruneau, B.G. (2017). Targeted Degradation of CTCF Decouples Local Insulation of Chromosome Domains from Genomic Compartmentalization. Cell *169*, 930–933.e22.

O'Carroll, D., Erhardt, S., Pagani, M., Barton, S.C., Surani, M.A., and Jenuwein, T. (2001). The Polycomb-Group Gene Ezh2 Is Required for Early Mouse Development. Molecular and Cellular Biology *21*, 4330–4336.

Oksuz, O., Narendra, V., Lee, C.-H., Descostes, N., LeRoy, G., Raviram, R., Blumenberg, L., Karch, K., Rocha, P.P., Garcia, B.A., et al. (2018). Capturing the Onset of PRC2-Mediated Repressive Domain Formation. Molecular Cell *70*, 1149–1162.e5.

Paemka, L., Mahajan, V.B., Ehaideb, S.N., Skeie, J.M., Tan, M.C., Wu, S., Cox, A.J., Sowers, L.P., Gecz, J., Jolly, L., et al. (2015). Seizures are regulated by ubiquitin-specific peptidase 9 X-linked (USP9X), a de-ubiquitinase. PLoS Genet *11*, e1005022.

Pantaleon, M., Kanai-Azuma, M., Mattick, J.S., Kaibuchi, K., Kaye, P.L., and Wood, S.A. (2001). FAM deubiquitylating enzyme is essential for preimplantation mouse embryo development. Mech. Dev. *109*, 151–160.

Pasini, D., Bracken, A.P., Hansen, J.B., Capillo, M., and Helin, K. (2007). The Polycomb Group Protein Suz12 Is Required for Embryonic Stem Cell Differentiation. Molecular and Cellular Biology *27*, 3769–3779.

Pasini, D., Bracken, A.P., Jensen, M.R., Lazzerini Denchi, E., and Helin, K. (2004). Suz12 is essential for mouse development and for EZH2 histone methyltransferase activity. Embo J *23*, 4061–4071.

Pasini, D., Cloos, P.A.C., Walfridsson, J., Olsson, L., Bukowski, J.-P., Johansen, J.V., Bak, M., Tommerup, N., Rappsilber, J., and Helin, K. (2010a). JARID2 regulates binding of the Polycomb repressive complex 2 to target genes in ES cells. Nature *464*, 306–310.

Pasini, D., Malatesta, M., Jung, H.R., Walfridsson, J., Willer, A., Olsson, L., Skotte, J., Wutz, A., Porse, B., Jensen, O.N., et al. (2010b). Characterization of an antagonistic switch between histone H3 lysine 27 methylation and acetylation in the transcriptional regulation of Polycomb group target genes. Nucleic Acids Res. *38*, 4958–4969.

Pauler, F.M., Sloane, M.A., Huang, R., Regha, K., Koerner, M.V., Tamir, I., Sommer, A., Aszodi, A., Jenuwein, T., and Barlow, D.P. (2009). H3K27me3 forms BLOCs over silent genes and intergenic regions and specifies a histone banding pattern on a mouse autosomal chromosome. Genome Res. *19*, 221–233.

Percharde, M., Bulut-Karslioglu, A., and Ramalho-Santos, M. (2017a). Hypertranscription in Development, Stem Cells, and Regeneration. Developmental Cell *40*, 9–21.

Percharde, M., Wong, P., and Ramalho-Santos, M. (2017b). Global Hypertranscription in the Mouse Embryonic Germline. CellReports *19*, 1987–1996.

Perino, M., Mierlo, G., Karemaker, I.D., Genesen, S., Vermeulen, M., Marks, H., Heeringen, S.J., and Veenstra, G.J.C. (2018). MTF2 recruits Polycomb Repressive Complex 2 by helical-shape-selective DNA binding. Nat. Genet. 1–14.

Pérez-Mancera, P.A., Rust, A.G., van der Weyden, L., Kristiansen, G., Li, A., Sarver, A.L., Silverstein, K.A.T., Grützmann, R., Aust, D., Rümmele, P., et al. (2012). The deubiquitinase USP9X suppresses pancreatic ductal adenocarcinoma. Nature *486*, 266–270.

Premarathne, S., Murtaza, M., Matigian, N., Jolly, L.A., and Wood, S.A. (2017). Loss of Usp9x disrupts cell adhesion, and components of the Wnt and Notch signaling pathways in neural progenitors. Sci Rep *7*, 8109–8118.

Quinlan, A.R., and Hall, I.M. (2010). BEDTools: a flexible suite of utilities for comparing genomic features. Bioinformatics *26*, 841–842.

Ramalho-Santos, M., Yoon, S., Matsuzaki, Y., Mulligan, R.C., and Melton, D.A. (2002). "Stemness": transcriptional profiling of embryonic and adult stem cells. Science *298*, 597–600.

Ramírez, F., Dündar, F., Diehl, S., Grüning, B.A., and Manke, T. (2014). deepTools: a flexible platform for exploring deep-sequencing data. Nucleic Acids Res. *42*, W187–W191.

Ran, F.A., Hsu, P.D., Wright, J., Agarwala, V., Scott, D.A., and Zhang, F. (2013). Genome engineering using the CRISPR-Cas9 system. Nat Protoc *8*, 2281–2308.

Reijnders, M.R.F., Zachariadis, V., Latour, B., Jolly, L., Mancini, G.M., Pfundt, R., Wu, K.M., van Ravenswaaij-Arts, C.M.A., Veenstra-Knol, H.E., Anderlid, B.-M.M., et al. (2016). De Novo Loss-of-Function Mutations in USP9X Cause a Female-Specific Recognizable Syndrome with Developmental Delay and Congenital Malformations. The American Journal of Human Genetics *98*, 373–381.

Reverón-Gómez, N., González-Aguilera, C., Stewart-Morgan, K.R., Petryk, N., Flury, V., Graziano, S., Johansen, J.V., Jakobsen, J.S., Alabert, C., and Groth, A. (2018). Accurate

Recycling of Parental Histones Reproduces the Histone Modification Landscape during DNA Replication. Molecular Cell *72*, 239–249.e5.

Rott, R., Szargel, R., Haskin, J., Bandopadhyay, R., Lees, A.J., Shani, V., and Engelender, S. (2011). α-Synuclein fate is determined by USP9X-regulated monoubiquitination. Proc. Natl. Acad. Sci. U.S.a. *108*, 18666–18671.

Rougeot, J., Chrispijn, N.D., Aben, M., Elurbe, D.M., Andralojc, K.M., Murphy, P.J., Jansen, P.W.T.C., Vermeulen, M., Cairns, B.R., and Kamminga, L.M. (2019). Maintenance of spatial gene expression by Polycomb-mediated repression after formation of a vertebrate body plan. Development *146*, dev178590–14.

Rugg-Gunn, P.J., Cox, B.J., Ralston, A., and Rossant, J. (2010). Distinct histone modifications in stem cell lines and tissue lineages from the early mouse embryo. Proc. Natl. Acad. Sci. U.S.a. *107*, 10783–10790.

Saha, B., Home, P., Ray, S., Larson, M., Paul, A., Rajendran, G., Behr, B., and Paul, S. (2013). EED and KDM6B coordinate the first mammalian cell lineage commitment to ensure embryo implantation. Molecular and Cellular Biology *33*, 2691–2705.

Schmitges, F.W., Prusty, A.B., Faty, M., Stützer, A., Lingaraju, G.M., Aiwazian, J., Sack, R., Hess, D., Li, L., Zhou, S., et al. (2011). Histone methylation by PRC2 is inhibited by active chromatin marks. Molecular Cell *42*, 330–341.

Schwickart, M., Huang, X., Lill, J.R., Liu, J., Ferrando, R., French, D.M., Maecker, H., O'Rourke, K., Bazan, F., Eastham-Anderson, J., et al. (2010). Deubiquitinase USP9X stabilizes MCL1 and promotes tumour cell survival. Nature *463*, 103–107.

Seiler, C.Y., Park, J.G., Sharma, A., Hunter, P., Surapaneni, P., Sedillo, C., Field, J., Algar, R., Price, A., Steel, J., et al. (2014). DNASU plasmid and PSI:Biology-Materials repositories: resources to accelerate biological research. Nucleic Acids Res. *42*, D1253–D1260.

Shan, Y., Liang, Z., Xing, Q., Zhang, T., Wang, B., Tian, S., Huang, W., Zhang, Y., Yao, J., Zhu, Y., et al. (2017). PRC2 specifies ectoderm lineages and maintains pluripotency in primed but not naïve ESCs. Nature Communications 1–14.

Shechter, D., Nicklay, J.J., Chitta, R.K., Shabanowitz, J., Hunt, D.F., and Allis, C.D. (2009). Analysis of histones in Xenopus laevis. I. A distinct index of enriched variants and modifications exists in each cell type and is remodeled during developmental transitions. Journal of Biological Chemistry *284*, 1064–1074.

Sneeringer, C.J., Scott, M.P., the, K.K.P.O., 2010 Coordinated activities of wild-type plus mutant EZH2 drive tumor-associated hypertrimethylation of lysine 27 on histone H3 (H3K27) in human B-cell lymphomas. National Acad Sciences.

Snow, M.H.L. (1977). Gastrulation in the mouse: Growth and regionalization of the epiblast. Development *42*, 293–303.

Stovner, E.B., and Sætrom, P. (2019). epic2 efficiently finds diffuse domains in ChIP-seq data. Bioinformatics *35*, 4392–4393.

Subramanian, A., Tamayo, P., Mootha, V.K., Mukherjee, S., Ebert, B.L., Gillette, M.A., Paulovich, A., Pomeroy, S.L., Golub, T.R., Lander, E.S., et al. (2005). Gene set enrichment analysis: A knowledge-based approach for interpreting genome-wide expression profiles. Proc Natl Acad Sci USA *102*, 15545.

Tarpey, P.S., Smith, R., Pleasance, E., Whibley, A., Edkins, S., Hardy, C., O'Meara, S., Latimer, C., Dicks, E., Menzies, A., et al. (2009). A systematic, large-scale resequencing screen of X-chromosome coding exons in mental retardation. Nat. Genet. *41*, 535–543.

The Gene Ontology Consortium (2019). The Gene Ontology Resource: 20 years and still GOing strong. Nucleic Acids Res. *47*, D330–D338.

Thornton, S.R., Butty, V.L., Levine, S.S., and Boyer, L.A. (2014). Polycomb Repressive Complex 2 Regulates Lineage Fidelity during Embryonic Stem Cell Differentiation. PLoS ONE *9*, e110498–14.

Thorvaldsdóttir, H., Robinson, J.T., and Mesirov, J.P. (2013). Integrative Genomics Viewer (IGV): high-performance genomics data visualization and exploration. Brief. Bioinformatics *14*, 178–192.

van Mierlo, G., Dirks, R.A.M., De Clerck, L., Brinkman, A.B., Huth, M., Kloet, S.L., Saksouk, N., Kroeze, L.I., Willems, S., Farlik, M., et al. (2019). Integrative Proteomic Profiling Reveals PRC2-Dependent Epigenetic Crosstalk Maintains Ground-State Pluripotency. Cell Stem Cell *24*, 123–137.e128.

Walter, M., Teissandier, A., Pérez-Palacios, R., and Bourc'his, D. (2016). An epigenetic switch ensures transposon repression upon dynamic loss of DNA methylation in embryonic stem cells. Elife *5*, R87.

Wamstad, J.A., Alexander, J.M., Truty, R.M., Shrikumar, A., Li, F., Eilertson, K.E., Ding, H., Wylie, J.N., Pico, A.R., Capra, J.A., et al. (2012). Dynamic and coordinated epigenetic regulation of developmental transitions in the cardiac lineage. Cell *151*, 206–220.

Wang, C., Liu, X., Gao, Y., Yang, L., Li, C., Liu, W., Chen, C., Kou, X., Zhao, Y., Chen, J., et al. (2018). Reprogramming of H3K9me3-dependent heterochromatin during mammalian embryo development. Nat Cell Biol 1–23.

Wang, S.-P., Tang, Z., Chen, C.-W., Shimada, M., Koche, R.P., Wang, L.-H., Nakadai, T., Chramiec, A., Krivtsov, A.V., Armstrong, S.A., et al. (2017). A UTX-MLL4-p300 Transcriptional Regulatory Network Coordinately Shapes Active Enhancer Landscapes for Eliciting Transcription. Molecular Cell *67*, 308–321.e6.

Wood, S.A., Pascoe, W.S., Ru, K., Yamada, T., Hirchenhain, J., Kemler, R., and Mattick, J.S. (1997). Cloning and expression analysis of a novel mouse gene with sequence similarity to the Drosophila fat facets gene. Mech. Dev. *63*, 29–38.

Yang, X., Hu, B., Liao, J., Qiao, Y., Chen, Y., Qian, Y., Feng, S., Yu, F., Dong, J., Hou, Y., et al. (2019). Distinct enhancer signatures in the mouse gastrula delineate progressive cell fate continuum during embryo development. Cell Res 1–16.

Yap, D.B., Chu, J., Berg, T., Schapira, M., Cheng, S.W.G., Moradian, A., Morin, R.D., Mungall, A.J., Meissner, B., Boyle, M., et al. (2011). Somatic mutations at EZH2 Y641 act dominantly through a mechanism of selectively altered PRC2 catalytic activity, to increase H3K27 trimethylation. Blood *117*, 2451–2459.

Young, M.D., Willson, T.A., Wakefield, M.J., Trounson, E., Hilton, D.J., Blewitt, M.E., Oshlack, A., and Majewski, I.J. (2011). ChIP-seq analysis reveals distinct H3K27me3 profiles that correlate with transcriptional activity. Nucleic Acids Res. *39*, 7415–7427.

Zhang, M., Wang, F., Kou, Z., Zhang, Y., and Gao, S. (2009). Defective chromatin structure in somatic cell cloned mouse embryos. J. Biol. Chem. *284*, 24981–24987.

Zhang, Y., Liu, T., Meyer, C.A., Eeckhoute, J., Johnson, D.S., Bernstein, B.E., Nusbaum, C., Myers, R.M., Brown, M., Li, W., et al. (2008). Model-based analysis of ChIP-Seq (MACS). Genome Biol. *9*, R137–R139.

Zhang, Y., Xiang, Y., Yin, Q., Du, Z., Peng, X., Wang, Q., Fidalgo, M., Xia, W., Li, Y., Zhao, Z.-A., et al. (2018). Dynamic epigenomic landscapes during early lineage specification in mouse embryos. Nat. Genet. *50*, 96–105.

Zheng, H., Huang, B., Zhang, B., Xiang, Y., Du, Z., Xu, Q., Li, Y., Wang, Q., Ma, J., Peng, X., et al. (2016). Resetting Epigenetic Memory by Reprogramming of Histone Modifications in Mammals. Molecular Cell *63*, 1066–1079.

Materials and Methods

Mice

Usp9x$^{fl/fl}$ females were maintained as homozygotes on a C57BL/6 background by crossing *Usp9x*$^{fl/fl}$ and *Usp9x*$^{fl/Y}$ mice (Naik et al., 2014). Heterozygous male *Sox2-Cre* mice were obtained from Jackson Laboratories (JAX stock #008454) and bred with Cre-negative females to maintain a stock of heterozygous males (Hayashi et al., 2002). All mice were maintained on 12h light/dark cycle and provided with food and water *ad libitum* in individually ventilated units (Techniplast) in specific pathogen-free facilities at The Center for Phenogenomics, Toronto. All procedures involving animals were performed according to the Animals for Research Act of Ontario and the Guidelines of the Canadian Council on Animal Care. Animal Care Committee reviewed and approved all procedures conducted on animals at TCP (Protocol 22-0331). Sample size choice was not pre-determined. Genotyping primers:
TGCTGTCTTAAATGCATTTATTAATGGAG (Usp9x-fwd),
GTAAACAGTATTTGAAGTAGGCAAGAG (Usp9x-rev).

Yolk sacs were dissected from embryos and used for DNA extraction with the Sigma Red Extract-N-Amp kit (Sigma). Usp9x status was assessed by PCR amplification using Phire Green Hot Start II PCR Master Mix (Thermo Fisher Scientific). Cycling conditions: 98C for 30 sec; 35 cycles of 98C for 5 sec, 58C for 5 sec, 72C for 8 sec; 72C for 1 min.

Plasmid construction

The sgRNA was designed to target the *Usp9x* ATG with 20 nt overhang in both directions. Cloning was performed by annealing pairs of oligos into pSpCas9(BB)-2A-GFP (PX458) (modified from GFP to BFP by site directed mutagenesis), a gift from Feng Zhang (Addgene

plasmid # 48138 ; http://n2t.net/addgene:48138 ; RRID:Addgene_48138) (Ran et al., 2013). Plasmid identity was verified by Sanger sequencing and purified by midiprep (Qiagen).

The eGFP-AID-Usp9x plasmid was assembled from pEN244-CTCF-AID[71-114]-eGFP-FRT-Blast-FRT targeting construct, a gift from Benoit Bruneau (Addgene plasmid # 92140; http://n2t.net/addgene:92140 ; RRID:Addgene_92140) (Nora et al., 2017). The vector was digested with NruI, NsiI, and XhoI and gel purified to remove regions of *CTCF* homology (Qiagen Gel Extraction kit). ~900 bp homology arms to the *Usp9x* N-terminus were amplified from mouse genomic DNA using PrimeStar GXL polymerase (Takara) and Gibson assembly primers with 21 nucleotide overlap to adjacent fragments. The vector fragments and amplified homology arms were assembled by Gibson Assembly (NEB HiFi Assembly Kit).

Oligos containing a 3xFLAG sequence were annealed by incubation in annealing buffer (1x: 10 mM Tris-HCl pH 7.5, 1 mM EDTA, 50 mM NaCl) for 5 min at 95C followed by slow cooling to 25C. The annealed fragment was then digested with BamHI and XhoI and cleaned up by PCR purification (Qiagen MinElute). The eGFP-AID-Usp9x vector was also digested with BamHI/XhoI and cleaned up by gel extraction (Qiagen). The 3xFlag sequence was then ligated into the digested eGFP-Usp9x plasmid (Takara DNA ligation kit #6023).

ES cell targeting

Vectors were amplified by transformation into Stbl3 competent cells (Invitrogen). Resultant colonies were picked for miniprep DNA extraction (Qiagen) and screening by restriction enzyme digest. Positive clones were verified by Sanger sequencing, purified by Maxiprep column extraction (Qiagen Maxiprep) and then concentrated by standard ethanol precipitation overnight, and used for nucleofection.

5 million OsTir1 cells (Nora et al., 2017) (passage 4) were nucleofected with 2.5ug of the sgRNA plasmid and 20 ug of either eGFP-AID-Usp9x plasmid or eGFP-3xFLAG-Usp9x plasmid, using an Amaxa Nucleofector 2b device and ES nucleofection kit (Lonza) per the manufacturer's instructions. Cells were diluted in 500 ul of medium and immediately plated onto 10 cm dishes with 10 ml pre-warmed medium. After 2 days, GFP-single and BFP-/GFP-double-positive cells were sorted by FACS and plated at clonal density (10,000 cells per 10cm dish). Clones were left to expand for 5 days before manual picking onto 96well plates. Single clones were then dissociated and expanded for 2 days. Clones were screened for auxin responsiveness by replica plating onto 2 96w plates, addition of auxin to 1 plate, and measurement of eGFP fluorescence intensity by flow cytometry. After 8 hours, 10/48 picked AID clones displayed high eGFP expression as well as visible response to auxin, although the maximum response was ~50%. These 10 clones were subsequently expanded and used for all analyses shown. Cells were periodically passaged in the presence of puromycin (1 ug/ml) to select against spontaneous transgene silencing.

Usp9x-CD-mCherry cloning

The Usp9x catalytic domain was amplified from a plasmid containing the full-length Usp9x ORF, obtained from DNASU (Seiler et al., 2014), mCherry was amplified by PCR from a pcDNA3-mCherry plasmid. We then cloned the purified Usp9x-DUB and mCherry fragments into pEF1a-IRES-Neo was a gift from Thomas Zwaka (Addgene plasmid # 28019 ; http://n2t.net/addgene:28019 ; RRID:Addgene_28019) by Gibson Assembly and confirmed successful integration by Sanger sequencing (Dejosez et al., 2010). To make the C1566S catalytic mutant form of the Usp9x DUB domain, we performed site directed mutagenesis (Liu and Naismith, 2008). PCR with Phusion polymerase (NEB), with the PCR cycling conditions: 98C for 7 min; 12 cycles of 98C for 30s, 61C for 30s, 72C for 3 min 45s; 3 cycles of 98C for 30s,

56C for 30s, 72C for 3m 45s; 72C for 10 min; hold. The PCR product was digested with DpnI for 3h at 37C (NEB) and then 5 ul was transformed into Stbl3 competent cells (Thermo Fisher).

Mouse embryonic stem cell culture

ES cells were passaged every 1-2 days and grown in regular serum ES cell medium: ES-FBS cells were cultured in DMEM GlutaMAX with Na Pyruvate, 15% fetal bovine serum (Atlanta Biologicals), 0.1 mM Non-essential amino acids, 50 U/ml Penicillin/Streptomycin, 0.1 mM EmbryoMax 2-Mercaptoethanol and 2000 U/ml ESGRO supplement. Cells tested negative for Mycoplasma contamination.

Indole-3-acetic acid sodium salt (Sigma I5148-2G) was dissolved in water to 500 mM, filter sterilized, and frozen in aliquots. These stock solutions were thawed diluted to 500 uM for all depletion experiments. Prior to experiments, cells were pulsed with puromycin (1 ug/ml) to select for optimal Os*Tir1* expression.

Colony formation assays

1000 cells from the indicated conditions were sorted and plated onto a 12-well plate. Cells were grown in self-renewing conditions (serum/LIF) for 5-6 days. Colonies were then washed 1x in PBS, fixed for 15 minutes at RT in 4% PFA, and stained according to the instructions of the VectorRed Alkaline Phosphatase (AP) Substrate Kit (Vector Laboratories). Colonies were manually scored on the basis of colony morphology and AP positivity (>50% of colony area).

qRT-PCR

cDNA synthesis was performed with the High-Capacity cDNA Reverse Transcription Kit (Thermo), using random hexamer priming for 2 hours at 37C. KAPA 2x SYBR Green Master

Mix, low ROX (KAPA) was used for qPCR and data were acquired on a QuantStudio 5 (Thermo) and analyzed in GraphPad Prism v8.

RNA-seq library preparation

3 clonal replicates of each cell line (AID-Usp9x or Flag-Usp9x) were used for RNA-sequencing. Cells were plated the day before sorting, and auxin was added to a final concentration of 500 uM in fresh media for 8h. Cells were trypsinized and resuspended in FACS buffer (10% FBS, PBS, ± 500 uM auxin) with SYTOX Blue for sorting. 250,000 cells from each condition were sorted on the basis of negative SYTOX Blue (Thermo) incorporation. 8h sorted cells were immediately pelleted, resuspended in Buffer RLT (Qiagen), snap frozen on dry ice, and stored at -80˚C before library preparation. Cells for the 2 day recovery were plated in regular ES-FBS medium and cultured for 48h in serum/LIF without auxin. They were sorted and stored in the same way. Sorts were performed on a Sony SH800 Single Cell Sorter (Sony).

RNA extractions from frozen lysates were performed on the same day using RNeasy Mini columns (Qiagen). Recovered total RNA was quantified by Qubit and quality assessed using an Agilent Bioanalyzer, RNA pico kit (Agilent). Synthetic RNAs from the External RNAs Control Consortium (ERCC) were spiked in at known concentrations to the same volume of RNA from the previous step, and 1 ug of total RNA was used for mRNA isolation and library preparation using the NEBNext Ultra II Directional Library Prep Kit for Illumina with the mRNA isolation module, per manufacturer's instructions (NEB #E7420S and #XXX). Library quality was assessed by Bioanalyzer High Sensitivity DNA chip (Agilent). Libraries were quantified by Qubit and pooled at equimolar concentration. Sequencing was performed on a HiSeq 4000 with 50 bp single-end reads (Illumina) at the UCSF Center for Advanced Technology.

For embryo RNA-seq, whole E8.5 embryos were dissected, cleaned of extraembryonic tissue, and then resuspended in buffer RLT + beta-mercaptoethanol, and snap frozen on dry ice. RNA was extracted as above, and 600 ng of total RNA was used for library preparation using the NEBNext Ultra II Directional Library Prep Kit for Illumina with the mRNA isolation module and NEBNext Multiplex Oligos for Illumina. DNA quality was assessed by Fragment Analyzer NGS. Libraries were quantified by Qubit and pooled at equimolar concentration for sequencing on a NextSeq 500, 75 bp single-end reads (Illumina) at the LTRI Sequencing Core.

RNA-seq analysis

Libraries were trimmed of Illumina adaptor sequences and quality-checked using trim_galore (Babraham Bioinformatics), and then aligned to mm10 with ERCC sequences using TopHat2 (options -g 20 --no-coverage-search --library-type fr-firststrand –no-novel-indels) (Kim et al., 2013). Gene counts were obtained from featureCounts on the command line with options: -t exon -T 8 -s 2 -g gene_id. The table of raw counts was imported into R, filtered to remove low-count genes (genes with 0 counts in any sample and those with ≤ 3 counts per million, CPM by edgeR, across all samples were filtered out), and separated into ERCC and gene counts. Values for spike-in normalization were determined from ERCC counts corrected for overall library size using edgeR calcNormFactors (nf <- calcNormFactors(raw_ercc_counts, lib.size=N), where N <- colSums(raw_gene_counts). The CNN factors were then used to adjust gene counts using the limma-voom transformation (option lib.size = N*nf) (Law et al., 2014). Data were further analyzed and plotted using ggplot2. The threshold for significant differential expression was adjusted p-value < 0.05 and log2FC > 0.7.

For *Usp9x*-mutant embryo RNA-seq, gene counts were obtained in the same manner, imported into R, and converted to a DESeq2 object (DESeqDataSetFromMatrix using sample information) for processing, DESeq2 1.24.0. Genes with fewer than 10 counts across all

samples were filtered out before differential expression analysis. rlog-normalized counts (DESeq2) were used for PCA and heatmaps of gene expression. Raw counts were used for differential expression analysis using the default parameters of the DEseq function.

To obtain counts from developing post-implantation embryos, published RNA-seq data from post-occipital embryos E6.5-E8.5 (Beccari et al., 2018) were downloaded from GEO and processed. The output of featureCounts was imported into R, filtered to remove low-expressed genes (≤ 10 counts across samples), and then normalized using DESeq2 estimateSizeFactors. Normalized counts were obtained from the output of counts (option normalized = TRUE).

Gene Ontology analyses

Pathway analysis was performed by Gene Ontology (GO) analysis using DAVID 6.8 and geneontology.org (Ashburner et al., 2000; Huang et al., 2009b; 2009a; Mi et al., 2019; The Gene Ontology Consortium, 2019). Transcription factor binding enrichment was determined using the Enrichr suite (https://amp.pharm.mssm.edu/Enrichr/) (Chen et al., 2013; Kuleshov et al., 2016). Lists of differentially-expressed genes were analyzed by ChEA. Tables of enriched factors and P-values were downloaded and plotted in R.

Gene Set Enrichment Analysis (GSEA v6.0.12) was performed with default conditions using the online GSEAPreranked tool online to compare differential expression (all genes sorted by log2FC) with gene sets from various published datasets as outlined below (Subramanian et al., 2005). Normalized enrichment scores were plotted in GraphPad Prism v8.

Datasets used for GSEA

The 2-cell embryo signature is from Macfarlan et al. (Macfarlan et al., 2012). Transcriptional signatures from cleavage stages through E5.5 were retrieved from the same source (Boroviak

et al., 2015), taking either the full gene list or the top 500 genes enriched for a particular time point from the published stage-specific expression analysis. The E6.5 epiblast signature was defined as genes differentially expressed in E6.5 epiblast relative to visceral endoderm and endoderm at the same stage (Zhang et al., 2018). A signature of early mesoderm was determined from published RNA-seq of ES cell differentiation, and we selected genes by fold-change of expression at the mesoderm stage compared to ES cells (Wamstad et al., 2012). The endoderm signature comes from published microarray data of early endoderm in E7.5 embryos (Gu et al., 2004). Neuroectoderm genes were defined by RNA-seq data of epiblast stem cell differentiation to neural fate, comparing the fold-change in expression at day 2 of differentiation relative to baseline (Barry et al., 2017). In all cases, either the full published gene list or the top 500 genes ranked by fold-change were used for GSEA.

Histone extraction

Histone extraction was performed based on a standard acid extraction protocol (Shechter et al., 2009). Briefly, sorted cells were lysed for 10 min at 4C in triton extraction buffer (PBS with 0.5% Triton X-100, 2 mM PMSF, 1x Halt Protease Inhibitor at a density of 10^7 cells/ml). Lysates were spun for 10 min at 4C, 2000 rpm. The pellet was washed once in 0.5x volume of lysis buffer and centrifuged again. Pellets were resuspended in 0.2 N HCl (10^6 cells/ml) and acid extracted overnight, rotating at 4C. The solution was clarified by centrifugation and the supernatant transferred to a new tube. Histones were precipitated in 0.25x volume TCA, incubated 20 minutes on ice, and pelleted at max speed for 10 min. Excess acid was removed from solution through two washes in ice-cold acetone, pellets were air-dried, and then histones were resuspended in water before BCA Protein quantification (Pierce). LDS sample buffer (Thermo Fisher) was added to 1x and samples were denatured for 5 min at 95C followed by cold shock.

Co-immunoprecipitations

Co-immunoprecipitation (Co-IP) assays were performed on nuclear extracts. ES cells grown to confluency were washed twice and then scraped in cold PBS. Cell pellets were weighed and resuspended in 4x volume of swelling buffer A (10 mM HEPES pH 7.9, 5 mM $MgCl_2$, 0.25 M Sucrose, 0.1% NP-40) with protease inhibitors were added fresh (1x Halt Protease inhibitors, 1 mM PMSF, 1 mM NaF, 10 mM N-ethylmaleimide (Sigma)). Lysates were incubated on ice for 20 min and passed through a 18 ½ G needle five times. Nuclei were pelleted by centrifuged for 10 min at 1500 *g* and lysed in 8x volume buffer B (10 mM HEPES pH 7.9, 1 mM $MgCl_2$, 0.1 mM EDTA, 25% glycerol, 0.5% Triton X-100, 0.5 M NaCl with PIs as in buffer A). After incubation on ice for 10 min, samples were passed through an 18 ½ G needle 5 times and pulse sonicated, 2 times 5 seconds at 4C. 100 ul of lysate was diluted in 400 ul IP wash/dilution buffer (150 mM NaCl, 10 mM Tris pH 8, 0.5% sodium deoxycholate, 1% Triton X-100, 1 mM EDTA, 1 mM EGTA) and rotated 4h-overnight with 1 ug Rb anti-Usp9x (Bethyl), 1.7 ug Rb anti-Ezh2 (CST #), or 1.7 ug Rb anti-IgG (Millipore CS200581). Input samples were collected at this time. Immune complexes were bound by 25 ul of pre-washed Protein A Dynabeads (Thermo), rotating end-over-end for 2h at 4C. Beads were washed in IP wash/dilution buffer, 3x5 min at 4C. Input and IP samples were eluted and denatured by boiling in 2x Laemmli buffer/bME for 10 min at 95C.

Co-IPs were also performed using Flag M2-bound magnetic agarose beads (Sigma) and GFP-Trap beads (ChromoTek). For Flag pull-downs, AID-Usp9x ES cell were used as controls for nonspecific binding to the Flag beads. For GFP pull-downs, the same amount of lysate was added to negative beads (ChromoTek) to control for nonspecific binding to beads. Cells were collected as above but diluted into GFP-Trap dilution buffer (10 mM Tris-HCl pH 7.5, 150 mM NaCl, 0.5 mM EDTA), immunoprecipitated by rotating for 1.5h at 4C, and washed by 3x fast washes in GFP-Trap dilution buffer. Input and IP samples were denatured as above.

HA-Ubiquitin Immunoprecipitations

HA-tagged ubiquitin was overexpressed in ES cells by transfection with Lipofectamine 2000 (Thermo Fisher Scientific), 500 ng per ~$8x10^6$ cells in a 10 cm dish. Water diluted in Lipofectamine was used for mock transfections. Medium was changed the next morning and cells were harvested after 24 hours. Adherent cells were washed twice and then scraped into cold PBS. The resulting cell pellets were weighed and resuspended in 4x volume of RIPA buffer (150 mM NaCl, 1% NP-40, 0.5% Na deoxycholate, 0.1% SDS, 50 mM Tris pH 8) to lyse for 15 min on ice. Pellets were centrifuged at max speed for 10 min, 4C, to remove insoluble material. 100 ul of supernatant was taken for IP and diluted to 500 ul in non-denaturing lysis buffer (20 mM Tris pH 8, 137 mM NaCl, 1% Triton X-100, 2 mM EDTA) plus 2.5 ug of anti-HA antibody (Abcam ab1190). IPs were incubated overnight at 4C with end-over-end rotation, and the next day immune complexes were then to 25 ul Protein A Dynabeads (Thermo Fisher Scientific) by rotating 2h at 4C. Complex were washed on beads for 3x10 min in IP wash buffer (150 mM NaCl, 10 mM Tris pH 8, 0.5% Na deoxycholate, 1% Triton X-100, 1 mM EDTA, 1 mM EGTA) and then eluted in 2x Laemmli buffer/10% β-mercaptoethanol followed by 10 min at 95C and cold shock on ice. Input samples were collected and denatured in Laemmli buffer to 1x. Samples were removed from beads for western blotting.

For Usp9x catalytic domain expressions, transfections were performed as above but with the addition of 2.5 µg of plasmid (wild-type or C1566S pEF1a-Usp9x_CD-mCherry) and in medium without Pen/Strep. Transfection was checked by mCherry fluorescence the next morning. IPs were performed as above but with the following antibodies instead of HA: Ezh2 at 1:300 (CST #5246), Suz12 at 1:50 (CST #3737), or rabbit IgG at 1:50 (Millipore CS200581).

Subcellular fractionation

Subcellular fractionation was performed as previously reported (Mendez and Stillman, 2000). Cell pellets were resuspended in buffer A (10 mM HEPES pH 7.9, 10 mM KCl, 1.5 mM $MgCl_2$, 0.34M sucrose, 10% glycerol, 0.1% Triton X-100, 1 mM DTT, and PIs: NaF, PMSF, 1x Halt Protease inhibitor cocktail); incubated 5 min on ice; and then centrifuged for 5 min at 1300 *g*, 4C. The supernatant was taken as the cytoplasmic extract and clarified by centrifugation at max speed. Nuclear pellets were washed in buffer A and then resuspended in buffer B (3 mM EDTA, 0.2 mM EGTA, 1 mM DTT, and PIs). After 5 min on ice, chromatin pellets were centrifuged for 5 min at 1700 *g*, 4C. The supernatant was collected as the soluble nucleoplasmic fraction. Insoluble pellets were resuspended in 1x Laemmli buffer containing 5% beta-mercaptoethanol and sonicated on a Bioruptor: high power, 30s on, 30s off, 5 min total (Diagenode).

Western blot analysis

Whole-cell protein lysates were prepared as indicated elsewhere. In general, WBs were performed cell-number normalized. Denatured samples were separated on 4-15% Mini-Protean TGX SDS-PAGE gels (Bio-rad). Most WBs were performed CNN, meaning that protein from the same number of cells was loaded on a gel. Wherever possible, extractions in each experiment were performed from the same number of cells. Protein was transferred to methanol-activated PVDF membranes (Bio-rad) by wet transfer (1x Pierce Transfer Buffer, 10% methanol) or using high molecular weight transfer conditions for the Bio-rad TransBlot Turbo (Bio-rad). Membranes were blocked in 5% milk/TBS-T and then incubated with indicated antibodies. Primary antibody incubation was performed for 1.5h at room temperature or overnight at 4C. Membranes were then washed and incubated with HRP-conjugated anti-mouse/rabbit secondary antibodies (Jackson Labs) for 1h at room temperature. Proteins were detected by ECL (Pierce) or Clarity (Bio-rad) detection reagents and exposure to X-ray film (Pierce).

H3K27me3 ChIP-seq

Two biological replicates, consisting of clonal replicates of AID-Usp9x collected on consecutive days, were collected. 10^6 cells were sorted and cross-linked in 1% formaldehyde/PBS, rotating for 10 min at room temperature. Cross-links were quenched with glycine (125 mM) for 5 min at room temperature. Samples were spun down at max speed, 4˚C, to pellet out insoluble material, and snap frozen. All subsequent steps were performed on ice or at 4˚C. Fixed cell pellets were thawed, 1% SDS, 10 mM EDTA, 50 mM Tris-HCl pH 8 with protease inhibitors (1x Halt PI, 1 mM PMSF, 1 mM NaF), and lysed for 30 min at 4C. Chromatin was sheared to 200-500 bp fragments on a Covaris S220 with settings PIP 105, duty 2, cpb 200 for 9 min.

Genomic DNA was cleaned up using QIAGEN Minelute Columns and quantified by Qubit. The same amount of chromatin from HEK293 cells was spiked in to equivalent volumes of ChIP eluates (62 pg of spike-in chromatin per 25 ul of ChIP), yielding final concentrations between ~1-5%. Libraries were constructed from 2.5 ng of DNA and prepared using the NEBNext Ultra II DNA Library Prep Kit for Illumina with 9 PCR cycles (NEB #E7645S). Library quality was assessed by High Sensitivity DNA Assay on an Agilent 2100 Bioanalyzer (Agilent Technologies). Samples were sequenced on a HiSeq 4000 using single-end 50 bp reads.

H3K27me3 ChIP-seq data analysis

Sequencing reads that passed quality control were trimmed of adaptors using trim_galore v0.4.0 and aligned to mm10 and hg19 using Bowtie2 v2.2.5 with no multimapping (Langmead and Salzberg, 2012). SAM files were converted to BAM files, sorted, and indexed using SAMtools (Li et al., 2009). Normalization factors (NFs) for each sample were calculated as a fraction of input reads as in van Mierlo et al. (van Mierlo et al., 2019). Bam files were deduplicated using picard v2.18.14 MarkDuplicates. H3K27me3 ChIP-seq data were downloaded as fastq files from NCBI GEO. For paired-end samples, only one read was kept and all samples were trimmed, aligned

to mm10, sorted, and deduplicated as above. Deduplicated bam files were analyzed using deepTools v3.3.0 on the command line (Ramírez et al., 2014).

Broad peak calling

Deduplicated bam files were converted to scaled bedgraphs using deepTools bamCoverage (options --scaleFactor <NF> --binSize 10 --blackListFileName ENCODE_mm10_blacklist.bed) and then to bed files using awk: awk '{print $1"\t"$2"\t"$3"\tid-"NR"\t"$4"\t."}'. These scaled bed files were used to call broad peaks relative to input files using epic2 on the command line (options -gn mm10, -d chrM) (Stovner and Sætrom, 2019). Bedtools merge was used to merge peaks within 3kb, and bedtools intersect was used to determine a set of common peaks between replicates (Quinlan and Hall, 2010).

Bam files were converted to scaled bigWigs using deepTools bamCoverage (*--binSize* 100 --*scaleFactor* <NF>). Correlation between replicates was checked by deeptools multiBigWigSummary bins and plotCorrelation, and then scaled bw files were merged (bigwigCompare add) for heatmaps. computeMatrix was used to generate coverage of scaled bigwig files over no-auxin peaks (options: scale-regions -m 500 --upstream 10000 --downstream 10000 --binSize 100 --missingDataAsZero --skipZeros --sortRegions descend --sortUsing mean --sortUsingSamples 1 -p max). Heatmaps were produced using deepTools plotHeatmap. TSS profile plots were generated from the output of deeptools plotProfile (--outFileNameData), which was imported into R, processed to average replicates, and then plotted with ggplot2. Sample tracks were visualized in Integrated Genome Viewer (IGV v2.3.92). multiBamSummary was used to count reads falling into non-overlapping 10kb genes across the genome, and read counts were then imported into R. Embryo counts were normalized by library sizes (number of mapped reads in deduplicated bam files), and ES

cell data were normalized by spike-in factors. For cumulative distribution plots, reads were counted in non-overlapping 10kb genomic bins using deeptools multiBamSummary. The resulting counts table was imported into R, filtered to remove regions without coverage, scaled with the NFs calculated above, and then plotted using ggplot2 (stat_ecdf). P-values represent Kolmogorov-Smirnov test results using the averages of replicates. Counts per bin were adjusted for biological batch (embryo vs. ES cell origin) using ComBat/sva in R and analyzed by PCA.

For repeats analysis, H3K27me3 was counted over individual repetitive elements (obtained from UCSC RepeatMasker) using featureCounts. In R, we filtered out elements with low coverage, scaled using the NFs calculated above, and calculated the average of replicates. Thresholds for enrichment were set as $\log_2$(Usp9x-high/no-auxin) > |0.7|. To select regions for plotting, we applied cutoffs for normalized counts: > 5 for hyper-H3K27me3 and >3 for hypo-H3K27me3 elements.

Data availability

Raw and processed sequencing files as well as R codes used for analyses will be made available upon publication.

General Discussion

Together, the results in Chapters 1 and 2 provide insight into post-translational control of the peri-implantation chromatin landscape. Our studies of permissive chromatin revealed that several key euchromatic regulators are intrinsically unstable proteins that are rapidly depleted upon short-term inhibition of translation. We previously reported that ES cells show a global increase in nascent translational output from 2i to serum (Bulut-Karslioglu et al., 2016). Cumulatively, our results provide a direct link between translational output and establishment of an open chromatin landscape at implantation. It will be important to assess whether such a transition occurs in the embryo, for example through *ex vivo* incorporation of HPG in pre- and post-implantation embryos. It is interesting that enhancers are more susceptible to acute changes in translational output than promoters, as detected by our ATAC-seq analysis. This may suggest more fine-tuned regulation of enhancer chromatin state in response to nutrient conditions, or perhaps factors that bind enhancers are more unstable.

We observe in Chapter 1 that acute inhibition of translation has little effect on heterochromatin state. It is important to note, however, that we did not include H3K27me3-marked facultative heterochromatin in this analysis. Given the reduction in nascent transcriptional output in these cells, I expect that acute CHX treatment promotes global gain of H3K27me3. This likely also occurs over regions of the genome that lose chromatin openness upon CHX treatment in the ATAC-seq experiment, including many developmental enhancers. Since activating chromatin marks and transcription directly impair PRC2 methyltransferase activity, the gain of H3K4me3 and other marks of

permissive chromatin in the early post-implantation epiblast may help erase the pre-implantation H3K27me3 landscape.

My results in Chapter 2 return to the question of protein stability but center on Suz12 and Ezh2, essential regulators of facultative heterochromatin. I showed that Usp9x opposes Suz12 and Ezh2 ubiquitination. Thus, high expression of Usp9x, as occurs in the pre-implantation embryo, positively regulates PRC2 activity. Exactly how it does so remains an open question. Ubiquitination regulates essentially all aspects of protein biology. My findings support the notion that Usp9x stabilizes PRC2 proteins, although it seems to be important to modestly overexpress ubiquitin to draw out this connection. This could be due to redundant post-translational regulation of the complex in ES cells. It would be interesting to explore which E3 ligase(s) are responsible for Suz12 and/or Ezh2 turnover at implantation. In preliminary experiments, I have found that Usp9x may co-localize with PRC2 to the chromatin, suggesting that it could directly stabilize the complex *in situ*. However, western blots on subcellular fractions (cytoplasm, nucleoplasm, and insoluble chromatin) did not reveal a pattern of higher chromatin-bound Suz12 or Ezh2 in Usp9x-high ES cells (data not shown). Other experiments to identify ubiquitinated Suz12 and Ezh2 at chromatin, for example sequential ChIP, are technically challenging. Another way to approach this question is to tease apart which forms of ubiquitin linkages Usp9x removes from its PRC2 substrates. Lysine48-linked poly-ubiquitination is the most associated with protein degradation (Komander and Rape, 2012), and Usp9x hydrolyzes multiple types of linkages (Paudel et al., 2019). Alternatively, ubiquitin could directly oppose catalytic activity of the complex, for example preventing allosteric activation or

blocking interaction with key partners. As all of the biochemical experiments conducted in Chapter 2 require large cell numbers, I have not tested the Usp9x-PRC2 relationship directly in embryos. It is of great interest to assess whether Usp9x deubiquitinates PRC2 components *in vivo*. In the meantime, it would be interesting to test for Usp9x-Suz12/Ezh2 interactions by proximity ligation assays in early embryos.

In repeated assays, from transcriptional to biochemical analyses, I observed that Usp9x levels parallel Suz12 levels and activity. Intriguingly, both genes occur in a transcriptional module that decreases sharply in mRNA expression early ~E8.0 and then rebounds by ~E8.5 (Mitiku and Baker, 2007). Additional studies are needed to determine what factors co-regulate Usp9x and Suz12. One candidate is the zinc-finger transcription factor Zfp281, a known regulator of the naïve-to-primed transition that binds to the *Usp9x* promoter (Fidalgo et al., 2016; Huang et al., 2017; Kim et al., 2008).

There are several lines of *in vivo* work that would be interesting to pursue. First, deletion of *Usp9x* earlier in development would allow me to ask the question raised by my ES cell work: does Usp9x promote PRC2 activity in the pre-implantation embryo? I expect that knockout of *Usp9x* by, for example, a constitutive Cre (Rosa26-Cre) would result in lower levels of H3K27me3 during cleavage stages. A caveat to this experiment is that Usp9x may play a role in specifying extra-embryonic tissues, but one way to sidestep this issue is through tetraploid complementation. To this point, aggregation of *Usp9x*-mutant (by gene trap) ES cells at the morula stage results in post-implantation defects around embryonic turning (Cox et al., 2010), suggesting that the major role for Usp9x is not during

pre-implantation development, or at least not during late pre-implantation stages. A maternal deletion model using either Zp3-Cre or Gdf9-Cre could address roles for Usp9x prior to trophectoderm specification.

Another key mouse experiment is to perform deletions of *PRC2* components solely in epiblast cells. Similar to many other constitutive knockout mice (Perez-Garcia et al., 2018), reports that *PRC2* mutants are peri-gastrulation lethal are difficult to interpret given the known role for H3K27me3 in specification of extraembryonic tissues (Rugg-Gunn et al., 2010; Saha et al., 2013). I predict that loss of *Suz12* would phenocopy the loss of *Usp9x* that I describe in this thesis, given their paralleled expression dynamics. Ezh2 is also a Usp9x substrate and may therefore have a similar phenotype. Deletion of *Ezh2* and *Eed* in mice leads to abnormal gain of extraembryonic mesoderm (Faust et al., 1995; O'Carroll et al., 2001), suggesting important roles for PRC2 in protecting epiblast cell fate. *Suz12* mutants were not reported to show this phenotype (Pasini et al., 2004), raising the intriguing possibility that Suz12 promotes rather than restrains extraembryonic programs in epiblast cells. Another view on these data is that maternal PRC2 is especially important for the balance between embryonic and extraembryonic specification, and thus the maternal load of PRC2 mRNA/proteins will affect the phenotype. If Suz12 is transcribed from the zygotic genome earlier than Ezh2 and Eed, then the effect of maternal deletion would be less severe.

There is growing evidence that maternal PRC2 functions in early development. Recent sequencing studies indicate that broad H3K27me3 domains in early mouse embryos are

maternally inherited and mediate non-canonical (i.e. not by DNA methylation) genomic imprinting (Zheng et al., 2016; Inoue et al., 2017). In light of my own results, it would be interesting to assess whether premature hypertranscription in the embryo contributes to growth restriction in *Ezh2*-hypomorphic embryos. Another possibility is that loss of the Usp9x-PRC2 axis derepresses transposable elements, which may have implications for long-term organismal health and homeostasis and/or development of the germline. Interestingly, maternal *Ezh2* mutant mice are born but remain small postnatally (Erhardt et al., 2003). The molecular consequences of Ezh2 loss in this case were not well studied, but the phenotype could be due to poor placentation. This is a particularly enticing prospect given that Usp9x regulates Peg10, a paternally-expressed imprinted gene that stimulates placental growth (Ono et al., 2006). Thus, a picture emerges in which Usp9x and Suz12—and subsequently PRC2—are coordinately regulated to partition embryonic versus extraembryonic fate in the early embryo.

There is a lot to learn from non-mammalian model organisms that do not produce invasive placentas. Although Drosophila embryos do not specify extraembryonic tissues, maternal PRC2 domains contribute to specification of germ cell versus embryonic cell fate early in embryogenesis (Zenk et al., 2017). It is striking that PRC2 loss via *Ezh2* deletion causes relatively mild consequences for zebrafish development; embryos gastrulate but later show ectopic domains of gene expression (Rougeot et al., 2019). Different groups report variable effects of PRC2 knockdowns on survival of Xenopus embryos (Kerns et al., 2012; Lim et al., 2011; Peng et al., 2009), but the function of spatial gene restriction after gastrulation appears to be conserved (Akkers et al., 2009). I posit that, in mice, a major

role for PRC2 in early development is in proper specification of the extraembryonic tissue, and its role in the post-implantation epiblast is primarily to reinforce spatial and/or lineage-specific patterns of gene expression. Epiblast-specific deletions will allow careful dissections of this hypothesis.

My work raises many other questions related to mechanism and conservation of mechanism. First, broad domains of H3K27me3 appear to be an ancestral function of PRC2 (Dumesic et al., 2015), and thus it would be interesting to explore whether Usp9x stimulates this function in other organisms. Second, Usp9x has previously been found to interact with an array of substrates relevant to peri-implantation development. For one, Usp9x interacts with mTor in muscle cells (Agrawal et al., 2012). This is interesting as we have previously found that inhibition of mTor induces prolonged developmental pausing in both ES cells and blastocysts (Bulut-Karslioglu et al., 2016). Could Usp9x help integrate mTor activity with PRC2 output? Finally, *Usp9x* is an X-linked gene with a well-conserved homolog on the Y chromosome, *Usp9y*. A small number of such X-Y gene pairs have been retained over evolution (Bellott et al., 2014; Lahn and Page, 1997). Is there any role for Usp9y in early development?

I leave these questions and many others to the next enthusiast of Usp9x.

References

Agrawal, P., Chen, Y.T., Schilling, B., Gibson, B.W., and Hughes, R.E. (2012). Ubiquitin-specific Peptidase 9, X-linked (USP9X) Modulates Activity of Mammalian Target of Rapamycin (mTOR). Journal of Biological Chemistry *287*, 21164–21175.

Akkers, R.C., van Heeringen, S.J., Jacobi, U.G., Janssen-Megens, E.M., FranCoijs, K.-J., Stunnenberg, H.G., and Veenstra, G.J.C. (2009). A Hierarchy of H3K4me3 and H3K27me3 Acquisition in Spatial Gene Regulation in Xenopus Embryos. Developmental Cell *17*, 425–434.

Beddington, R.S. (1983). Histogenetic and neoplastic potential of different regions of the mouse embryonic egg cylinder. J Embryol Exp Morphol *75*, 189–204.

Bellott, D.W., Hughes, J.F., Skaletsky, H., Brown, L.G., Pyntikova, T., Cho, T.-J., Koutseva, N., Zaghlul, S., Graves, T., Rock, S., et al. (2014). Mammalian Y chromosomes retain widely expressed dosage-sensitive regulators. Nature *508*, 494–499.

Boroviak, T., Loos, R., Bertone, P., Smith, A., and Nichols, J. (2014). The ability of inner-cell-mass cells to self-renew as embryonic stem cells is acquired following epiblast specification. Nat Cell Biol *16*, 513–525.

Bradley, A., Evans, M., Kaufman, M.H., and Robertson, E. (1984). Formation of germ-line chimaeras from embryo-derived teratocarcinoma cell lines. Nature *309*, 255–256.

Brons, I.G.M., Smithers, L.E., Trotter, M.W.B., Rugg-Gunn, P., Sun, B., Chuva de Sousa Lopes, S.M., Howlett, S.K., Clarkson, A., Ahrlund-Richter, L., Pedersen,

R.A., et al. (2007). Derivation of pluripotent epiblast stem cells from mammalian embryos. Nature *448*, 191–195.

Bulut-Karslioglu, A., Biechele, S., Jin, H., Macrae, T.A., Hejna, M., Gertsenstein, M., Song, J.S., and Ramalho-Santos, M. (2016). Inhibition of mTOR induces a paused pluripotent state. Nature *540*, 119–123.

Chazaud, C., and Yamanaka, Y. (2016). Lineage specification in the mouse preimplantation embryo. Development *143*, 1063–1074.

Choi, Y.J., Lin, C.-P., Risso, D., Chen, S., Kim, T.A., Tan, M.H., Li, J.B., Wu, Y., Chen, C., Xuan, Z., et al. (2017). Deficiency of microRNA miR-34a expands cell fate potential in pluripotent stem cells. Science *355*, aag1927–13.

Cockburn, K., and Rossant, J. (2010). Making the blastocyst: lessons from the mouse. J. Clin. Invest. *120*, 995–1003.

Cox, B.J., Vollmer, M., Tamplin, O., Lu, M., Biechele, S., Gertsenstein, M., van Campenhout, C., Floss, T., Kühn, R., Wurst, W., et al. (2010). Phenotypic annotation of the mouse X chromosome. Genome Res. *20*, 1154–1164.

Damjanov, I., Solter, D., and Škreb, N. (1971). Teratocarcinogenesis as related to the age of embryos grafted under the kidney capsule. W. Roux' Archiv F. Entwicklungsmechanik *167*, 288–290.

Dumesic, P.A., Homer, C.M., Moresco, J.J., Pack, L.R., Shanle, E.K., Coyle, S.M., Strahl, B.D., Fujimori, D.G., Yates, J.R., and Madhani, H.D. (2015). Product binding enforces the genomic specificity of a yeast polycomb repressive complex. Cell *160*, 204–218.

Erhardt, S., Su, I.-H., Schneider, R., Barton, S., Bannister, A.J., Perez-Burgos, L., Jenuwein, T., Kouzarides, T., Tarakhovsky, A., and Surani, M.A. (2003). Consequences of the depletion of zygotic and embryonic enhancer of zeste 2 during preimplantation mouse development. Development *130*, 4235–4248.

Evans, M.J., and Kaufman, M.H. (1981). Establishment in culture of pluripotential cells from mouse embryos. Nature *292*, 154–156.

Faust, C., Schumacher, A., Holdener, B., and Magnuson, T. (1995). The eed mutation disrupts anterior mesoderm production in mice. Development *121*, 273–285.

Fidalgo, M., Huang, X., Guallar, D., Sanchez-Priego, C., Valdes, V.J., Saunders, A., Ding, J., Wu, W.-S., Clavel, C., and Wang, J. (2016). Zfp281 Coordinates Opposing Functions of Tet1 and Tet2 in Pluripotent States. Stem 1–16.

Guzman-Ayala, M., Sachs, M., Koh, F.M., Onodera, C., Bulut-Karslioglu, A., Lin, C.J., Wong, P., Nitta, R., Song, J.S., and Ramalho-Santos, M. (2014). Chd1 is essential for the high transcriptional output and rapid growth of the mouse epiblast. Development *142*, 118–127.

Huang, X., Balmer, S., Yang, F., Fidalgo, M., Li, D., Guallar, D., Hadjantonakis, A.-K., and Wang, J. (2017). Zfp281 is essential for mouse epiblast maturation through transcriptional and epigenetic control of Nodal signaling. Elife *6*, 243.

Inoue, A., Jiang, L., Lu, F., Suzuki, T., and Zhang, Y. (2017). Maternal H3K27me3 controls DNA methylation-independent imprinting. Nature *547*, 419–424.

Kerns, S.L., Schultz, K.M., Barry, K.A., Thorne, T.M., and McGarry, T.J. (2012). Geminin is required for zygotic gene expression at the Xenopus mid-blastula transition. PLoS ONE *7*, e38009.

Kim, J., Chu, J., Shen, X., Wang, J., and Orkin, S.H. (2008). An Extended Transcriptional Network for Pluripotency of Embryonic Stem Cells. Cell *132*, 1049–1061.

Kleinsmith, L.J., and Pierce, G.B.J. (1964). MULTIPOTENTIALITY OF SINGLE EMBRYONAL CARCINOMA CELLS. Cancer Research *24*, 1544–1551.

Kojima, Y., Kaufman-Francis, K., Studdert, J.B., Steiner, K.A., Power, M.D., Loebel, D.A.F., Jones, V., Hor, A., de Alencastro, G., Logan, G.J., et al. (2014). The transcriptional and functional properties of mouse epiblast stem cells resemble the anterior primitive streak. Cell Stem Cell *14*, 107–120.

Komander, D., and Rape, M. (2012). The Ubiquitin Code. Annu. Rev. Biochem. *81*, 203–229.

Lahn, B.T., and Page, D.C. (1997). Functional coherence of the human Y chromosome. Science *278*, 675–680.

Lim, J.-W., Hummert, P., Mills, J.C., and Kroll, K.L. (2011). Geminin cooperates with Polycomb to restrain multi-lineage commitment in the early embryo. Development *138*, 33–44.

Manejwala, F.M., Cragoe, E.J., and Schultz, R.M. (1989). Blastocoel expansion in the preimplantation mouse embryo: role of extracellular sodium and chloride and possible apical routes of their entry. Developmental Biology *133*, 210–220.

Marks, H., Kalkan, T., Menafra, R., Denissov, S., Jones, K., Hofemeister, H., Nichols, J., Kranz, A., Stewart, A.F., Smith, A., et al. (2012). The Transcriptional and Epigenomic Foundations of Ground State Pluripotency. Cell *149*, 590–604.

Martin, G.R. (1981). Isolation of a pluripotent cell line from early mouse embryos cultured in medium conditioned by teratocarcinoma stem cells. Proc Natl Acad Sci USA *78*, 7634–7638.

Mitiku, N., and Baker, J.C. (2007). Genomic Analysis of Gastrulation and Organogenesis in the Mouse. Developmental Cell *13*, 897–907.

Nichols, J., and Smith, A. (2009). Naive and primed pluripotent states. Cell Stem Cell *4*, 487–492.

O'Carroll, D., Erhardt, S., Pagani, M., Barton, S.C., Surani, M.A., and Jenuwein, T. (2001). The Polycomb-Group Gene Ezh2 Is Required for Early Mouse Development. Molecular and Cellular Biology *21*, 4330–4336.

Ono, R., Nakamura, K., Inoue, K., Naruse, M., Usami, T., Wakisaka-Saito, N., Hino, T., Suzuki-Migishima, R., Ogonuki, N., Miki, H., et al. (2006). Deletion of Peg10, an imprinted gene acquired from a retrotransposon, causes early embryonic lethality. Nat. Genet. *38*, 101–106.

Osorno, R., Tsakiridis, A., Wong, F., Cambray, N., Economou, C., Wilkie, R., Blin, G., Scotting, P.J., Chambers, I., and Wilson, V. (2012). The developmental dismantling of pluripotency is reversed by ectopic Oct4 expression. Development *139*, 2288–2298.

Paudel, P., Zhang, Q., Leung, C., Greenberg, H.C., Guo, Y., Chern, Y.-H., Dong, A., Li, Y., Vedadi, M., Zhuang, Z., et al. (2019). Crystal structure and activity-based labeling reveal the mechanisms for linkage-specific substrate recognition by deubiquitinase USP9X. Proc Natl Acad Sci USA *116*, 201815027–10.

Peng, J.C., Valouev, A., Swigut, T., Zhang, J., Zhao, Y., Sidow, A., and Wysocka, J. (2009). Jarid2/Jumonji Coordinates Control of PRC2 Enzymatic Activity and Target Gene Occupancy in Pluripotent Cells. Cell *139*, 1290–1302.

Percharde, M., Wong, P., and Ramalho-Santos, M. (2017). Global Hypertranscription in the Mouse Embryonic Germline. CellReports *19*, 1987–1996.

Perez-Garcia, V., Fineberg, E., Wilson, R., Murray, A., Mazzeo, C.I., Tudor, C., Sienerth, A., White, J.K., Tuck, E., Ryder, E.J., et al. (2018). Placentation defects are highly prevalent in embryonic lethal mouse mutants. Nature 1–23.

Rossant, J., and Tam, P.P.L. (2009). Blastocyst lineage formation, early embryonic asymmetries and axis patterning in the mouse. Development *136*, 701–713.

Rougeot, J., Chrispijn, N.D., Aben, M., Elurbe, D.M., Andralojc, K.M., Murphy, P.J., Jansen, P.W.T.C., Vermeulen, M., Cairns, B.R., and Kamminga, L.M. (2019). Maintenance of spatial gene expression by Polycomb-mediated repression after formation of a vertebrate body plan. Development *146*, dev178590–14.

Rugg-Gunn, P.J., Cox, B.J., Ralston, A., and Rossant, J. (2010). Distinct histone modifications in stem cell lines and tissue lineages from the early mouse embryo. Proc. Natl. Acad. Sci. U.S.a. *107*, 10783–10790.

Saha, B., Home, P., Ray, S., Larson, M., Paul, A., Rajendran, G., Behr, B., and Paul, S. (2013). EED and KDM6B coordinate the first mammalian cell lineage commitment to ensure embryo implantation. Molecular and Cellular Biology *33*, 2691–2705.

Smith, A. (2017). Formative pluripotency: the executive phase in a developmental continuum. Development *144*, 365–373.

Snow, M.H. (1981). Growth and its control in early mammalian development. Br. Med. Bull. *37*, 221–226.

Snow, M.H.L. (1977). Gastrulation in the mouse: Growth and regionalization of the epiblast. Development *42*, 293–303.

Takahashi, K., and Yamanaka, S. (2006). Induction of Pluripotent Stem Cells from Mouse Embryonic and Adult Fibroblast Cultures by Defined Factors. Cell *126*, 663–676.

Tesar, P.J., Chenoweth, J.G., Brook, F.A., Davies, T.J., Evans, E.P., Mack, D.L., Gardner, R.L., and McKay, R.D.G. (2007). New cell lines from mouse epiblast share defining features with human embryonic stem cells. Nature *448*, 196–199.

Yang, Y., Liu, B., Xu, J., Wang, J., Wu, J., Shi, C., Xu, Y., Dong, J., Wang, C., Lai, W., et al. (2017). Derivation of Pluripotent Stem Cells with In Vivo Embryonic and Extraembryonic Potency. Cell *169*, 243–257.e25.

Ying, Q.-L., Wray, J., Nichols, J., Batlle-Morera, L., Doble, B., Woodgett, J., Cohen, P., and Smith, A. (2008). The ground state of embryonic stem cell self-renewal. Nature *453*, 519–523.

Zenk, F., Loeser, E., Schiavo, R., Kilpert, F., Bogdanović, O., and Iovino, N. (2017). Germ line-inherited H3K27me3 restricts enhancer function during maternal-to-zygotic transition. Science *357*, 212–216.

Zheng, H., Huang, B., Zhang, B., Xiang, Y., Du, Z., Xu, Q., Li, Y., Wang, Q., Ma, J., Peng, X., et al. (2016). Resetting Epigenetic Memory by Reprogramming of Histone Modifications in Mammals. Molecular Cell *63*, 1066–1079.

Publishing Agreement

It is the policy of the University to encourage the distribution of all theses, dissertations, and manuscripts. Copies of all UCSF theses, dissertations, and manuscripts will be routed to the library via the Graduate Division. The library will make all theses, dissertations, and manuscripts accessible to the public and will preserve these to the best of their abilities, in perpetuity.

Please sign the following statement:

I hereby grant permission to the Graduate Division of the University of California, San Francisco to release copies of my thesis, dissertation, or manuscript to the Campus Library to provide access and preservation, in whole or in part, in perpetuity.

DocuSigned by:
C18398F4EB9F433...

Author Signature

12/5/2019

Date